2010

Development of a Scale Vehicle Dynamics Test Bed

Andrew Liburdi
University of Windsor

Development of a Scale Vehicle Dynamics Test Bed

by

Andrew Liburdi

A Thesis
Submitted to the Faculty of Graduate Studies
through
Mechanical, Automotive, and Materials Engineering
in Partial Fulfillment of the Requirements for
the Degree of Master of Applied Science at the
University of Windsor

Windsor, Ontario, Canada

2010

Development of a Scale Vehicle Dynamics Test Bed

by

Andrew Liburdi

APPROVED BY:

_____

Dr. Xiaohong, Xu, Outside Program Reader
Department of Civil and Environmental Engineering

_____

Dr. Gary Rankin, Program Reader
Department of Mechanical, Automotive and Materials Engineering

_____

Dr. Bruce Minaker, Advisor
Department of Mechanical, Automotive and Materials Engineering

_____

Dr. Peter Frise, Co-Advisor
Department of Mechanical, Automotive and Materials Engineering

_____

Dr. Vesselin Stoilov , Chair of Defense
Department of Mechanical, Automotive and Materials Engineering

September 10, 2010

DECLARATION OF ORIGINALITY

I hereby certify that I am the sole author of this thesis and that no part of this thesis has been published or submitted for publication.

I certify that, to the best of my knowledge, my thesis does not infringe upon anyone's copyright nor violate any proprietary rights and that any ideas, techniques, quotations, or any other material from the work of other people included in my thesis, published or otherwise, are fully acknowledged in accordance with the standard referencing practices. Furthermore, to the extent that I have included copyrighted material that surpasses the bounds of fair dealing within the meaning of the Canada Copyright Act, I certify that I have obtained a written permission from the copyright owner(s) to include such material(s) in my thesis and have included copies of such copyright clearances to my appendix.

I declare that this is a true copy of my thesis, including any final revisions, as approved by my thesis committee and the Graduate Studies office, and that this thesis has not been submitted for a higher degree to any other University or Institution.

ABSTRACT

Research in the area of vehicle dynamics often requires that virtual models be correlated with test data or control systems be implemented within hardware. However, the prohibitive cost associated with a proper testing program has relegated the majority of research in these areas to virtual simulation.

The purpose of this research was to develop a low cost vehicle dynamics test bed, which could be used to investigate the full operational range of vehicle handling. A scaled approach, analogous to wind tunnel testing, was used in order to make predictions about a system based on observations obtained from a scale model. The following test bed is unique since it is untethered from the acquisition system allowing for a wider range of test manoeuvres to be used. Results obtained from the test bed verified the usefulness of a scaled approach with good correlation being achieved between linear handling models and test data.

DEDICATION

To my wife Yan, without whom none of this would have been possible.

ACKNOWLEDGMENTS

I would first like to thank my supervisor Dr. Bruce Minaker who has always supported me over the last eight years as both an undergraduate and graduate student. His patience and guidance when the project proved to be the most difficult, allowed me to find my way and accomplish my goals. For that I am grateful.

I would also like to thank Rob Rieveley, a fellow graduate student, who helped work out countless problems throughout the course of this project and was integral in helping formulate this research. His knowledge and assistance in the area of control electronics proved to be invaluable in developing the test bed.

I would like to acknowledge my family for the tremendous amount of support that they have given me throughout my life. I need to thank by brothers who have always been there for me, providing words of encouragement and guidance along the way. It is comforting to know that I have four older brothers who will always look out for me.   I also need to thank my parents who have done an amazing job of raising five boys. Thank you for the sacrifices you have made to ensure that we always had what we needed and the guidance you have given to all of us. I have always strived to make you proud and any successes I have had in my life are a result of your guidance and support. For that I am forever grateful.

Lastly, I need to thank my wife Yan, who has done nothing but support me throughout this whole process. I want to thank her for her patience and the sacrifices she made in order allow me to pursue this degree. Without a doubt, none of this would have been possible without her.

TABLE OF CONTENTS

LIST OF TABLES

LIST OF FIGURES

NOMENCLATURE

Label	Description
NHTSA	National Highway Traffic and Safety Administration
FBD	Free Body Diagram
CG	Center of Gravity
a	Distance of CG from front axle
b	Distance of CG from rear axle
c	Lateral location of CG from left side tires
l	Wheelbases
h or h_{CG}	CG height from road surface
t	Track width
I_{zz}	Yaw mass moment of inertia
I_{xx}	Roll mass moment of inertia
I_{yy}	Pitch mass moment of inertia
r, ϕ	Yaw rate
v	Lateral velocity
a_y or A_y	Lateral acceleration
a_x or A_x	Longitudinal acceleration
a_z or A_z	Vertical acceleration
C_α, C_f, C_r	General cornering stiffness, Cornering stiffness of front tires, Cornering stiffness of rear tires respectively
R	Turning radius
α	Lateral slip angle
m	Mass
β	Body slip angle
δ	Front wheel steer angle
W, W_{XX}	Weight of vehicle, where XX represents location such as left, right , front or rear

Label	Description
U, u	Forward vehicle velocity
IRS	Illinois Roadway Simulator, University of Urbana-Champaign
PURRS	Roadway simulator, Penn State University
EEPROM	Electronically Erasable Programmable Read Only Memory
I/O	Input/Output
R_O	Kinematic turning radius
IMU	Inertial measurement unit
SPI	Serial protocol interface – Serial communication
EUSART	Hardware implemented module on PIC microcontrollers to carry out serial communication
MSSP	Hardware implemented module on PIC microcontrollers to carry out serial communication
f	Frequency
V_{SS}	Ground voltage, logic 0
V_{DD}	Supply voltage, logic 1
ΔW	Normal load transfer
ABS	Anti-lock braking system
TCS	Traction Control System
ESC	Electronic Stability Control
RC	Radio Controlled or Resistor/Capacitor circuit
MLT	Mass – Length – Time base dimensions
FLT	Force – Length – Time base dimensions
ROM	Read only memory
DC	Zero Hertz
CPU	Central Processing Unit
ALU	Arithmetic Logic Unit
PC	Program Counter

Label	Description
A/D	Analog to Digital convertor
I^{2}C	Serial communication protocol
SPI	Serial communication protocol
V_{crit}	Critical speed
V_{char}	Characteristic speed

Chapter 1: Introduction

1.1 Motivation

Currently, the majority of vehicle dynamic research being conducted is largely relegated to virtual simulation. The emphasis on simulations is directly due to the cost associated with a proper vehicle testing program. Even though virtual simulation has proven to be extremely valuable, allowing researchers to predict vehicle behaviour over a wide range of operating conditions; it is often necessary to validate these models with test data. Also, the implementation of vehicle dynamic control systems, require that these systems be tested in hardware on actual vehicles in order to ensure proper design intent. Therefore, due to the high costs associated with vehicle testing, this type of research is primarily conducted by automotive manufactures or research groups with large enough budgets that justify such methods. It becomes an even larger issue when considering academia, since the cost of data acquisition equipment alone can easily surpass most research grants. Take into account the time and effort associated with vehicle preparation, the cost of scheduling testing time, and the prospect of conducting this type testing is daunting for most groups.

There has been a tremendous amount of interest in developing low cost methods for testing vehicle handling behaviour. These methods will allow a larger portion of the research community to validate their work and hopefully result in more rapid advancements within the field. One of the more popular methods that is gaining acceptance is scale vehicle dynamic testing, which is analogous to wind tunnel testing, a common method used in the study of fluid mechanics. This approach allows researchers to predict vehicle behaviour based on data collected using scale sized models. Recent research in this area has been very promising, allowing for vehicle dynamics, as well as control research to be conducted without many of the problems associated with full sized testing.

Some key advantages of scale testing are its low cost, increased safety, high repeatability and its usefulness at validating control methods. Scale testing is ideally suited for advanced control development, since researchers can investigate more aggressive strategies without fear of injury to personnel or damage to property. In fact, it is often stated within the literature that the most important aspect of scale vehicle testing is its ability to test vehicle stability via aggressive driving situations, which would otherwise be too dangerous for traditional full scale testing [1].

Another encouraging aspect of scale testing is that it has been shown to closely correlate with common vehicle models, as well as full size vehicle test data [*2*]. Controllers developed on scale vehicles have been shown to stabilize their full sized counterparts once the proper scaling factors have been applied [*3*]. All of these benefits make scale vehicle testing very attractive to researchers and therefore is the focus of this thesis.

1.2 Outline of Chapters

This thesis presents the development of a scale vehicle dynamic test bed that is used at the University of Windsor. The system is able to characterize vehicle handling and assist with the development of vehicle dynamic controllers. It is unique when compared to other scale test beds in that the acquisition system is contained within the vehicle, which allows for a wider range of testing manoeuvre to be conducted. The remaining chapters can be broken down as follows.

 Chapter 2 introduces important concepts related to vehicle dynamics and dimensional analysis, which form a basis for the development of the test bed. The most recent applications of scale vehicle dynamics found within the literature will be discussed and research goals presented. Chapter 3 details the development of the virtual models used in correlating test data, as well as a description of the scale vehicle used within this research. Chapter 4 presents the development of the test bed and the design approach used in creating a custom data acquisition system. Chapter 5 will present the testing manoeuvres used to evaluate the vehicle's handling behaviour and discuss the experimental results that were obtained. Finally, Chapter 6 will present conclusions and recommendations that were obtained from this research.

Chapter 1: Introduction | Andrew Liburdi

Chapter 2: Literature Review

2.1 Vehicle Dynamics and Control

The modern automobile has come a long way in the last two decades. Modern vehicles have dramatically improved in key areas such as safety, performance, durability and efficiency. In order to realize these goals, manufacturers have relied heavily on advanced vehicle modeling and computer control. The increased performance of today's vehicles can be attributed to the improved understanding of how vehicles behave throughout a wide range of operating conditions. This understanding has been achieved through the use of advanced analysis tools, which are able to model the most complex nonlinear behaviour to a high level of fidelity. The use of these tools has fundamentally changed the way in which vehicles are designed; allowing engineers to optimize a vehicle chassis within the virtual realm, without the need to build expensive physical prototypes [4]. The change in development methodology has allowed manufacturers to introduce new vehicles to the market faster while at the same time reducing development costs. The extra development time and money can be used to optimize vehicle systems which ultimately results in the higher levels of quality and refinement that customers have come to expect.

The implementation of computer control has had a profound impact on vehicle safety, with present control systems having the ability to monitor the state of a vehicle thousands of times per second. They can then intervene in an instant in order to help a driver during an emergency situation [5]. For example, controllers can actuate the braking system in order to reduce braking distances (ABS); or they can maintain vehicle stability by applying the brakes to specific wheels in an effort to stabilize yaw motions (stability control). Due to improvements in the computing power of current low cost silicon, these control methods are becoming more advanced and are continually pushing the boundaries of vehicle safety and performance to new heights.

Whatever the implementation, there is no doubt that computer control has had a dramatic effect on how vehicles of today function and most importantly, on what customers have come to expect from automobile manufacturers [6]. No single area of vehicle development is this more evident than in vehicle dynamics, where these technologies have become common place. For example, the National Highway Traffic and Safety Administration (NHTSA) has recently

mandated that all vehicles use stability control technologies as standard issued equipment starting in 2012 [7].

Any discussion on the topic of vehicle dynamics and control can be broken down into three fundamental areas; longitudinal dynamics, handling (planar dynamics) and ride (vertical dynamics). The remainder of this thesis primarily focuses on the handling dynamics of scale vehicles and therefore a brief development of important concepts associated with handling behaviour will be presented. Also, a survey of some of the more popular implementations of computer control being used to improve handling will be highlighted.

2.1.1 Tire Basics

The pneumatic tire is arguably one of the most complicated devices that we use today. Tire response is dependent on dozens of variables, some of which include: internal pressure, temperature, chemical compound and tread design [8]. In terms of vehicle dynamics, the tire is the single most important factor in determining how a vehicle responds to driver inputs. This is due to the fact that the only portion that connects a vehicle to the road is the contact patch of each tire. Therefore, an extensive amount of work has been conducted over the years in order to investigate how a tire behaves under various conditions. This section will highlight some of the basic concepts involved in their analysis and act as a primer for the discussions about scale vehicles that follow.

Slip Angle:

In order for a tire to produce the traction forces that are required to accelerate a vehicle in a straight line or around a corner, it is necessary for the tire to develop a slip angle [9]. The slip angle can be explained by the fact that the elastic characteristics of a tire allow it to be pointed in a direction different from which the vehicle is heading. The angle between these two headings is known as the lateral slip angle. Figure 1 shows a bottom view of a tire contact patch which is being subjected to a slip angle [8].
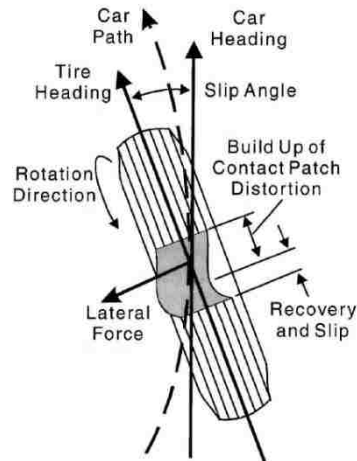
Figure 1: Bottom view of a tire contact patch subjected to a lateral slip angle.

Due to elastic distortion within the contact patch, the wheel travels along a different heading than that which it is pointed. The angle between these two headings is known as the lateral slip angle. As tread enters the contact patch it builds up at the leading edge causing the lateral distortion shown above. In this region the normal load is the highest allowing the tread to adhere to the road. As the tread moves rearward through the contact patch, the normal load decreases causing the tread to start slipping before it is allowed to recover back into the main tread, assuming its original undistorted shape. Note that lateral traction is a result of the elastic reaction forces created by the distortion in the contact patch, which means that tires cannot produce traction forces without first assuming a slip angle. Figure was taken from Haney [8].

When a rolling tire is subjected to a slip angle, the leading edge of the tread contacts the ground slightly to one side of the rest of the contact patch. As the tire continues to roll, each small increment of tread rubber coming into the contact patch contacts the road a small distance toward the direction the tire is pointed. When all of the small deviations in the tire's contact patch are added up, it results in the vehicle moving along a curved path.

Traction Forces:

A tire does not generate traction forces until it is steered away from its current course and assumes a slip angle. Figure 2 shows a typical lateral force curve of a radial tire. The shape of this curve is not the same for all tires, but rather is a specific characteristic of the design of the tire [4].

Notice that this curve has three distinct regions. First there is a straight section at small slip angles where an increase in slip angle gives a proportional increase in lateral force. The slope of this section of the curve is the cornering stiffness of the tire. In this region of the curve, the tread is not sliding on the road at any point in its contact patch [8]. At higher slip angles, portions of the tire patch are sliding and there is less of an increase in lateral force with respect to slip angle. This is called the transition region [4]. As the curve reaches its peak, more of the contact patch is sliding and the tire produces less lateral force. After the peak of the curve, lateral force

can reduce as much as 30% within a few degrees of extra slip angle [*8*]. At these high slip angles most of the contact patch is sliding, producing an increased amount of heat and wear. This high slip angle region is also known as tire saturation, since the tire is no longer able to generate any extra lateral force. Note that a similar situation exists for longitudinal traction forces.
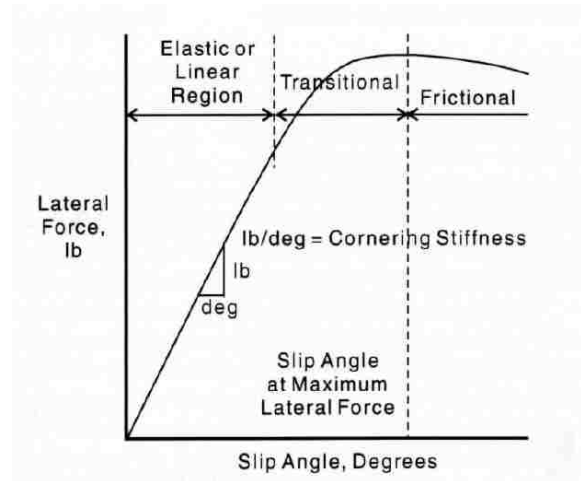
Figure 2: Lateral traction force curve of a pneumatic tire.

There are three distinct regions to a typical traction force curve highlighted above. 1) Linear region: The traction forces increase linearly with slip angle and the slop of the curve is known as the cornering stiffness (C_α). 2) Transitional Region: Within this region a portion of the contact patch starts to slide causing the lateral force to no longer increase linearly with slip angle. As the slip angle is increased further, more of the contacts patch slides causing the traction forces to reach a peak value before they start to decrease. 3) Frictional Region: In this region the majority of the contact patch is sliding and traction forces are produced due to sliding friction. The force curve decreases with increases to slip angle which is known as tire saturation. Figure was taken from Haney [*8*].

The Friction Circle:

The previous discussion about traction forces assumed that only lateral or longitudinal forces were being produced at any one time (i.e. pure cornering or pure acceleration/braking). However, in many situations a tire needs to produce both types of traction forces at the same time, such as when accelerating out of a corner. It is expected that the maximum amount of lateral force that the tire can produce will decrease when the tire is required to produce longitudinal forces as well [*10*]. A popular way of visualizing this dependence is called the friction circle, which is illustrated in Figure 3. The friction circle shows how the lateral force decreases in the presence of braking or acceleration. The concept is equally applicable to a single tire or a vehicle [*10*].
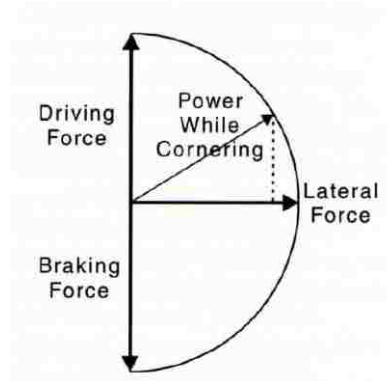
Figure 3: Traction circle plot of a typical pneumatic tire

The radius of the traction circle represents the total traction capability of the tire. The thicker arrows indicate pure cornering, braking and acceleration situations with their magnitudes equal to the radius of the friction circle. The general case of combined loading is represented by the thinner arrow. It is seen that the thin arrow is equal to the vector sum of the lateral and driving force components and that its magnitude is the same as the total traction limit of the tire. Therefore, as more lateral traction is needed, less driving traction is available since the resultant force must be within the total traction limit of the tire. Figure was taken from Haney [*8*].

The three thick arrows show maximum driving, braking, and lateral forces when pure acceleration/braking or cornering is present. When the tire experiences a combination of these forces, the maximum lateral force is not available. The friction circle represents the vector sum of both traction forces and is the maximum force that can be generated by the tire. Therefore, adding driving power to the tire reduces the available lateral force since the sum of their squares must equal the total traction force. A simple example of this is a high powered rear wheel drive vehicle that is accelerating out of a corner. Under hard acceleration, the rear end of the vehicle tends to get loose or slide because all of the traction capabilities of the rear tires are being used to accelerate the vehicle, leaving little to no traction left to maintain any lateral grip [*10*]. Note that the figure depicted above is a simplification of the real situation. A real traction plot is elliptical with the tire being able to generate slightly more driver/braking forces than lateral.

Load Sensitivity:

One of the unique properties of the pneumatic tire is known as load sensitivity. Referring to Figure 4, it is seen that as the normal load on a tire increases, the maximum traction force that the tire can produce also increases; however, this occurs in a nonlinear fashion. This nonlinear relationship is known as load sensitivity.
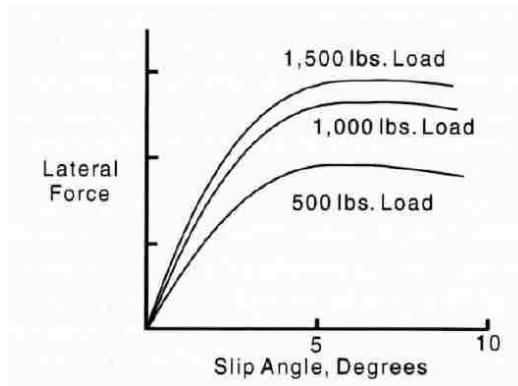
Figure 4: Normal load sensitivity of a pneumatic tire.

The above figure illustrates the relationship between normal load and the lateral traction limit of a tire. The traction limit of the tire is increased as the normal load is increased. However, it can be seen that the increase in the traction limit is smaller for higher normal loads, which is known as tire load sensitivity. Figure was taken from Haney [8].

This concept is critical when tuning a vehicle chassis for specific handling behaviour. The reasoning behind this is that as a vehicle corners and starts generating lateral acceleration, a portion of the weight that was once on the inside tires is transferred to the outside tires. The load transferred across an axle can be easily found by performing a force and moment balance on the FBD shown in Figure 5. Doing so results in the following expression.

Lateral Load Transfer:

$$\Delta W_{lateral} = W_R - W_L = \frac{Wha_y}{t} \qquad (1)$$
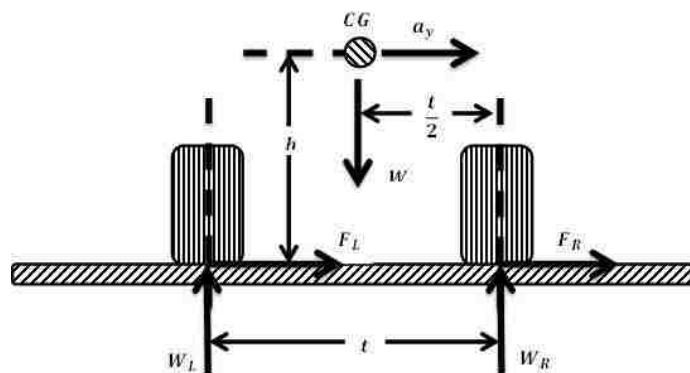
Figure 5: FBD of vehicle cornering model subjected to a lateral acceleration

As a vehicle corners a portion of its weight on the inside tires is transfer to the outside tires. The mathematical expressions that define this weight transfer can be determined by performing a moment balance on the above figure.

Chapter 2: Literature Review | Andrew Liburdi

Due to the load sensitivity of the tire, load transferred across an axle results in a larger reduction of traction forces on the inside tires than that which is gained by the outside tires. The result is a net decrease in the traction capability of the two tire combined [*9*]. By adjusting the amount of load transfer that occurs across each axle, engineers can manipulate a vehicle's lateral force balance which ultimately affects its handling characteristics. Tuning can be accomplished in several ways, some of which include modifying the longitudinal CG position, spring rates, and stiffness of anti-roll bars [*10*].

2.1.2 Vehicle Handling

The topic of vehicle handling primarily deals with motions within the plane of the road surface, which include lateral/longitudinal accelerations and the yaw rate. However, handling also encompasses out of plane dynamics such as roll and pitch motions, which generally need to be included when load transfer (lateral and longitudinal) is an important factor in dictating tire performance [*9*].

Vehicle handling models can be grouped into two main areas: linear and nonlinear. Linear models have the benefit of using frequency response methods, such as transfer function representations and eigenvalue analysis [*11*]. These methods can be used to investigate the stability of the system and are very valuable in demonstrating any fundamental dynamic modes that may exist. Linear models are generally a result of a system simplification (linearization), which usually limits their application to narrow operating ranges.

Nonlinear modeling is generally more accurate over a wider operating range, but requires more a complicated system representation. Usually nonlinearities introduced into handling models are due to the method in which tire traction forces are calculated or how the suspension system is modeled. Modern software tools use nonlinear models of suspension elements, such as springs, bushings, dampers and tires in order to predict behaviour over the vehicle's entire operating range. Although these software tools are very powerful, the vast majority of vehicle models used within controller design are linear. This is due to the fact that they do not require large computational resources to calculate vehicle states and are generally accurate enough to capture the important dynamics involved [*12*].

Linear Bicycle Model:

The most fundamental models of vehicle handling are based on the linear bicycle model. Although the development of this model will not be presented until a later chapter, it will be

mentioned here because it is the focus of much of the discussion that follows regarding scale vehicles. By using the bicycle model, it is possible to investigate the effects of tire cornering stiffness and inertial properties on the planar response of a vehicle [9]. The bicycle model FBD is illustrated in Figure 6.
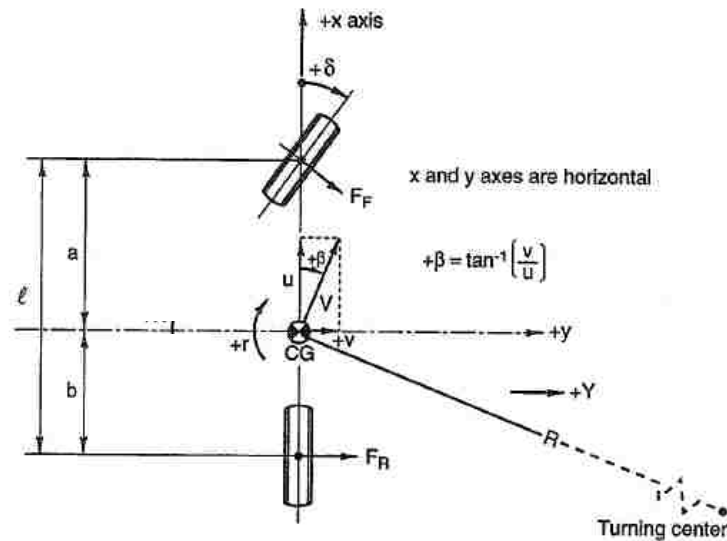
Figure 6: Linear bicycle model diagram

Linearized handling model used to predict planar response of a vehicle. Traction forces are assumed to be concentrated at a single contact patch at each axle designated above by F_F and F_R. The steer angle δ is used as the only excitation for this model. Figure was taken from Miliken [10].

Several assumptions are introduced in the development of the bicycle model in order to linearize the system. These assumptions are listed below.

> ➤ Track width is assumed to be negligible
> ➤ Tire operates within linear range
> ➤ Constant longitudinal velocity
> ➤ No aerodynamic effects
> ➤ Suspension geometry is neglected

As can been seen from the figure above, the first and most obvious assumption that is made is that the traction forces at each axle are assumed to be concentrated at a single contact patch, located along the center line of the vehicle. This has important implications related to when the model can be applied. Specifically, the lateral load transfer that is often involved in the vehicle's cornering dynamics is effectively neglected, since the vehicle's track is assumed to be zero. Previously, when discussing tire load sensitivity, it was shown that load transfer has an

important effect on the cornering capabilities of a vehicle. Therefore the application of the bicycle model is only valid for low lateral acceleration manoeuvres in which load transfer is minimized.

The most important assumption that is made in the development of the bicycle model is that the tire forces are assumed to be linearly proportional to slip angle. By referring to the traction force curve in Figure 2, this assumption is only valid when the tire is operating at small slip angles. This assumption also reinforces the idea that the model is only applicable for low slip angle manoeuvres, which generally occur when the vehicle is generating lateral accelerations of less than 0.3g [13]. In fact, Leblanc showed that the bicycle model is in close agreement with vehicle data when operated within the 0.3g limit [13].

The requirement that the vehicle must be generating less than 0.3g seems to be limiting; however research conducted by Leblanc [13] showed that for highway or city driving, which includes speeds above 30 km/h, lateral accelerations fall well within the 0.3g limit [13]. It is only in the most extreme situations, such as emergency manoeuvres or racing that the traction limits of the tire are used. Therefore, the bicycle model is well suited for developing controllers that mainly deal with low to medium acceleration situations.

2.1.3 Control Applications

The amount of published literature on vehicle dynamic control is extensive and the interested reader is encouraged to consult Tomizuka [6], and Furukawa [14] for more information on the subject. Also, those interested in control applications related to ride comfort can consult Hrovat [15], which provides a detailed survey of current optimal control strategies used in active and semi-active suspension systems. This thesis focuses primarily on the planar dynamics of vehicle control and therefore a summary of control topics related to vehicle handling will be presented.

Control strategies can be classified in many different ways. For example they can be grouped based on the design method used in their development (optimal, robust, neural networks) or by the type of actuation used (active, semi-active, etc.) [3]. However, it is much more useful to group the various control approaches according to the type of vehicle behaviour that they are designed to stabilize. By classifying control methods in this way, three primary areas are observed within vehicle handling: yaw rate control, roll mitigation, and lateral positioning control. These three areas have been the focus of most of the work over the last decade regarding vehicle

handling, whereas roll mitigation has become more popular in recent years due to the popularity of larger vehicles such as SUV's and trucks.

Yaw Rate Control:

The majority of control approaches that deal with vehicle handling revolve around the use of yaw rate feedback in calculating control functions. This is because most of the disturbances such as road irregularities and actuator nonlinearities can be by-passed through the use of the yaw rate measurement [*16*]. The majority of commercially available chassis control technologies utilize yaw rate feedback in conjunction with other subsystems, such as anti-lock brakes (ABS), or traction control (TCS). The most popular term used by manufacturers who implement these technologies is electronic stability control (ESC).

First developed by Bosch in 1995 [*14*], ESC methods typically monitor yaw rate, lateral velocity and body accelerations in order to determine the state of the vehicle. These states are then compared to vehicle models in order to determine the vehicle's stability state [*5*]. Inputs from the driver, such as, steer angle and throttle position are used to determine the driver's intent when calculating the response. The controller can then use the ABS or TCS systems to carry out the control function it deems necessary in order to maintain yaw stability. This system has been shown to be very successful at maintaining stability in low friction situations, such as in wet weather or icy conditions [*5*].

Roll Mitigation:

There has been a major focus by regulatory bodies such as NHTSA to further the development of technologies that reduce rollover incidents. This is due to the fact that vehicle rollover accounts for a disproportional amount of fatalities when compared to other types of accidents. For example, a recent study has shown that rollovers account for just 2.5% of all accidents per year in the United States; however, these contribute to approximately 20% of all fatalities [*17*]. This alarming statistic has caused regulators such as NHTSA to develop a number of transient manoeuvres that measure a vehicle's rollover performance. Similar to ESC, roll mitigation takes advantage of the ABS and TCS systems to generate counter yaw motions that reduce the propensity for rollover. The key difference is that they include the vehicle's roll rate and roll position when calculating the desired control function [*17*]. Roll mitigation is becoming increasingly popular on SUVs and trucks, since their high center of gravity makes them prone to rollovers.

Lateral Positioning Control:

The intent of lateral positioning control is to maintain the vehicle's position on the road surface. For the most part the driver is not considered in this control method and therefore these control approaches are regulated to autonomous vehicle applications [*3*]. The approaches are also broad in terms of feedback and actuation methods. For example GPS, radar, and vision systems are some of the common methods used to measure vehicle state. Commercial availability of technologies that use these approaches is limited. The most recent is a parallel parking system offered by Lexus in 2006 [*18*]. This system is able to parallel park a vehicle without any driver intervention. The system uses radar and vision systems to determine the locations of obstacles, while electronic power steering allows for complete control of the steering system and the manipulation of the vehicle [*18*].

Another notable system includes active cruise control, which was introduced by BMW in 2000 [*19*]. This technology uses range finding radar in order to determine the distance of vehicles in front and regulates the throttle and brakes to maintain a safe driving distance. It can also utilize the stability management system and GPS in order to determine if the vehicle is traveling at the proper speed when negotiating corners [*19*].

2.2 Scaled Systems

Dimensional analysis is a powerful tool that is used in many areas of engineering. It is based on the Buckingham Pi theorem and consists of recasting a system into a non-dimensional form such that its variable space is reduced and is independent of size. This is achieved by defining non-dimensional variables (Pi groups), which when substituted into the original system, result in a representation that is independent of dimension. This method is used extensively when conducting experimental testing, since the non-dimensional form of the system has fewer variables to control. Also, the results can be applied to other systems that satisfy basic similarity conditions [*20*].

One specific area of engineering that takes advantage of dimensional analysis is fluid mechanics. In fact, engineers are usually first introduced to dimensional methods in an introductory course in fluids [*20*]. This is because the majority of fluid mechanics theory is defined by common dimensionless Pi groups. Some of the more popular Pi groups are shown below in Table 1.

Table 1: Common Pi groups used within fluid mechanics

$\rho = density, V = fluid\ velocity, \mu = viscosity, p = pressure, c = speed\ of\ sound, l = length$

Pi Group	Name	Force Ratio	Application
$\dfrac{\rho V l}{\mu}$	Reynolds Number, Re	$\dfrac{inertia\ force}{viscous\ force}$	Generally important in all types of fluid dynamics problems
$\dfrac{V}{\sqrt{gl}}$	Froude Number, Fr	$\dfrac{inertia\ force}{gravitational\ force}$	Flow with a free surface
$\dfrac{p}{\rho V^2}$	Euler Number, Eu	$\dfrac{pressure\ force}{inertia\ force}$	Problems in which pressure, or pressure differences, are of interest
$\dfrac{V}{c}$	Mach Number, Ma	$\dfrac{inertia\ force}{compressibility\ force}$	Flows in which the compressibility of the fluid is important

A key application of dimensional methods within fluid mechanics is wind tunnel testing. Key Pi groups, such as Reynolds number and geometric scaling factors are taken into account in order to ensure that the test system is dynamically equivalent to the real system [*21*]. Doing so allows researchers to extend the results obtained from the wind tunnel and apply them to real systems with a high level of confidence.

The following sections will introduce the Buckingham Pi theorem and present a method that can be used to systematically determine the Pi parameters of a system. The linear bicycle model will be used as an example to demonstrate this method.

2.2.1 Buckingham Pi Theorem

The first question that needs to be answered when conducting a dimensional analysis is, "How many dimensionless Pi groups are needed to define a system?" This can be answered by the application of the Buckingham Pi theorem. The proof of the theorem is beyond the scope of this thesis but the interested reader can consult Buckingham [*21*] for details. The theorem is based on the concept of dimensional homogeneity, which was first studied by Fourier [*21*].

Dimensional homogeneity states that all terms in a mathematical expression that stand by themselves, or added together must be of the same dimension. Therefore, if we assume that a system can be defined by k variables, then a valid mathematical representation is;

$$u_1 = f(u_1, \, u_2, \cdots, u_k) \qquad (2)$$

Based on dimensional homogeneity, this expression implies that the dimension of u_1 is equal to all terms that stand by themselves on the right hand side. If we were to rearrange the terms to form dimensionless Pi groups (Π), then by Buckingham;

Buckingham Pi
Theorem:
$$\Pi = f(\Pi_1, \, \Pi_2, \cdots \Pi_{k-r}) \qquad (3)$$

Therefore, the Buckingham Pi theorem states that the required number of Pi terms is fewer than the original variables. The variable space has been reduced by r; the minimum number of base dimensions needed to define all variables within the system [21]. Usually mass, length and time (MLT) are used as the base dimensions; however, the only requirement is that the base dimensions cannot be combined to form a dimensionless group [20]. This is also known as dimensional independence.

2.2.2 Similitude

One of the most important aspects of dimensional analysis is the concept of similitude. If two systems can be defined by the same variables and operate under the same conditions, then they are considered similar. For example, consider a scale model that is to be developed for a prototype vehicle. Similitude between the two systems allows for predictions to be made about the prototype, based on observations obtained from the scale model [20]. This is guaranteed, provided certain similarity conditions are satisfied. Specifically;

Prediction Equation:
$$\Pi_{protoype} = \Pi_{model} \qquad (4)$$

If all Pi groups for the model and the prototype are equal then similitude is guaranteed. The above expression is known as the prediction equation and governs the relationship that needs to be satisfied between the model and prototype systems. Note that all Pi groups must be equal to ensure complete similitude. The fact that all Pi groups must be equal implies that geometric scaling is not the only factor that is required when designing a scaled experiment. Other factors of the system must be properly scaled to ensure that the model operates under the same test

conditions as the prototype. There are generally three scaling factors that need to be considered when developing a test [20].

> - Geometric – Length Scale
> - Dynamic – Force Scale
> - Kinematic – Velocity or Acceleration Scale

When it is not possible to achieve agreement between all Pi groups, the resulting model is called "distorted" [20]. Distorted models are very common and do not have any general rules for interpreting their results. The success of using such a model depends primarily on the skill and experience of the investigator involved. The validity of any similitude study is only guaranteed if all variables have been taken into account when determining the original Pi parameters. If any variable was neglected, then the resulting scaling factors will be incorrect and any predictions flawed [20].

2.2.3 *Method of Repeated Variables*

There are multiple methods that can be used to recast a system into a non-dimensional form; however, the Method of Repeated Variables is the most common and straightforward [20]. It is a systematic approach to determining the proper amount and form of the required Pi parameters. The method consists of five main steps which will be illustrated below.

Step 1: Identify all variables that affect the system

This step is the most difficult and most important throughout the whole procedure. If the proper variables are not selected, then the dimensional analysis will be incorrect. Determination of the variables is accomplished through the investigator's knowledge of the problem and physical laws that govern the phenomenon [20]. The only requirement is that all variables must be independent. For example, the cross sectional area and the diameter of a pipe should not be both used, since the area can be easily related to the diameter.

In order to illustrate this method the linear bicycle model that was discussed in a previous section will be used. The non-dimensional form of this model is used throughout this thesis so its development here will be a fundamental tenant of this work. The following dimensional analysis of the bicycle model was first presented by Brennan [22].

Example:

Assuming that a vehicle is front wheel steering and rear wheel drive, then the state space representation of the linear bicycle model can be shown to be;

Linear Bicycle
Model:

$$\dot{X} = AX + BU \qquad\qquad (5)$$

Where,

$$X = \begin{Bmatrix} v \\ \phi \end{Bmatrix}$$

$$A = \begin{bmatrix} -\dfrac{C_f + C_r}{mu} & -u - \dfrac{aC_f - bC_r}{mu} \\ -\dfrac{aC_f - bC_r}{I_{zz}u} & -\dfrac{a^2C_f + b^2C_r}{I_{zz}u} \end{bmatrix}$$

$$B = \begin{bmatrix} \dfrac{C_f}{m} \\ \dfrac{aC_f}{I_Z} \end{bmatrix}$$

$$U = \begin{Bmatrix} \delta \\ 0 \end{Bmatrix}$$

Vehicle Trajectory:

$$\dot{x} = ucos\theta + vsin\theta \qquad\qquad (6)$$

$$\dot{y} = usin\theta - vcos\theta$$

Where

$x = longitudinal\ position\ coordinate$
$y = lateral\ position\ coordinate$
$u = longitudinal\ velocity$
$v = lateral\ velocity$
$\phi = yaw\ rate$
$m = vehicle\ mass$
$I_{zz} = polar\ moment\ of\ inertia$
$C_f, C_r = front\ and\ rear\ axle\ cornering\ stiffness$
$a = distance\ between\ front\ axle\ and\ CG$
$b = distance\ between\ rear\ axle\ and\ CG$
$l = wheelbase$
$\delta = front\ wheel\ steering\ angle$

Because we wish to ultimately correlate the vehicle trajectory, then the vehicle position is a function of the following variables.

Vehicle Position:
$$(x, y) = f\big(\delta,\ \theta,\ m,\ I_{zz},\ C_f,\ C_r,\ a, l,\ u,\ v\big) \qquad (7)$$

Note that b is replaced by the wheelbase l, since the wheelbase is a standard measurement that is used when specifying vehicle parameters. Therefore, it would make the resulting scaling factors more meaningful. Both a, b and l cannot be used because they are related to one another through the following relationship.

Wheelbase:
$$a + b = l \qquad\qquad\qquad (8)$$

Step 2: Pick a set of base dimensions

Usually MLT or FLT are used as base dimensions, but any dimensionally independent set can be chosen.

Example:

For the bicycle model the following dimensions are observed;

$$x = y = a = l = [L]$$
$$m = [M]$$
$$I = [M][L^2]$$
$$u = v = [L][T^{-1}]$$
$$C_f = C_r = [M][L][T^{-2}]$$
$$\delta = \theta = dimensionless\ !$$

Based on the above dimensions the base units are chosen to be MLT.

Step 3: Determine the # of Pi groups

This step requires a simple application of the Buckingham Pi theorem.

Example:

For the bicycle model example, Buckingham gives;

$$n = number\ of\ system\ variables$$
$$r = minium\ number\ of\ base\ dimensions$$

Therefore

$$\# \ of \ \Pi = n - r$$
$$\# \ of \ \Pi = 12 - 3$$
$$\# \ of \ \Pi = 9$$

Step 4: Select the # of repeating variables to be used to define Pi groups

The only requirement is that all reference dimensions must be present in the repeating variables and that the variables are dimensionally independent.

Example:

For the bicycle model the variables are chosen to be;

$$Repeating \ Variables = u, m \ and \ l$$

Step 5: Calculate Pi groups

The Pi groups are generated by multiplying the non-repeating variables with the repeating variables and determining the exponents of the repeating variables that make their product dimensionless. This is easier to see when applied to an example.

Example:

Considering the bicycle model the Pi groups are calculated as follows;

Note that δ and θ are dimensionless and therefore are automatically Pi groups.

Therefore,

$$\Pi_1 = \delta \quad and \quad \Pi_2 = \theta$$

Using x:

$$x \cdot m^a \cdot u^b \cdot l^c \ = \ [L][M]^a[L]^b[T^{-1}]^b[L]^c$$

Equating exponents,

$$[L] \quad 1 + b + c = 0$$
$$[M] \quad a = 0$$
$$[T^{-1}] \quad b = 0$$

Solving,

$$a = 0, \quad b = 0, \quad c = -1$$

Chapter 2: Literature Review | Andrew Liburdi

Therefore,

$$\Pi_3 = \frac{x}{l} \quad \rightarrow \quad \Pi_4 = \frac{y}{l} \quad \rightarrow \Pi_5 = \frac{a}{l}$$

This implies that all geometric scaling can be performed by dividing the desired dimension by the wheelbase!

Using I_{ZZ},

$$I_{zz} \cdot m^a \cdot u^b \cdot l^c = [M][L]^2[M]^a[L]^b[T^{-1}]^b[L]^c$$

Equating exponents,

$$[M] \quad 1 + a = 0$$
$$[L] \quad 2 + b + c = 0$$
$$[T^{-1}] \quad - b = 0$$

Solving,

$$a = -1, \quad b = 0, \quad c = -2$$

Therefore,

$$\Pi_6 = \frac{I_{zz}}{ml^2}$$

Similarly, using v, C_f, and C_r gives,

$$\Pi_7 = \frac{v}{u}, \quad \Pi_8 = \frac{C_f l}{mu^2}, \quad \Pi_9 = \frac{C_r l}{mu^2}$$

It should be noted that the form of the Pi terms that were obtained above depends on the somewhat arbitrary selection of repeating variables and therefore are not unique [20]. However, the required number of Pi terms is fixed based on Buckingham [21]. A common question that arises with any dimensional analysis is, "which form of the Pi terms is the best?" There are no simple answers to this question and it is usually a matter of which is easier to control during experiments [20]. In the case of the bicycle model, longitudinal velocity and wheelbase were selected, since they are parameters that are chosen when setting up the vehicle for testing.

2.3 Scaled Vehicle Dynamics

The majority of the literature that deals specifically with scaled vehicle dynamics involves the use of a roadway simulator. A roadway simulator is a test bed in which a scale vehicle traverses a moving roadway. A treadmill or conveyor is usually the method of choice to implement the movable road surface. Research using roadway simulators has been conducted at several institutions including the United States Naval Academy [23], Auburn University [24], University of Michigan [25], and Bosch R&D [26] [27]. However, two institutions that have

been the most active in this area have been the University of Urbana-Champaign [*28*] and Penn State University [*29*]. In fact, the premise of this thesis, to a large extent was based on early work of Brennan et al at Urbana-Champaign [*22*], [*30*], [*12*] and Penn State [*29*].   Therefore those setups will be highlighted below.

2.3.1 Illinois Roadway Simulator: University of Urbana-Champaign

Some of the most critical work published on scale vehicle dynamics was conducted at Urbana-Champaign on the Illinois Roadway Simulator (IRS) [*22*], [*28*]. The test setup shown in Figure 7 consisted of a standard treadmill on which a 1/10 scale RC vehicle rode. Lateral positioning control was implemented by adjusting the treadmill speed and the vehicle's servo steering system to ensure that it remained on the road surface at all times [*22*].

Figure 7: IRS roadway simulator – University of Urbana-Champaign

Roadway consists of standard treadmill which is electronically controlled to maintain its velocity. A sensor arm is physically attached to the 1/10th scale vehicle in order to measure its position and orientation with respect to an absolute coordinate system. Figure was taken from Brennan [*3*].

State feedback measurements are accomplished with the use of a sensing arm. The arm is made up of three revolute joints, whose rotations are measured using encoders located at each joint. The joint motions were used to back calculate the vehicle's x, y, yaw, roll and pitch motions [*31*]. Due to the size of the treadmill, the vehicle was limited in terms of its lateral range

of motion. Therefore, it was not possible to evaluate highly aggressive manoeuvres, such as those commonly used for testing nonlinear vehicle response or emergency situations.

Even though the test bed was primarily limited to evaluating a vehicle's linear response, key observations were made about the adequacy of using virtual models to predict scale vehicle behaviour. Some of the key observations are highlighted below.

I.   Results conducted on IRS showed good correlation with the linear bicycle model in both the frequency and time domains.   The model dynamics were also very similar to those of actual full sized vehicles found in the literature, thereby validating the scale vehicle approach [*22*].

II.   Early difficulties with correlating the scale vehicle's frequency response were due to the limited bandwidth of the standard servo controlled steering system. A higher bandwidth servo was installed which eliminated the rate limitation [*22*]. Therefore, actuator dynamics are an important factor and should be carefully considered when designing a scale vehicle system [*31*].

III. All testing was conducted using manoeuvres that ensured that the scale tires remained within their linear range [*1*].

Brennan et al showed that a scale test bed was a valuable tool to test a vehicle's dynamic performance, provided the tires are operating within their linear range (i.e., not saturated).

2.3.2 PURRS: Penn State University

The most recent research published on scale vehicle dynamics was under the supervision of Brennan at Penn State University [*29*]. The setup used was called PURRS, which was an evolution of the IRS and is illustrated in Figure 8. The PURRS consists of a much larger conveyor, approximately 3.7m long and 2.1m wide. It has the added benefit that the road surface can be articulated in both pitch and roll, with ranges of +/- 25° of roll and +/- 6° of pitch [*29*]. The articulation of the roadway allows for researchers to input lateral loads into the vehicle's tires based on roadway inclination, thereby allowing for a much larger dynamic range of testing. The system used a sensing arm similar to the one on the IRS, in order to measure the vehicle's state feedback. It also used custom built scale vehicles, which were designed based on the Pi parameters derived from a 1992 Mercury Tracer [*29*].
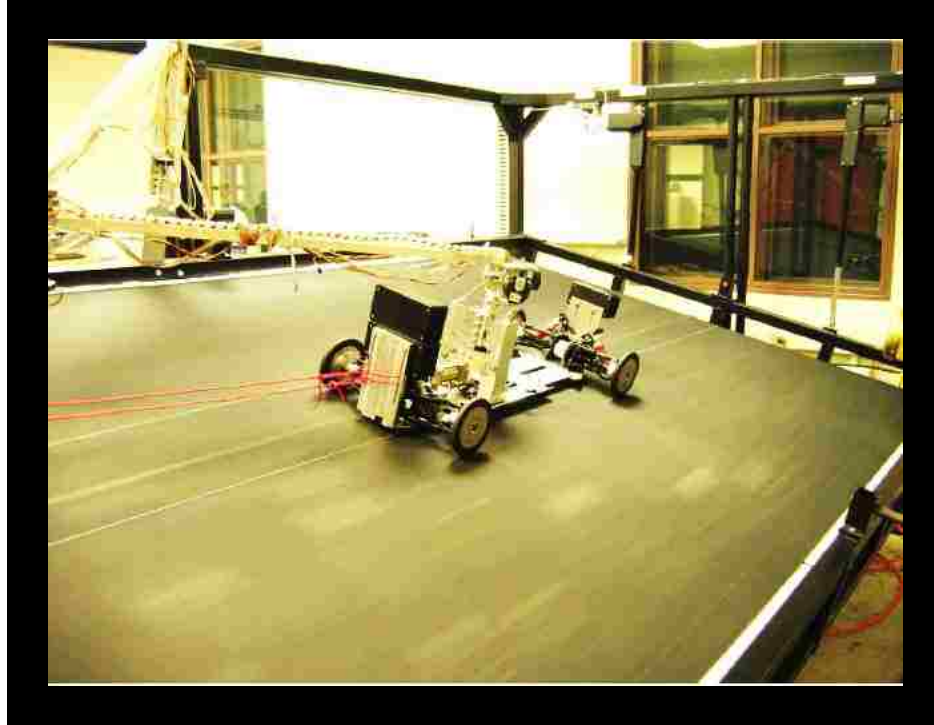
Figure 8: PURRS roadway simulator – Penn State University

The roadway is implemented using a large conveyor measuring 3.7 m long X 2.1 m wide. It is also possible to articulate the roadway in both the pitch and roll directions. A sensing arm is physically attached to the vehicle to measure its position and orientation with respect to an absolute coordinate system. Figure was taken from Lapapong et al [*29*].

With the added range of motion of this simulator, it was possible to test a wider range of vehicle behaviour, which included roll dynamics, as well as manoeuvres that operated within nonlinear range of tire performance. Research conducted on the PURRS was the first to attempt to directly match the planar dynamic performance of scale sized vehicles to a specific full sized vehicle [*29*]. Some of the key findings that were obtained are highlighted below.

I.   Results of the research showed good agreement between scaled and full sized vehicle response for low to intermediate input frequencies [*29*]. Good correlation was evident for low and high amplitude inputs across most of the frequency range.

II.   At higher frequencies, significant error was observed between the scale and full sized vehicles. This was attributed to the incorrect matching of tire lag dynamics [*29*]. It is well known that for full sized vehicles, the generation of tire forces is a function of time. This is due to the flexibility of the tire structure and sidewall stiffness [*8*]. However, the scale tires used for testing were made of solid rubber and were therefore too stiff in relation to their size [*29*]. This minimized or eliminated any tire lag dynamics in the scale vehicle response and resulted in poor correlation at higher frequencies.

The research clearly showed that scale vehicles are useful in the design and testing of chassis controllers that primarily use low to medium frequency inputs. The remarkable agreement of the scale and full sized responses stressed the repeatability and determinism of scale vehicle testing and validated their use [*29*].

2.3.3 Scale Tire Testing

Most of the research that has been presented thus far has dealt with vehicles which operate within the linear range of tire performance. It was shown using PURRS that due to tire lag dynamics, poor correlation between scale and full sized vehicles were obtained at high frequencies. In order to achieve better correlation it is necessary to demonstrate the ability of scale vehicles and dimensional analysis to extend beyond the linear model and encompass some of the system's nonlinearities [*32*]. The most important nonlinearity associated with a vehicle dynamic study is the force producing characteristics of the pneumatic tire [*10*].

In an effort to expand scale vehicle research to include nonlinear dynamics, Polley constructed a scale tire tester, similar to those used to test real automotive tires [*30*]. Du-Bro model air plane tires, with sizes ranging between 4.5" to 6.0" in diameter were used because they were pneumatic and shared similar cross-sectional shapes with that of real automotive tires. The one difference between the Du-bro and full sized tires was that the Du-Bro tires lacked any ply or belt structure which makes up the carcass of modern radial tires.
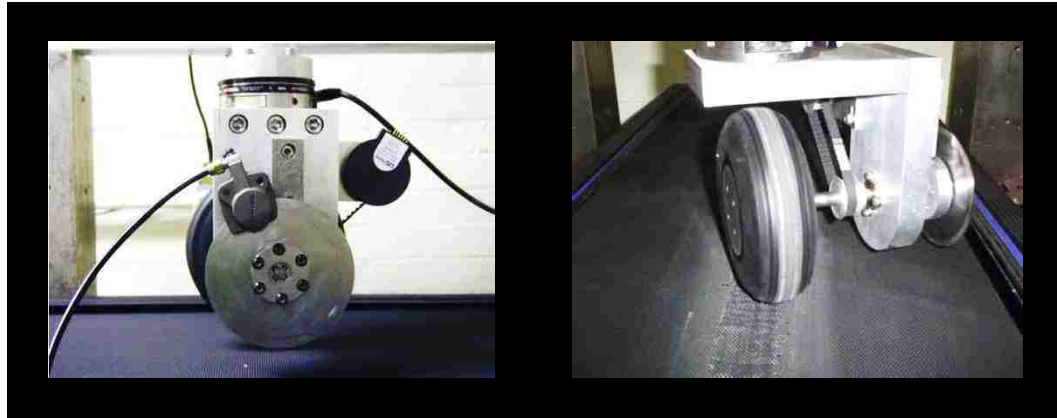
(a)   (b)

Figure 9: Scale tire tester – University of Urbana-Champaign

Scale tire testing being conducted using Du-Bro model air plane tires. Testing is carried out over a range of slip angles and normal loads. Contact patch forces and moments are measured using a 6 DOF force transducer. A disc brake is applied in order to generate braking forces and measure the tire's longitudinal performance. Figures were taken from Polley [*30*].

Tests conducted on the scale tire included measurements of lateral force, longitudinal force, and aligning moment. These measurements were taken over various normal loads and slip angles. This method of testing is a standard approach used when manufacturers publish data. The following observations were obtained.

I.   Analysis of scaled tire response showed very good resemblance with data published for similar testing conducted on full sized tires [*30*]. It was shown that the shape of the scaled steady state response, for both lateral force and self-aligning moment, closely resembled that of full sized tires, only differing in scale.

II.   A dimensional analysis was performed on key tire parameters and the Pi groups derived. It was found that the distributions of the scale Pi groups and that of full sized tires are nearly identical, indicating a quantitative matching between scale and full size tire response [*30*].

III.   It was concluded that the force producing characteristics of scaled pneumatic tires can exhibit similitude with full size tires. The results can be used to design scale vehicles which exhibit dynamic similitude for both the linear and nonlinear regions of tire performance.

The research that was conducted by Polley is very encouraging because it showed that the scaled pneumatic tire response was similar to that of full sized tires. This allows for dynamic

similitude to be extended to the nonlinear regions of vehicle performance and expands the usefulness of scale vehicle testing overall.

2.4 Non-Dimensional Control

It has been shown that scale vehicles can be designed to be dynamically similar to their full sized counterparts. Also, scale tire responses have been shown to closely match those of full sized tires, allowing scale vehicle research to be conducted within both the linear and nonlinear regions of vehicle behaviour. This close correlation between scale and full sized vehicles is critical because it results in a realistic vehicle model that can be used for controller design. However, the scale vehicles would not be of much use unless the controllers developed on these systems can be implemented on the full sized vehicle. Fortunately research conducted at Urbana-Champaign [*1*], showed that controllers developed in a non-dimensional framework, not only scale properly, but also result in simpler control definitions and a less conservative control function when compared to dimensioned methods [*3*].

2.4.1 Robust Control

One popular area of control research where non-dimensional methods have been shown to be valuable is in robust control.   Robust control theory attempts to create control algorithms that are designed to tolerate system variability. The variability can be due to variation in system properties, such as a change in vehicle mass due to different payload conditions, or due to external disturbances that affect a system's response, such as wind or road irregularities [*3*]. This compensation is accomplished by defining system parameters in terms of statistical distributions.

Brennan applied robust control methods to a scale vehicle system and tested them using the IRS. He showed that the dimensionless framework afforded a lower level of uncertainty in parameter descriptions, when compared to a dimensioned system approach [*3*]. He also showed that a single dimensionless controller is able to stabilize a large range of vehicle sizes, after the appropriate rescaling of individual vehicle dimensions [*33*]. This approach resulted in tighter uncertainty bounds in the definition of the system model and therefore results in a less conservative controller overall [*3*].

2.4.2 Gain-Scheduling

Another area in which dimensionless system representations are advantageous is gain scheduling. Gain scheduling is used when a single system model is inadequate at predicting system behaviour throughout its whole operating range [15]. The method includes changing routines that switch control gains as a function of operating conditions or by interpolating different control laws. The task of controller design grows exponentially more difficult with the number of gain scheduling variables used to define the switching structure [3]. Dimensional analysis simplifies the design task since a dimensionless representation has a reduced variable space and therefore fewer gain scheduling parameters are needed. Brennan [3] demonstrated this through an example of a gantry system.

2.5 Research Objectives

It has been shown above that scale vehicle testing is an attractive alternative when developing controllers. It provides many advantages, such as reduced costs, decreased setup time and the flexibility to test more aggressive control laws without fear of injury or damage to property. Research in this area has shown that scale testing is a valid method in which to test a vehicle's handling dynamics, since the results gained from the scaled system can be applied to full size vehicles.

Up until now, scale testing has been performed on roadway simulators which are tethered to the vehicle in order to measure its state feedback. Despite recent improvements to the PURRS system, the vehicle is still forced to travel within a small area, which limits the type of manoeuvres that can be performed. For example, aggressive manoeuvres, such as those commonly used for evaluating rollover performance are not possible on these systems.

The main goal of this research was to develop a scale test bed that could be used to investigate the limits of vehicle handling, with a specific emphasis towards controls development. To conduct such testing it was necessary to ensure that the vehicle was free to conduct any manoeuvre that the researcher intended. In order to accomplish this task it was necessary to develop a custom acquisition module which could be fully contained within the vehicle package. In caparison with roadway simulators, the test bed developed here is unique in that the vehicle is untethered from the acquisition system, which leads to some obvious advantages.

The first advantage is that all control and acquisition systems are contained within the vehicle itself and therefore it is not necessary to designate any lab space for the test bed. This

allows the system to be portable and testing can be conducted anywhere there is enough area to carry out the manoeuvres. Second, there are no restrictions on the type of manoeuvres that can be used and therefore the complete nonlinear response of the vehicle can be investigated. Finally, the use of the test bed can be extended to other types of research, such as path tracking or autonomous vehicle control applications.

Chapter 3: Vehicle Modeling

3.1 Model Vehicle

In order to properly conduct scale vehicle testing it was necessary to find a vehicle system that would approximate the operation of a full sized vehicle. Apart from needing to be properly scaled in dimension, the vehicle system needed to be re-configurable, incorporate a suspension/chassis system of the same architecture and have a powerful enough drive system that would allow it to perform aggressive testing manoeuvres. Due to cost and time constraints it was decided that an off the shelf vehicle would provide the best value, as well as minimize any development time associated with system setup.   With these criteria in mind, the Traxxas E-Maxx, shown in Figure 10, was selected as the test platform of choice due to its popularity and feature set.
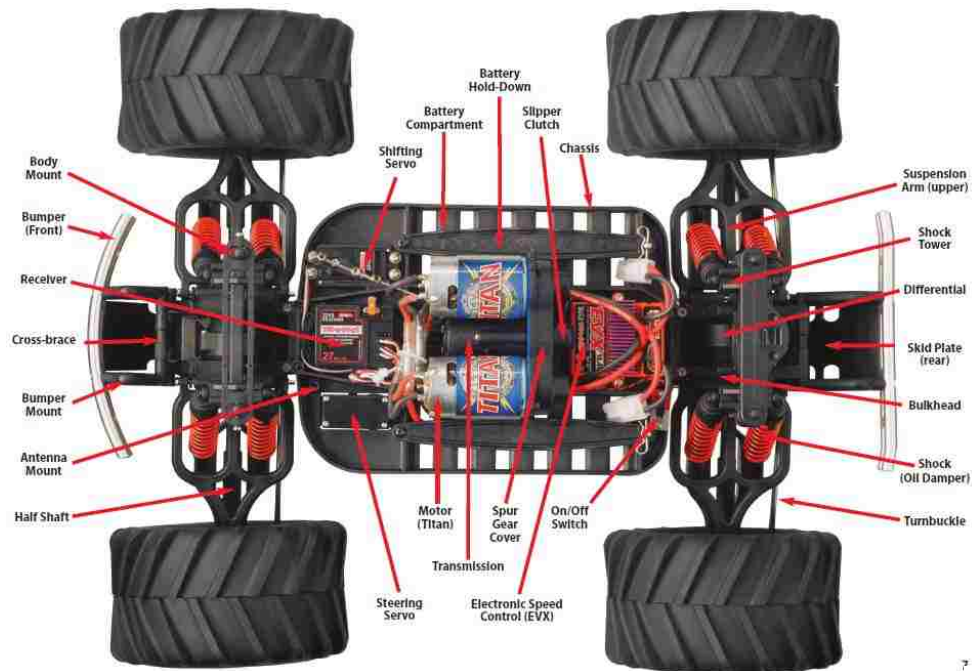
Figure 10: Traxxas E-Maxx scale vehicle

Above figure depicts a top view of the Traxxas E-Max RC vehicle. Key components are highlighted throughout the vehicle, including the wireless receiver, electronic speed control unit and Titan 550 motors. Vehicle chassis consists of a double wishbone suspension system with coil springs and hydraulic dampers. Figure was taken from the E-Maxx user manual [*34*].

The E-Maxx's features include 4-wheel drive, a shift on the fly two – speed transmission and twin Titan 550 motors which provided ample drive torque for the intended application. The

E-Maxx also incorporates a fully independent double wishbone suspension system that utilizes hydraulic dampers with coaxial springs to control body motions. Overall, the vehicle system closely resembles that of a full size vehicle and therefore made the E-Maxx an ideal platform with which to conduct this research. However, certain modifications needed to be made to ensure that the vehicle system produced realistic and repeatable behaviour. These modifications will be highlighted in the subsections that follow.

3.1.1 Steering Servo

One of the key findings that were made from the research conducted on the IRS was that the dynamics of the steering actuator played a pivotal role in the overall response of the vehicle. Specifically, it was found that the standard steering servo installed on the RC vehicle was too sluggish and introduced a rate limitation to the system [22]. Therefore, the dynamic response of the vehicle was not dictated by the chassis but rather how fast the steering servo could respond to commands. Based on these findings, it was decided early on to mitigate these effects by using a faster servo in order to avoid the introduction of a rate limitation. The Futaba S9402 is a high speed servo with a maximum rate of 0.10 sec/60° and a torque capacity of 78.48 N·m. This servo was also used on the IRS roadway simulator and was shown to be sufficiently fast to avoid any rate limitation [22]. Installation of the servo was straight forward and required no modification to the vehicle chassis or special hardware.

3.1.2 Tires

It has already been discussed that the most important aspect of vehicle handling is the response of the tire. It follows that the selection of the scale tire was an important factor in achieving realistic handling behaviour. The standard tires supplied with the E-Maxx are foam filled and use tread that consists of large lugs as shown in Figure 10. This configuration was not deemed to be representative of real automotive road tires and the confidence that they would produce realistic traction forces was low. Fortunately, Polley showed that the Du-Bro line of pneumatic model air plane tires exhibited the same traction force characteristics as full sized tires [30]. Therefore, the more realistic Du-Bro tire was chosen and the 5.0" diameter version used.

A comparison of the two tires is shown in Figure 11. It can be seen from the figure that the Du-Bro tire is much closer to full size tires in terms of tread, cross-sectional area and structure. This made the Du –Bro tire the better choice with which to conduct this research. Another

advantage of the Du-Bro tire was that Polley [*30*] had published detailed data on their performance which could be used when creating virtual models of the vehicle.

Figure 11: Du-Bro tire vs stock E-Maxx tire comparison

Tire on the left illustrates the 5" Du-Bro pneumatic tire used within this research. The tire on the right illustrates the stock E-Maxx tire. The stock tire is foam filled and consists of large lugs which will not allow the tire to produce realistic traction forces. The Du-Bro tire has been shown within the literature to closely match full size tire response once the proper scaling factors are applied.

In order to mount the Du-Bro tires, the E-Maxx wheel adapters needed to be modified, as illustrated in Figure 12. This was accomplished by drilling holes in both the hexagonal wheel adapter and Du-Bro rim which were used to hold wheel studs. The studs allowed the torque from the axle shaft to be transmitted to the wheel rim efficiently. The whole assembly is held together with a 23 mm long stud, internally threaded such that it passes through the Du-Bro rim and screws on to the E-Maxx Spindle. All machining was performed on a Bridgport mill, with attention given to ensure that all of the holes were machined true in order to prevent any wobbling when the tire rotates.

Figure 12: Modified E-Maxx wheel assembly

To accept the Du-Bro tire the hexagonal wheel adaptor shown above was drilled out and studs installed. A mating set of holes were drilled into the Du-Bro rim and the whole assembly was held together using a 23mm long bolt. The bolt was internally threaded to screw onto the E-Maxx spindle.

3.2 Vehicle Properties Characterization

In an effort to create the most accurate vehicle models possible, it was necessary to characterize the vehicle's inertial properties. The main properties that were measured included the center of gravity and the mass moments of inertia for all three rotation axes. The methods used to collect these parameters are highlighted within the following subsections.

3.2.1 Planar CG Location

Determining the longitudinal and lateral location of the vehicle's CG is a straight forward procedure. It involves measuring the vehicle corner weights and using moment balance equations to determine the CG location. Due to the small size of the vehicle, kitchen scales were used to measure the corner weights to a resolution of 0.001 kg.

(a)	(b)
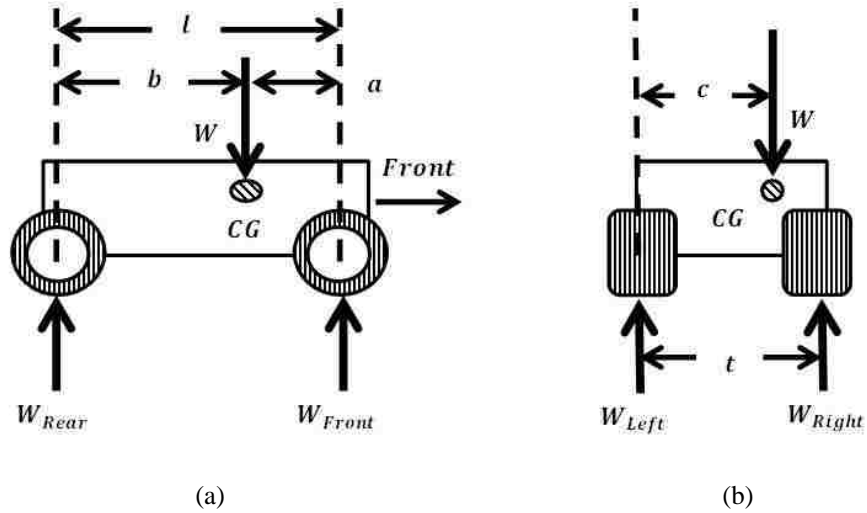
Figure 13: Longitudinal and lateral CG location FBD's

Figure (a) is used to conduct a moment balance in order to determine the longitudinal CG location. A moment balance conducted on the figure in (b) obtains the lateral CG location. The weight at each wheel was obtained using scales.

Performing a simple force/moment balance on the above FBD's results in the following expressions for the lateral and longitudinal CG location.

Longitudinal CG
Position:

$$a = \frac{W_{Rear}}{W} l \quad , \quad b = \frac{W_{Front}}{W} l \tag{9}$$

Lateral CG Position:

$$c = \frac{W_{Right}}{W} t \tag{10}$$

Ten samples of corner weights were used to calculate the CG position and their average taken. The CG location along with the standard deviation of each parameter is presented in Table 2.

.

Table 2:   CG location parameter values

Parameter	Value	Standard Deviation	# of Samples
Weight (N)	45.92	0.040	10
F/R Ratio	0.895	0.009	10
a (mm)	164	0.805	10
b (mm)	147	0.805	10
c (mm)	178	0.978	10

It should be noted that the significant digits for each parameter were determined based on the standard deviation. As can be seen from Table 2 the CG position dimensions have standard deviation values close to one. Therefore, the value of these dimensions can only be accurate to the nearest millimeter. This is not a major concern since the mean values are orders of magnitude larger than the deviation.

3.2.2 Inertial Tester

Measuring the mass moment of inertia of the vehicle required a more elaborate test apparatus than was required for the CG location. Methods commonly used to measure the inertia of an object include the Trifilar pendulum, mass tables and free vibration. The free vibration method was chosen due to its simplicity. This method is based on the damped sinusoidal motion of an object subjected to free torsional vibration. The natural frequency with which the object oscillates is proportional to the mass moment of inertia about the axis of rotation. A brief development of the equations used to determine the vehicle's inertia is presented below. The interested reader needing a more detailed analysis can refer to Inman [*35*] or any other introductory vibrations text.
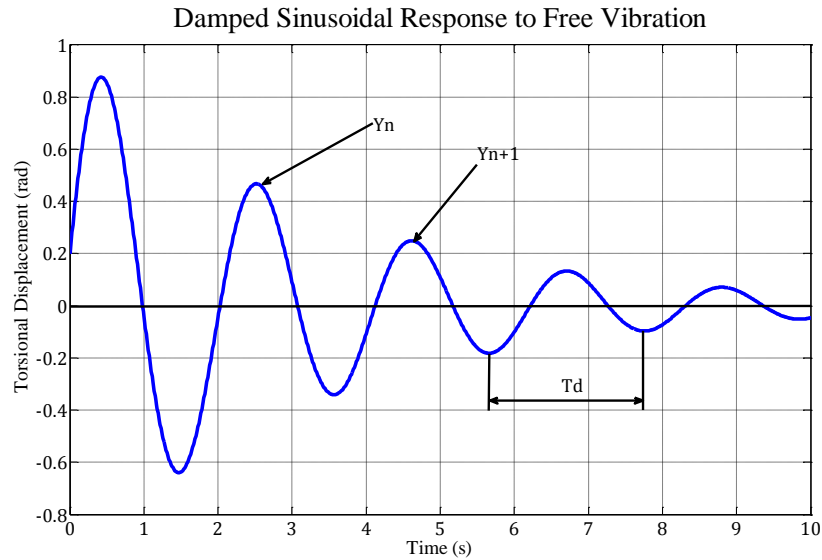
Figure 14: Typical damped torsional free vibration response

Signal illustrated above represents the typical response of an object undergoing torsional free vibration. Yn and Yn+1 denote successive peaks which are used to estimate the system's damping. The frequency of vibration is proportional to the mass moment of inertia of the vibrating object.

The torsional free vibration of a mass shown in Figure 14 is governed by the following equations of motion. Note that it is assumed that the system is governed by a linear ODE (Equation 11) and therefore all coefficients, including the damping ratio and system stiffness are assumed to remain constant.

Free Vibration
Equation of Motion:

$$I\ddot{\theta} + 2I\zeta\omega\dot{\theta} + k\theta = 0 \qquad (11)$$

Torsional
Displacement:

$$\theta = \rho e^{-\omega\zeta t}\cos(\omega_D t + \gamma) + C \qquad (12)$$

Where,

$\theta = torsional\ displacement$
$I = mass\ mometn\ of\ inertia\ about\ axis\ of\ rotation$
$\zeta = damping\ ratio$
$\omega = natural\ frequency$
$\omega_D = damped\ natural\ frequency$
$k = torsional\ stiffness\ of\ system$
$\rho = amplitude$
$\gamma = phase\ shift$
$C = Constant$

The damped natural frequency can be related to the mass moment of inertia by the following equations.

$$\omega_D = \omega\sqrt{1 - \zeta^2} = \sqrt{\frac{k}{I}}\sqrt{1 - \zeta^2}$$

Mass Moment of
Inertia:

$$I = \frac{k(1 - \zeta^2)}{\omega_D^2} \tag{13}$$

Parallel Axis
Theorem:

$$I_O = I_{CG} + mR^2 \tag{14}$$

Where;

$I_O = moment\ of\ inertia\ about\ axis\ of\ rotation\ of\ tester$
$I_{CG} = moment\ of\ inertia\ about\ the\ CG$
$R = perpendicular\ distance\ between\ O\ and\ CG$
$m = mass\ of\ vehicle$

The damping ratio shown in Equation 11 can be found using the logarithmic decrement method. Referring to Figure 14 the amplitude ratio of successive oscillations is related to the damping ratio through the following relationship.

Logarithmic
Decrement:

$$\delta = ln\left(\frac{y_n}{y_{n+1}}\right) = \frac{2\pi\zeta}{\sqrt{1 - \zeta^2}} \tag{15}$$

Damping Ratio:

$$\zeta = \sqrt{\frac{1}{\frac{4\pi^2}{\delta^2} + 1}} = \sqrt{\frac{\delta^2}{4\pi^2 + \delta^2}} \tag{16}$$

In order to measure the damped sinusoidal response of the vehicle, a test fixture was built as illustrated in Figure 15. The fixture consists of a simple wooden frame to support the weight of the vehicle as it is suspended from a straight shaft. Brackets were fabricated to allow the vehicle to be squarely mounted to the fixture. The shaft is connected to a potentiometer in order

Chapter 3 : Vehicle Modeling | Andrew Liburdi

to measure its angular displacement. Torsional stiffness is provided by a torsional spring mounted co-axial to the shaft with one end reacted against the wooden frame.
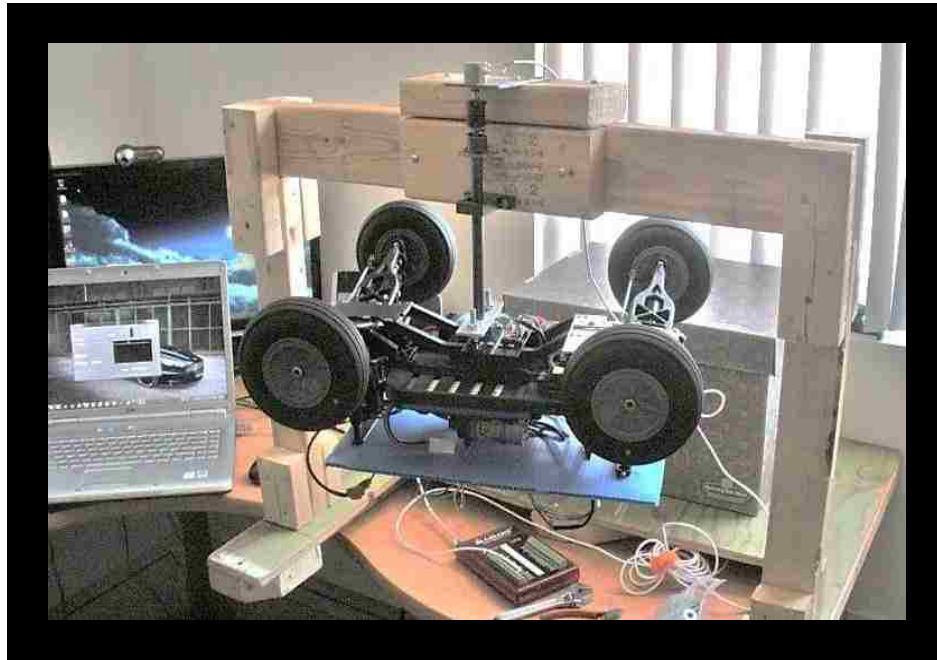
Figure 15: Inertial tester

Fixture used to subject vehicle to torsional free vibration. Potentiometer mounted to shaft records angular displacement as a function of time. The frequency of oscillation is proportional to the mass moment of inertia of the vehicle about the rotation axis.

Before measurements could be made, it was important to calibrate the test fixture and determine the system's torsional stiffness. This was accomplished by attaching a force meter to the shaft at a fixed distance from the center of rotation. The force needed to rotate the shaft over various angles was recorded and the torsional stiffness obtained. These measurements were taken several times with a high degree of repeatability. As can be seen in Figure 16, the results show that the torsional stiffness is constant and therefore the equations that were presented above are applicable to this system. After performing a linear regression analysis, the torsional stiffness of the system was found to be;

Torsional Stiffness:
$$K_{Torsion} = 5.3968 \, N \cdot mm/deg \qquad (17)$$

Torsional Spring Stiffness
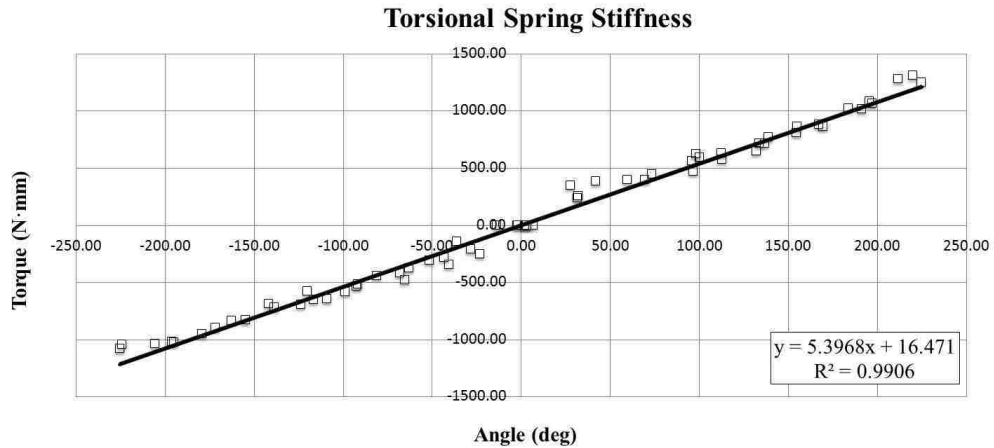
Figure 16: Inertial tester system stiffness calibration

The stiffness calibration curve was constructed my measuring the torque required to rotate the shaft over several angular positions. The curve above indicates that the system stiffness is linear and therefore satisfies the assumptions associated with the free vibration problem. The resulting system stiffness is shown to be 5.3968 N· mm/deg.

Data collected on the inertial tester consisted of torsional displacement measurements taken with the potentiometer. The vehicle was rotated both clockwise and counter-clockwise, with the measurements averaged in order to eliminate any bias. Analysis of the data required the use of a MatLab script which imported the data, corrected for phase shift and fitted a damped sinusoid in the form of Equation 12. Using the coefficients obtained from the curve fit and Equations 13and 14, the mass moment of inertia was obtained. Because the rotation axis of the inertial tester was offset from the vehicle's CG, the parallel axis theorem was used to convert the inertia measurements to those about the vehicle CG. It should be noted that performing this conversion resulted in CG inertias that were within 0.8% of the original measurement and therefore inertial tester measurements can be taken as the CG inertia directly.

Figure 17 shows the results obtained for clockwise measurements. It illustrates that the fitted damped sinusoidal model is extremely accurate at defining the torsional displacement of the system. Similar agreement between the regression model and counter clockwise data was also found. Table 3 lists all three moments of inertia obtained for the vehicle as well as their standard deviations. The low standard deviations indicate that the measurements were highly repeatable and provide a high degree of confidence in their results.

Table 3: Mass moment of inertia measurements

Parameter	Mean Value	Standard Deviation
I_{zz} $(kg \cdot m^2)$	0.093	0.0004
I_{xx} $(kg \cdot m^2)$	0.060	0.0008
I_{yy} $(kg \cdot m^2)$	0.05	0.006
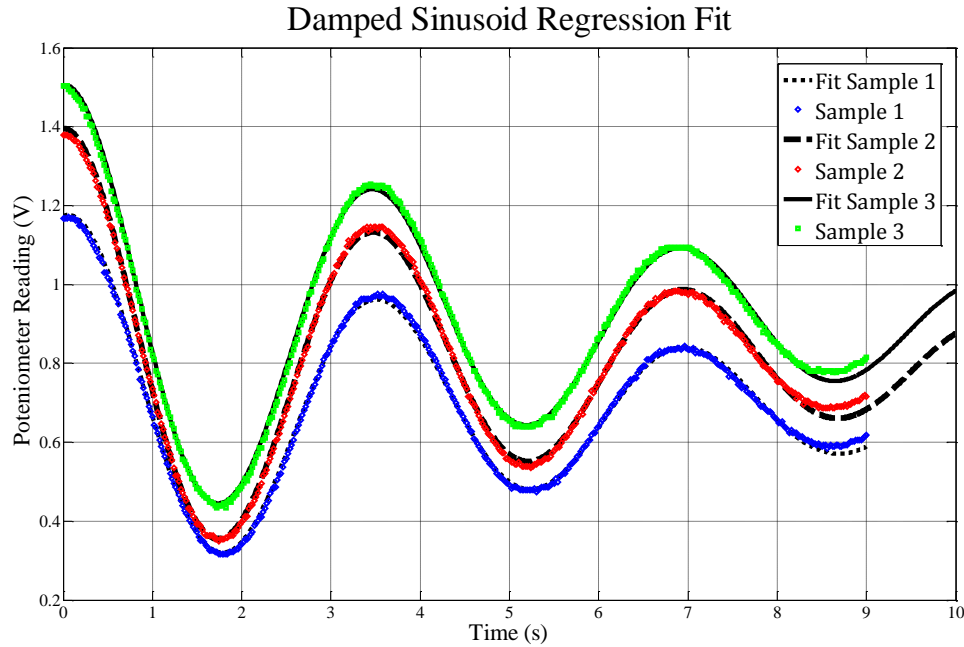
Figure 17: Regression analysis – I_{zz} estimated from free vibration response

Regression analysis fitted a damped sinusoidal wave form to the free vibration data . As can be seen the free vibration model provides an extremely good fit to the data and therefore validates the method used. From the regression model, the frequency of vibration was determined and used to calculate the mass moment of inertia of the vehicle.

3.2.3 *Π Parameter Analysis*

      Recall that the concept of similitude states that if two systems are governed by the same model and have equal Pi parameters, then they can be considered dynamically similar. Therefore observations obtained from one system can be used to predict the behaviour of the other system. To evaluate whether the E-Maxx is a satisfactory system to predict full sized vehicle behaviour, an analysis of its Pi parameters and how they relate to those of full sized vehicles is necessary.

                                                              Chapter 3 : Vehicle Modeling | Andrew Liburdi

Parameter Comparison:

It was shown previously using the method of repeated variables that the Pi parameters associated with the handling response predicted by the linear bicycle model are;

$$\Pi_1 = \frac{a}{l} \qquad \Pi_2 = \frac{b}{l} \qquad \Pi_3 = \frac{t}{l} \qquad \Pi_4 = \frac{C_\alpha l}{mu^2} \qquad \Pi_5 = \frac{I_{zz}}{ml^2}$$

By inspection the Pi parameters for other inertial properties can be shown to be;

$$\Pi_6 = \frac{I_{yy}}{ml^2} \qquad \Pi_7 = \frac{I_{xx}}{ml^2}$$

In order to properly determine if the Traxxas E-Maxx is a suitable test vehicle, full sized vehicle data was required to make Pi group comparisons. Fortunately, NHTSA published a survey of inertial properties for a wide range of vehicles [*36*]. This survey was used to determine the distribution of the above Pi groups for full sized vehicles. The data consisted of vehicles of all types ranging from small compact cars to large SUV's and trucks. Over 400 vehicles were included in the study giving a large sample size sufficient to make predictions about the larger population. Table 4 compares the Pi groups obtained for the E-Maxx and the mean values for the NHTSA vehicles. Note that Π_4 is not included because it depends on variables that need to be selected when developing the test and therefore is subject to change. The treatment of this parameter will be discussed separately in the following sections.

Table 4: Pi parameter comparison between E-Maxx and full sized vehicles

Pi Group	Traxxas E-Maxx	Full Vehicle Data (Mean)
$\Pi_1 = \dfrac{a}{l}$	0.54	0.445
$\Pi_3 = \dfrac{t}{l}$	1.12	0.550
$\Pi_5 = \dfrac{I_{zz}}{ml^2}$	0.21	0.250
$\Pi_6 = \dfrac{I_{yy}}{ml^2}$	0.4	0.243
$\Pi_7 = \dfrac{I_{xx}}{ml^2}$	0.135	0.051

To properly visualize how the E-Maxx compares with full sized vehicles, histograms for each Pi group obtained from the NHTSA survey are presented in Figure 18.
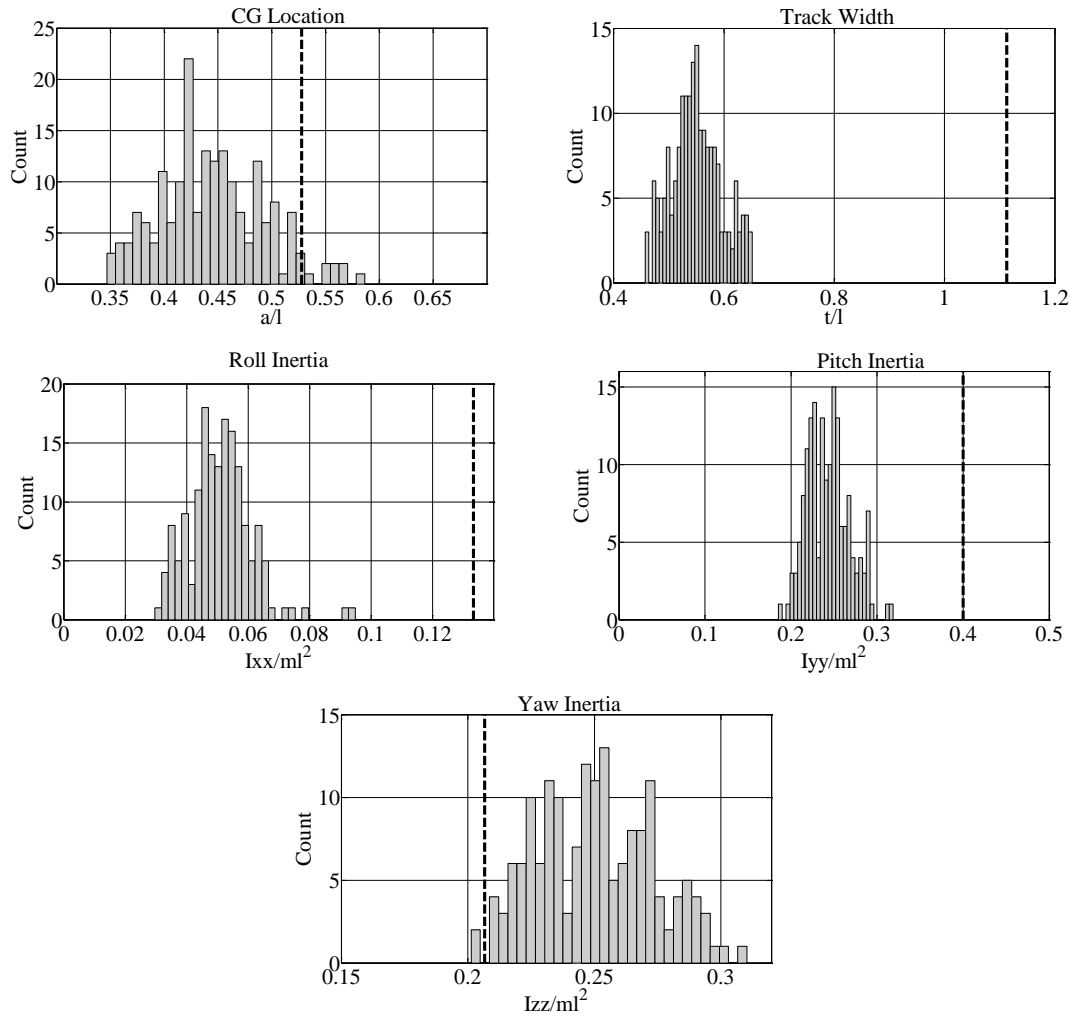
Figure 18: Pi parameter distributions

Histograms were generated from NHTSA data to determine the distribution of Pi parameters among the full size vehicle population. Dash line indicates the E-Maxx configuration which is outside of acceptable limits for all parameters except for longitudinal CG location.

It is seen from the above plots that the Pi parameters for the NHTSA data can be considered normally distributed. The longitudinal CG distribution shows that most of the vehicles are grouped around 0.425 which represent a front biased weight distribution. It will be shown in subsequent sections that the bicycle model predicts that vehicle handling is more stable with front heavy vehicle configurations and therefore manufactures tend to design this into their products for safety reasons. The E-Maxx is slightly rearward weight biased; however, it is still well within the range of values presented by the NHTSA data and can be considered consistent with full sized vehicles.

Though the CG location of the E-Maxx was shown to be consistent with the NHTSA data, the moment of inertia and track width Pi groups are shown to be inconsistent. The scaling of the track width is not representative because for the E-Maxx the track is actually greater than the wheelbase. This configuration is not realistic for use in full size vehicles because it would not provide enough occupant space. Also, the reduced wheelbase lowers high-speed stability and therefore manufacturers would be hesitant on implementing such a configuration. Unfortunately, it is not possible to easily change the track width or wheelbase of the Traxxas without completely fabricating new chassis components. Therefore, the track will be left in its original configuration and the inconsistency will be taken into account when analyzing any data collected with this vehicle.

Ballasting:

In order to improve the moment of inertia comparison, ballasting was used to manipulate the E-Maxx inertia in all three directions. This was accomplished by adding mass to the extremities of the vehicle's chassis. This resulted in increases to its inertia and weight while maintaining the CG location. The location and value of the ballast was varied using an iterative procedure and the use of a 3D CAD model to evaluate the new configurations. After some effort, a satisfactory configuration was found, which is illustrated in Figure 19. Figure 20 shows how the new configuration compares with the NHTSA data.
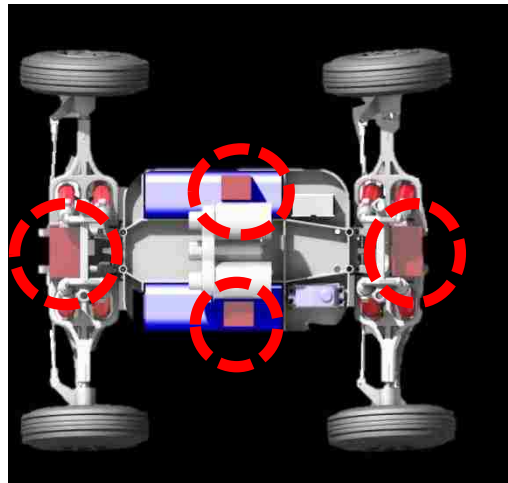
Figure 19: E-Maxx ballast configuration

Ballast placed at extremities of vehicle in order to alter inertial properties to better match full size vehicle population. Ballast distributed as follows: Front = 2 kg , Rear = 1.5 kg and Sides = 0.5 kg.
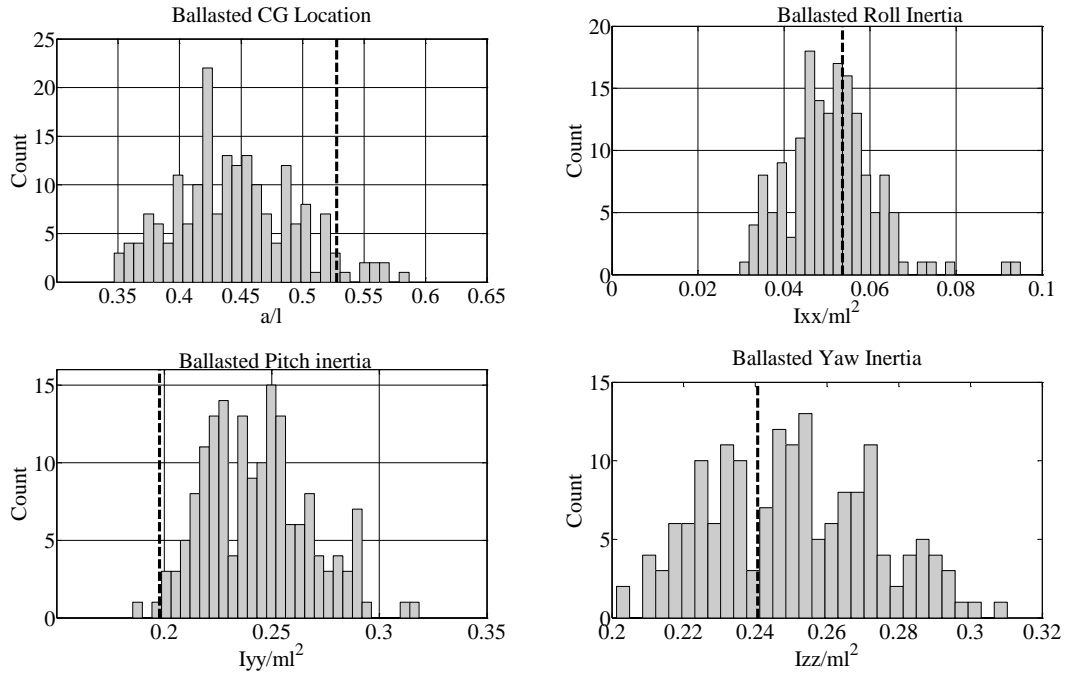
Figure 20: Ballasted Pi parameter distributions

It is seen that the ballasted E-Maxx configuration approaches the mean of the parameter distributions for I_{xx} and I_{zz}. I_{yy} has been improved from the baseline configuration and is now located at the lower tail of the distribution.

As can be seen from the above plots, the yaw and roll inertia are much closer to the NHTSA data. The pitch inertia is located at the tail end of the NHTSA data but is much improved when compared to the baseline configuration.

Π_4 Cornering Stiffness Scaling:

To ensure proper vehicle handling behaviour the scaled tire forces need to be representative of full sized vehicles. As a result the value of Π_4 is critical in determining if the Du-bro tires are adequate at predicting full sized tire behaviour. In order to make a proper comparison, tire cornering stiffness data was required. Fortunately, data for the Du-Bro tire was available due to the research conducted by Polley [30]. Obtaining manufacturer data on the other hand proved to be more difficult. However, limited data was found within various sources such as CALSPAN [37], the vehicle research laboratory at Delft University [30] and R.W. Allen [38]. The data included tire properties such as cornering stiffness, aspect ratio and max lateral load for over 90 tires.

An important aspect of Π_4 is that it is the only parameter that is dependent on the operating conditions of the vehicle. Specifically, the parameter can be manipulated by adjusting

the vehicle's forward velocity and therefore, Π_4 is used to properly scale the test velocity of the vehicle. In order to make a proper comparison, a forward velocity was needed for full sized vehicles. A particular area of interest in controls development, as well as, vehicle dynamics in general is the response of a vehicle at highway speeds. Therefore the forward velocity for the full sized vehicle was selected to be 100 km/hr. Mean values for both mass and wheelbase were taken from the NHTSA vehicle property survey to represent an average full size vehicle. Calculating the Pi parameters for the various tires within the published data, the distribution for Π_4 was obtained and is presented in Figure 21. Multiple forward velocities for the E-Maxx were used to determine an acceptable test speed to approximate full size tire performance.
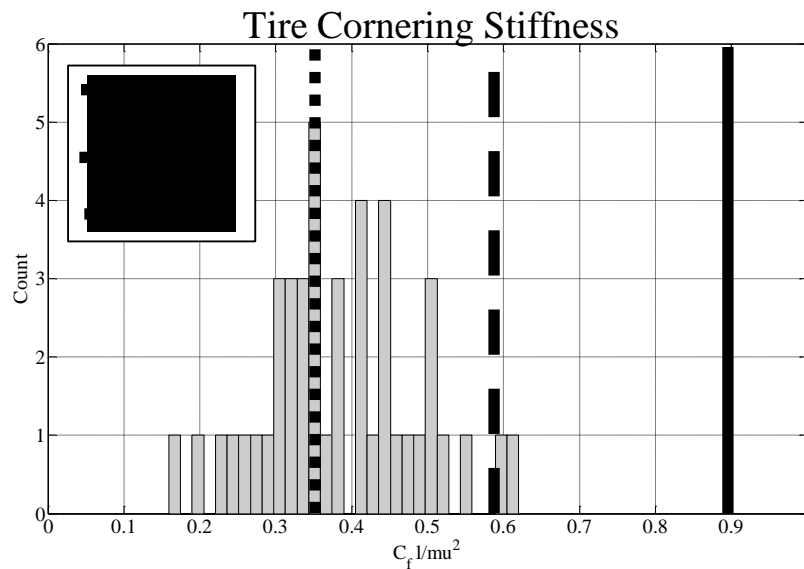
Figure 21: Cornering stiffness Pi comparison

Full size population histogram was created from several tire sources with vehicle dimensions taken as the mean values of the NHTSA data shown previously. The histogram was generated assuming a full vehicle speed of 100 km/hr. To properly scale the test to match the tire stiffness of the full size population, a test speed of 9 m/s is required.

As can be seen a forward velocity of 9 m/s is required to properly scale the Du-Bro cornering stiffness. There are some practical limitations associated with conducting experiments at such high speeds. First, the test area needed to conduct experiments is greatly increased when vehicle velocities are increased. Therefore it might not be possible to find an adequate test surface and may limit the type of testing that can be performed. Also, operating at these high velocities will tend to introduce high frequency nonlinear effects into the vehicle response. For example a small non-uniformity in the wheel or misalignment could result in a large amount of wheel wobble at high speed. Small road disturbances will be accentuated at high speeds which

could upset the vehicle resulting in a loss of control. These practical aspects will be discussed in more depth when discussing the development of the test manoeuvres.

3.3 Virtual Modeling

Even though scale testing is much easier and less time intensive than full sized testing, it is still more efficient to test new control methods using computer models. Therefore, to a large extent, the purpose of this research was to develop a virtual model that accurately represents the vehicle so control methods could be tested out prior to physical implementation. The following sections discuss the virtual modeling process that was used to characterize the vehicle both physically as well as dynamically.

3.3.1 Solid Modeling

One of the first tasks worked on was the creation of an accurate 3D CAD model of the E-Maxx. This provided several advantages moving forward. First, having the vehicle modeled allowed for test fitting of new parts and the analysis of changes to the vehicle configuration. Secondly, mass properties of individual components, as well as the whole vehicle itself could be estimated using the 3D model geometry and standard material property tables. Lastly, the CAD model allows the 3D geometry to be used for more advanced dynamic modeling techniques which would require the detailed geometry of each component. An advanced multi-body dynamics model developed using the ADAMS software package would be an example of a situation where the 3D CAD geometry could be imported and the inertial properties and kinematics replicated accurately.

The CAD model was developed with the use of CATIA V5, a powerful modeling suite used within the automotive and aerospace industries. The model was created by carefully measuring key features of each component and assembling them into the full vehicle assembly as illustrated in Figure 22.
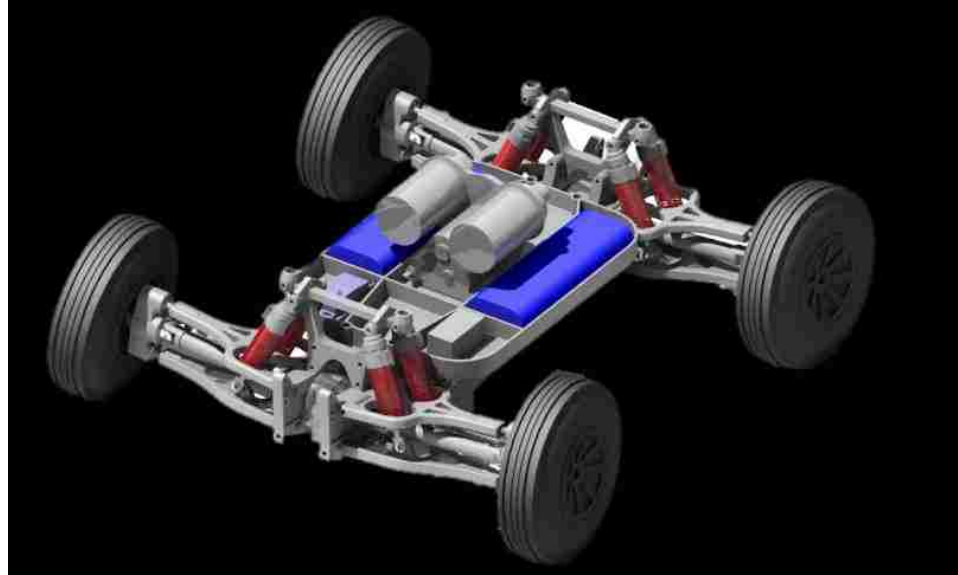
Figure 22: Traxxas E-Maxx CAD model

CAD model developed with CATIA V5. Key features of each component were modeled and assembled into the full vehicle model shown above. The model was used to evaluate various vehicle configurations as well as estimate inertial properties. CAD data can be imported into multi-body dynamics software packages, resulting in the accurate replication of component kinematics and inertial properties.

3.3.2 Linear Bicycle Model

The importance of the bicycle model has already been addressed within the literature review; however, it cannot be stressed enough that this model predicts the fundamental characteristics of vehicle handling. Miliken [*10*] showed that all subsequent nonlinear, steady state and transient response characteristics of vehicle handling are extensions of the linear behaviour predicted from this model. A detailed development of the bicycle model equations will be presented next.

Figure 23 illustrates the FBD of the traditional bicycle model. As can be seen the track width has been assumed to be zero, combining the front and rear tire forces into a single contact patch located in the middle of each axle. Also represented in Figure 23 is the body fixed coordinate system which is fixed to the vehicle and rotates with same yaw rate.
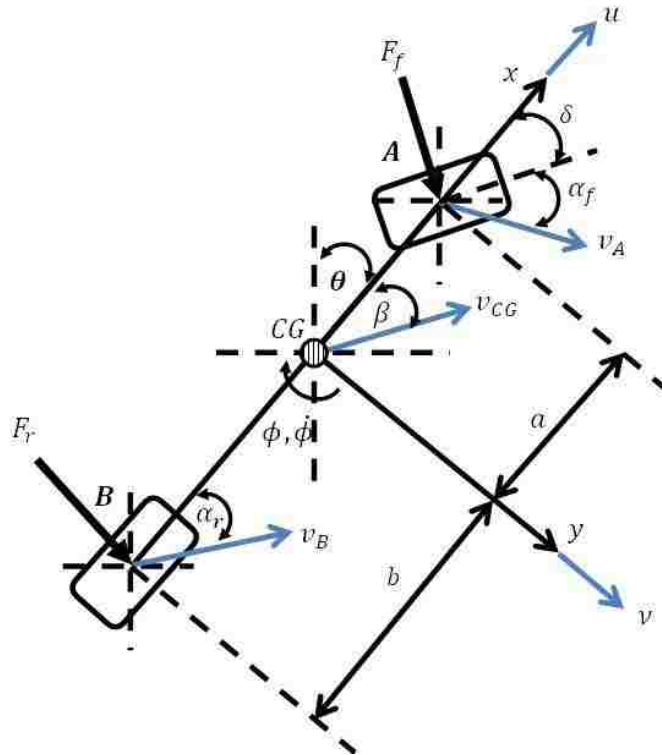
Figure 23: Linear bicycle model FBD

FBD used to develop the equations of motion for the linear bicycle model. A body fixed coordinate system is used which rotates with the same angular velocity of the vehicle. Traction forces at the front and rear axles are denoted by F_f and F_r respectively and are assumed to be linearly proportional to their slip angles.

Applying Newton's Laws on the FBD shown in Figure 23 gives;

Summing forces,

$$\sum \vec{F} = m\frac{d}{dt}\ (u\,\hat{\imath} + v\hat{\jmath})$$

Since the coordinate system is rotating

$$\sum \vec{F} = m[\dot{u}\,\hat{\imath} + \dot{v}\,\hat{\jmath} + \phi\hat{k}\ x\ (u\,\hat{\imath} + v\,\hat{\jmath})]$$
$$\sum \vec{F} = m\ [\ (\dot{u} - \phi v)\hat{\imath} + (\dot{v} + \phi u)\hat{\jmath}\ ]$$

Lateral Direction [$\hat{\jmath}$]:
$$F_f\ cos\delta + F_r = m\ (\dot{v} + \phi u)$$

If we assume that δ is small then $cos\delta \sim 1$

Therefore,

$$F_{front} + F_{rear} = m\ (\dot{v} + \phi u) \qquad\qquad (18)$$

Chapter 3 : Vehicle Modeling | Andrew Liburdi

Summing Moments about the CG gives;

$$\sum M_{CG} = I_{zz}\dot{\phi}$$

$$aF_{front} - bF_{rear} = I_{zz}\dot{\phi} \qquad (19)$$

In order to proceed the tire forces need to be defined. In an effort to simplify the system and obtain a linear representation the tires are assumed to generate lateral force linearly proportional to their slip angles. This assumption leads to the following relationships.

$$F_{front} = C_f \alpha_f \qquad (20)$$
$$F_{rear} = C_r \alpha_r \qquad (21)$$

Referring to Figure 23, geometry of the tire system gives

$$tan(\delta - \alpha) = \frac{v_A}{u_A}$$

Relative velocity gives

$$v_A = v + a\phi$$
$$v_B = v - b\phi$$

No track implies

$$u_A \sim u$$
$$u_b \sim u$$

Therefore

$$tan(\delta - \alpha_f) = v + a\phi$$
$$tan\,\alpha_r = v - b\phi$$

Assuming small angles implies $tan(\delta - \alpha) \sim \delta - \alpha$

Therefore

$$\alpha_f = \delta - (v + a\phi) \qquad (22)$$

$$\alpha_r = v - b\phi \qquad (23)$$

Substituting Equations 20 – 23 into Equations 18 and 19 gives;

Lateral Velocity:

$$\dot{v} = -\frac{C_f + C_r}{mu}v - \left[\frac{aC_f - bC_r}{mu} + u\right]\phi + \frac{C_f}{m}\delta \qquad (24)$$

Yaw Rate:

$$\dot{\phi} = -\frac{aC_f - bC_r}{I_{zz}u}v - \frac{a^2C_f + b^2C_r}{I_{zz}u}\phi + \frac{aC_f\delta}{I_{zz}} \qquad (25)$$

It is also desired to plot the vehicle trajectory as a function of time. Therefore the vehicle trajectory is defined as follows.

Transforming the body fixed coordinate system to the absolute global system results in;

$$\dot{x} = u\cos\theta + v\sin\theta \qquad\qquad (26)$$
$$\dot{y} = u\sin\theta - v\cos\theta \qquad\qquad (27)$$
$$\dot{\theta} = \text{-}\phi \qquad\qquad\qquad\qquad (28)$$

Therefore the state space representation of the bicycle model is;

Linear Bicycle Model:

$$\dot{X} = AX + BU \qquad\qquad (29)$$

Where,

$$X = \begin{Bmatrix} v \\ \phi \end{Bmatrix}$$

$$A = \begin{bmatrix} -\dfrac{C_f + C_r}{mu} & -u - \dfrac{aC_f - bC_r}{mu} \\ -\dfrac{aC_f - bC_r}{I_{zz}u} & -\dfrac{a^2C_f + b^2C_r}{I_{zz}u} \end{bmatrix}$$

$$B = \begin{bmatrix} \dfrac{C_f}{m} \\ \dfrac{aC_f}{I_{zz}} \end{bmatrix}$$

$$U = \begin{Bmatrix} \delta \\ 0 \end{Bmatrix}$$

Vehicle Trajectory:

$$\dot{x} = u\cos\theta + v\sin\theta \qquad\qquad (30)$$
$$\dot{y} = u\sin\theta - v\cos\theta$$

$x = longitudinal\ position\ coordinate$
$y = lateral\ position\ coordinate$
$u = longitudinal\ velocity$
$v = lateral\ velocity$
$\phi = yaw\ rate$
$m = vehicle\ mass$

Chapter 3 : Vehicle Modeling | Andrew Liburdi

$$I_{zz} = polar\ moment\ of\ inertia$$
$$C_f, C_r = front\ and\ rear\ axle\ cornering\ stiffness$$
$$a = distance\ between\ front\ axle\ and\ CG$$
$$b = distance\ between\ rear\ axle\ and\ CG$$
$$l = wheelbase$$
$$\delta = front\ wheel\ steering\ angle$$

3.3.3 Steady State Analysis

Now that the bicycle model has been developed key observations can be made by analyzing the response of the vehicle while negotiating a steady state corner. It is assumed that the vehicle is performing a turn with a constant forward velocity and steer angle. In this analysis it is desired to investigate three key response variables, yaw rate, body slip angle and the radius of curvature. Relationships between these response variables and the system input (steer angle) are known as transfer functions which are listed below.

> ➢ ϕ/δ = Yaw rate transfer function
>
> ➢ β/δ = Body Slip angle transfer function
>
> ➢ R/R_O = turning radius transfer function

Kinematic Steering

Recall that in order for a tire to generate the lateral loads needed to travel along a curved path, they need to develop slip angles. Due to the generation of slip angles the vehicle will follow a path different than which it is pointed, resulting in a body slip angle β as illustrated in Figure 23. However, for low speed cornering where the lateral acceleration is low, the slip angles can be considered negligible. This results in the vehicle path being dictated by the vehicle's geometry and the steer angle δ. This is illustrated in Figure 24.
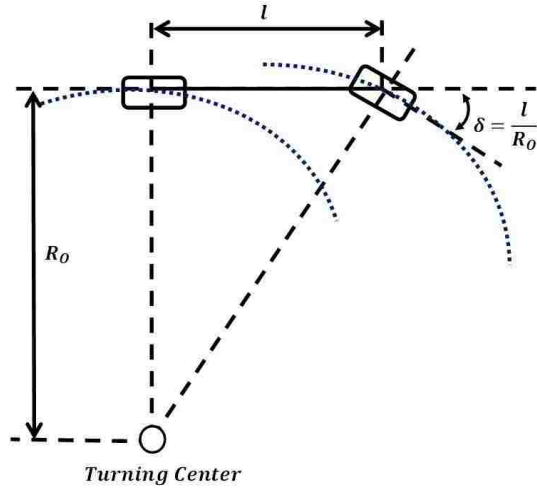
Figure 24: Kinematic steering

For low lateral accelerations, slip angles are negligible and the turning radius is defined by the wheel base of the vehicle and the steer angle of the front tire. This kinematic steering is the basis for all steady state behaviour and defines the response of a neutral steer vehicle.

By trigonometry the radius of curvature for the vehicle's path can be shown to be;

Kinematic Steering
Radius:

$$R_O = \frac{l}{\delta} = \frac{a + b}{\delta} \tag{31}$$

A key feature of kinematic steering is that due to the lack of lateral acceleration and subsequently rear slip angle, the rear wheels travel along a shorter radius than the front wheels. This corresponds to having a body slip angle that is positive as defined by the sign conventions in Figure 23.   As the vehicle increases its lateral acceleration, the rear slip angle increases until β becomes negative and the rear wheels travel along a larger radius than the front. It will be shown later that kinematic steering defines the behaviour of a neutral steering vehicle and is considered the baseline for all types of handling.

Transfer Functions

Setting the derivative terms of Equation 29 to zero and using algebra, the following transfer function expressions can be obtained. For a detailed development of these equations refer to the appendices.

Yaw Rate Transfer
Function:

$$\frac{\phi}{\delta} = \frac{u}{a + b - \dfrac{mu^2(aC_f - bC_r)}{(a + b)C_f C_r}} \tag{32}$$

Recall that $\beta = v / u$ therefore,

Body Slip Angle
Transfer Function:

$$\frac{\beta}{\delta} = \frac{b - \dfrac{amu^2}{(a + b)C_r}}{a + b - \dfrac{mu^2(aC_f - bC_r)}{(a + b)C_f C_r}} \tag{33}$$

Recall that $R = u/\phi$ and $R_O = l/\delta = (a + b)/\delta$ therefore,

Radius of Curvature
Transfer Function:

$$\frac{R}{R_O} = 1 - \frac{mu^2(aC_f - bC_r)}{(a + b)^2 C_f C_r} \tag{34}$$

One term that is critical in defining the behaviour of the above transfer functions is called the static stability factor, which is defined below. It can be seen that the static stability factor is present in all three transfer functions and dictates the form of their solutions.

Static Stability
Factor:

$$aC_f - bC_r \tag{35}$$

Looking first at the turn radius transfer function it becomes clear that there are three cases that can occur depending on the sign of the static stability factor.

Case 1:

$$aC_f - bC_r = 0 \quad \xrightarrow{yields} \quad \frac{R}{R_O} = 1$$

The turn radius of the vehicle is the same as the kinematic radius and is independent of the vehicle's velocity. This is known as the neutral steer condition and is the baseline for all handling behaviour.

Case 2:

$$aC_f - bC_r < 0 \xrightarrow{yields} \frac{R}{R_O} > 1$$

The vehicle will travel along a turn radius that is larger than the kinematic radius and is said to be understeering. What this means is for a given velocity, an understeering vehicle will require a larger steering angle to maintain the same turning radius as a neutral steering vehicle.

Case 3:

$$aC_f - bC_r > 0 \xrightarrow{yields} \frac{R}{R_O} < 1$$

The vehicle will travel along a turn radius that is smaller than the kinematic radius and is said to be oversteering. For a given velocity, an oversteering vehicle will require less steering angle to maintain the same turning radius as a neutral steering vehicle.

To better understand the significance of the static stability factor and the three cases highlighted above, the transfer functions of Equations 32- 34 were plotted over a range of velocities and are presented in Figure 25 - Figure 27. The transfer functions for the E-Maxx configuration were also plotted in order to compare its response.
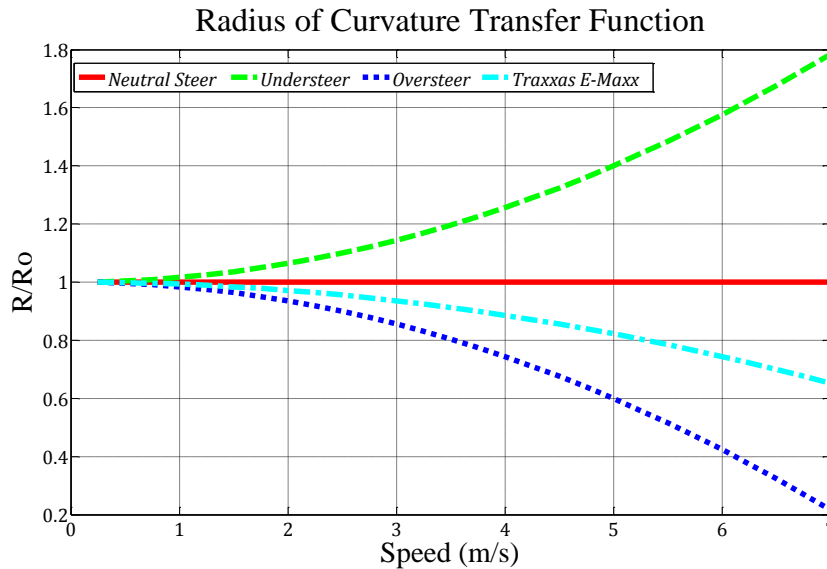
Figure 25: Radius of curvature steady state transfer function

The above figure illustrates the dependence of the radius of curvature transfer function on the sign of the static stability factor. As can be seen understeer vehicles require a larger turn radius for a given steer input and speed while oversteer vehicles require less. Note that by definition of a neutral steer vehicle's turn radius is the kinematic radius which is indicated above by a constant transfer function value of one. It is also observed that the E-Maxx can be considered an oversteering vehicle since its transfer function decreases with velocity.
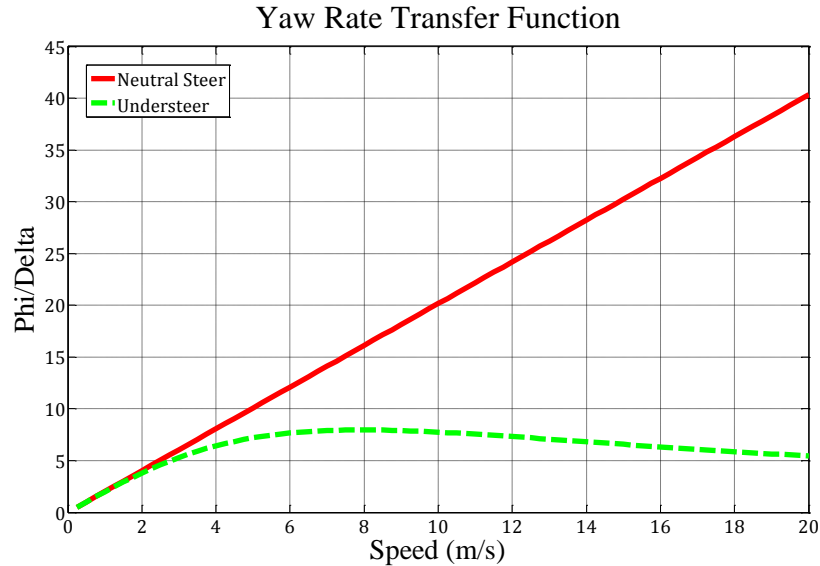
Figure 26: Yaw rate steady state transfer function

From the yaw rate transfer function the stability characteristics of the different cases can be observed. For understeer vehicles the yaw rate response eventually plateaus at a maximum value which can be considered a stable condition. Oversteering vehicles have their yaw rate response increases asymptotically with respect to vehicle speed, which ultimately results in a loss of control.
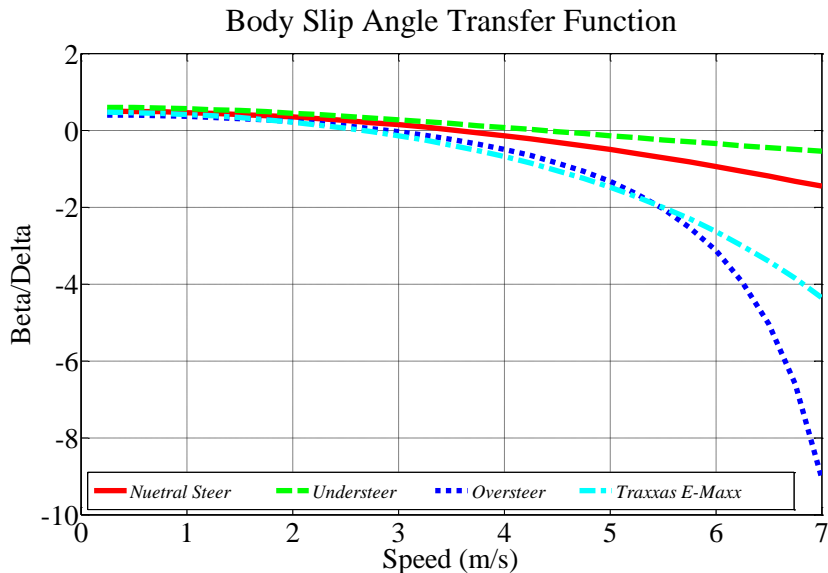
Figure 27: Body slip angle steady state transfer function

For low velocities the body slip angle transfer function is a positive value, which represents a vehicle whose rear wheels track inside the front. As the vehicle velocity is increased the body slip angle becomes negative, resulting in the rear wheels tracking outside the front. The speed at which this transition occurs is known as the tangent velocity because at this point the vehicle path and heading angle are tangent to each other. Similar to the yaw rate transfer function, the body slip angle becomes increasingly unstable with increases to vehicle velocity for oversteering vehicles.

From the above plots it is seen that as the vehicle velocity increases the transfer function responses become drastically different depending on the sign of the static stability factor. For example, for an oversteering vehicle, the yaw rate and slip angle transfer functions grow exponentially as the velocity increases. For the understeering, vehicle the turn radius grows at an increasing rate, as the velocity increases.

Another important observation can be made from the body slip angle plot. Notice that it starts off as a positive quantity and eventually becomes negative. Recall, that for low speed turning the rear slip angles are small and therefore the rear wheels will track inside the front wheels. The point when the rear slip angles are great enough so that the vehicle rear wheels track outside of the front is shown in Figure 27 when $\beta = 0$. The exact velocity that this occurs can be found by equating Equation 33 to zero and solving for u. This velocity is known as the tangent velocity because at this point the vehicle's path and heading are tangent to one another. Finally, looking at the transfer functions for the E-Maxx it is observed that it can be classified as an oversteering vehicle.

Tangent Velocity:

$$u_{Tan} = \sqrt{\frac{b(a+b)C_r}{ma}}$$

(36)

Understeer/Oversteer in Detail

In order to better visualize what is happening when a vehicle is understeering, it is necessary to examine how the lateral forces are being developed at each axle. In a steady state corner for a certain lateral acceleration, the lateral forces at each axle required to balance the vehicle can be found by performing a moment balance.

Therefore,

$$F_{front} = \frac{a}{b} F_{rear}$$

(37)

Note that for steady state cornering the forces defined by Equation 37 directly balance each other and no yaw moment is generated (i.e., yaw rate is constant). However, if the rear axle force were to increase faster than the front axle, then the above relationship will no longer exist and a yaw moment will be created that tries to turn the vehicle away from its intended path. The generation of this counter yaw moment is known as understeer. Since the axle forces are generated by producing slip angles, then an understeering vehicle is one that has its rear slip angles increase faster than its front slip angles as lateral acceleration builds. Conversely, an

oversteering vehicle is one that has its front slip angles increase faster than its rear slip angles as lateral acceleration builds. Therefore another way of expressing the understeer/oversteer behaviour of a vehicle is,

$$\textit{Understeer} \qquad \frac{\Delta(\alpha_F - \alpha_R)}{\Delta A_{Lateral}} < 0 \qquad\qquad (38)$$

$$\textit{Oversteer} \qquad \frac{\Delta(\alpha_F - \alpha_R)}{\Delta A_{Lateral}} > 0 \qquad\qquad (39)$$

It was shown in Figure 26 and Figure 27 that for an oversteering vehicle an increase in the vehicle's velocity resulted in an exponential increase in its yaw rate and body slip angle transfer functions. Plotting those two transfer functions over a wider velocity range reveals the stability implications of an oversteering vehicle.
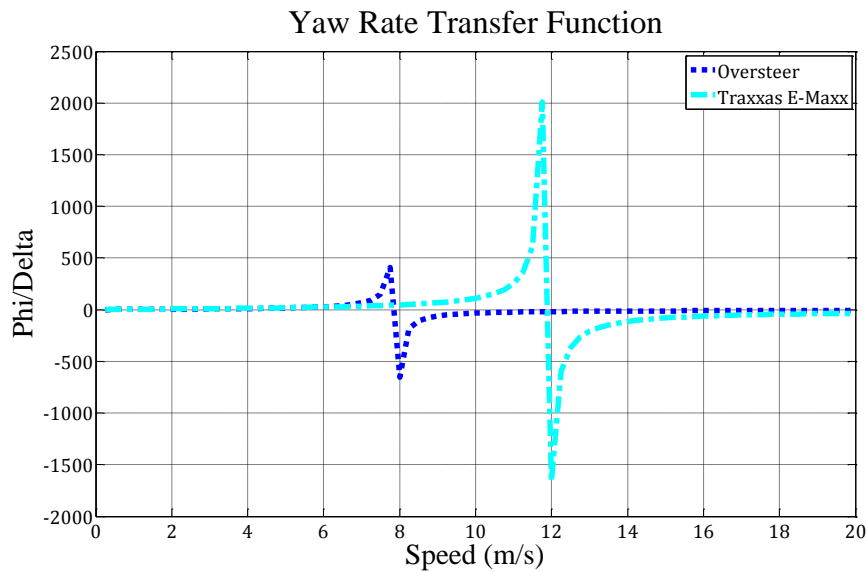
Figure 28: Oversteer instability – Critical speed

Oversteer response is shown to increase asymptotically around a particular value known as the critical speed. This sudden increase in yaw rate results in a loss of control and illustrates the instability associated with oversteering vehicles.

Figure 28 shows that for an oversteering vehicle, the yaw rate increases asymptotically about a particular velocity. The velocity about which the oversteering vehicle's response becomes infinite is known as its critical speed. Observing the transfer function response, it becomes clear that the oversteering condition is unstable because around the critical speed, a slight increase in the vehicle velocity results in a large increase in yaw rate.

The source of the instability has to do with the fact that an oversteering vehicle generates a yaw moment that tries to reduce its turn radius as lateral acceleration is generated. The reduction in the turn radius increases the lateral acceleration further and a perpetuating cycle ensues that ultimately results in a loss of control. Note that the yaw rate of an actual vehicle will never increase to infinity as predicted by this linear analysis because the tire forces will eventually saturate, resulting in the vehicle spinning out or sliding across the road surface. The critical speed can be found by finding the limit of the yaw rate transfer function as velocity goes to infinity. This results in the following expression.

Critical Speed:

$$V_{Critical} = \sqrt{\frac{C_f C_r (a+b)^2}{m(aC_f - bC_r)}}$$

(40)

The E-Maxx was shown to be an oversteering vehicle and therefore has the following critical speed.

Traxxas E-Maxx
Critical Speed:

$$V_{crit} = 11.91 \ m/s$$

(41)

Looking at Figure 28 it is seen that the test speed of 9 m/s is below the critical speed and is low enough to avoid any major instability. This is important because it would be very difficult to perform testing and achieve repeatable results while operating at or near the critical speed. The instability around that region would cause the vehicle to be unpredictable since small variations in the road surface would cause large deviations in the vehicles behaviour.

Observing the transfer function for the understeer vehicle in Figure 29, it is seen that no such instability exists, but rather the transfer function increases to a maximum value and then slowly fall off as the vehicle speed is increased further. The speed at which the transfer function is a maximum is called the characteristic speed and can be obtained by performing the limit analysis with the resulting expression shown below.

Characteristic
Velocity:

$$V_{Char} = \sqrt{\frac{C_f C_r (a+b)^2}{m(bC_r - aC_f)}}$$

(42)

Chapter 3 : Vehicle Modeling | Andrew Liburdi
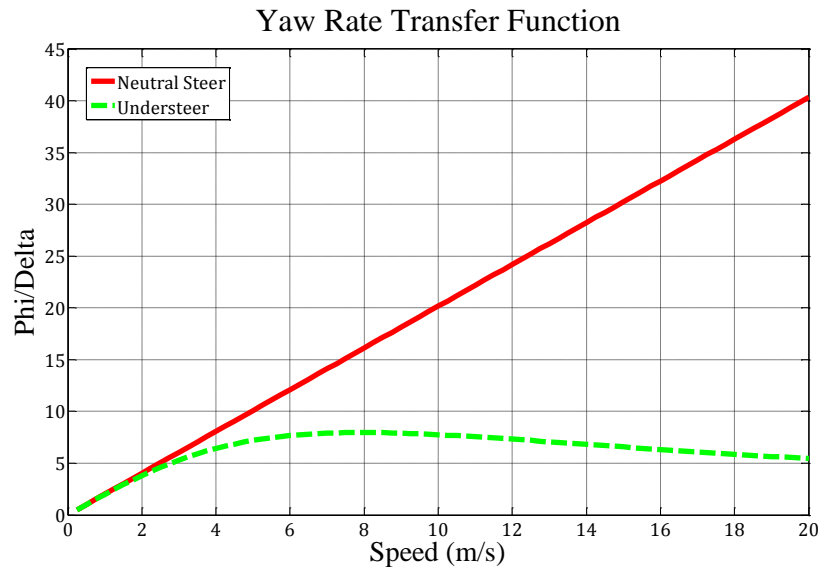
Figure 29: Understeer stability – Characteristic speed

Understeer vehicles avoid the instability, with their transfer functions reaching a maximum at the characteristic speed. Note that neutral steer cornering is dictated by kinematic steering which is independent of speed. Therefore its yaw rate transfer function increases linearly with respect to speed.

At the characteristic velocity the understeering vehicle transfer function is a maximum. What this represents is that for an understeering vehicle, its yaw response to steering inputs is most sensitive at the characteristic speed. The understeering vehicle is considered stable because it generates a yaw moment that tries to turn the vehicle out of the corner, thus avoiding a runaway condition altogether. Figure 29 also illustrates that for a neutral steer vehicle the transfer function is linear with respect to vehicle velocity. This is to be expected since by definition a neutral steer vehicle's steer input is independent of vehicle speed (i.e. kinematic steering).

3.3.4 Transient Analysis

Now that the steady state performance of the E-Maxx has been defined, it is necessary to look at how it responds to time varying steer inputs. Dynamic systems react to control inputs much like filters in that their response is dependent on the frequency of the forcing function driving the system. Therefore, when analyzing a vehicle's transient response it is often more useful to view the results within the frequency domain rather than the raw time histories themselves. Frequency methods allow investigators to examine the stability characteristics of the system which can prove to be very valuable at identifying its fundamental dynamic modes. The following sections will examine the E-Maxx's stability characteristics as predicted by the linear

bicycle model. The vehicle's frequency response will also be constructed and key observations made about various vehicle properties.

Stability:

One of the main advantages of using linear models to characterize a system is that frequency methods can be applied to investigate the systems stability. This is done by artificially applying a small input to the system and observing how it reacts when the input is taken away. The vehicle's free response illustrates how it will naturally dissipate energy and the frequency at which it oscillates is known as the natural frequency. This is performed using the following analysis.

Assume that the system free response can be represented by;

Free Response:
$$\bar{X}e^{\lambda t} \tag{43}$$

Substituting into the bicycle model of Equation 29 gives;

$$M\dot{x} + Cx = 0$$
$$M\overline{\lambda X}e^{\lambda t} + C\bar{X}e^{\lambda t} = 0$$
$$[M\lambda + C]\bar{X}e^{\lambda t} = 0$$
$$[M\lambda + C]\bar{X} = 0$$

Where,
$$M = \begin{bmatrix} m & 0 \\ 0 & I_{zz} \end{bmatrix}$$

$$C = \begin{bmatrix} \dfrac{C_f + C_r}{u} & mu + \dfrac{aC_f - bC_r}{u} \\ \dfrac{aC_f - bC_r}{u} & \dfrac{a^2C_f + b^2C_r}{u} \end{bmatrix}$$

It should be noted that this is the form of the standard eigenvalue problem. Therefore, in order to satisfy this equation then the following relationship must be met.

Characteristic
Equation:
$$det[M\lambda + C] = 0 \tag{44}$$

Expanding the terms and solving for the eigenvalues results in the following.

Let
$$A = mI_{zz}u^2$$
$$B = mu(a^2C_f + b^2C_r) + I_z uC_f C_r$$

$$C = (a + b)^2 C_f C_r - mu^2 \left(a C_f - b C_r \right)$$
$$A\lambda^2 + B\lambda + C = 0$$

To solve for λ, the quadratic equation is used.

Eigenvalues:

$$\lambda_{1,2} = \frac{-B \pm \sqrt{B^2 - 4AC}}{2A} \qquad (45)$$

At this point we can investigate the stability of the system. Recall that the free response was assumed to be of the exponential form shown in Equation 43. Therefore, in order for the system to be stable, the eigenvalues must be negative. As a result the following condition must be met.

$$-B + \sqrt{B^2 - 4AC} < 0$$
$$4AC > 0$$

Note that A is always positive therefore;

$$C = (a + b)^2 C_f C_r - mu^2 \left(a C_f - b C_r \right) > 0$$

It follows that if $\left(a C_f - b C_r \right) < 0$ than stability is guaranteed. Recall that $\left(a C_f - b C_r \right)$ is called the static stability factor and a negative value represents the understeer condition. Therefore, an understeering vehicle is always stable.

Looking at the expressions for the eigenvalues it is clear that they are dependent on vehicle velocity. This dependence is illustrated in Figure 30 and Figure 31 where the eigenvalues are plotted with respect to vehicle speed.

Chapter 3 : Vehicle Modeling | Andrew Liburdi

Eigenvalues: Understeer
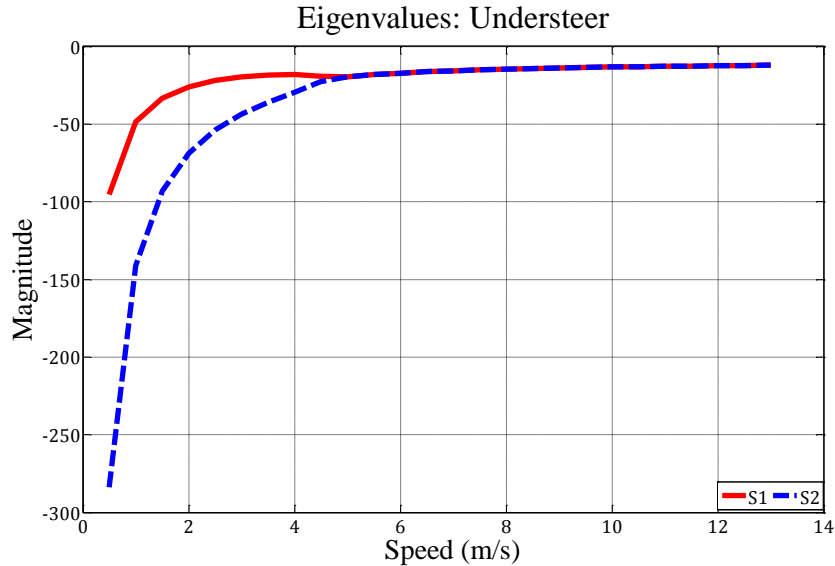
Figure 30: Eigenvalue analysis - Understeer vehicle

The understeer vehicle exhibits two negative real valued eigenvalues which combine into complex conjugates at approximately 4.5 m/s. The complex conjugate eigenvalues result in oscillatory motion with the negative real parts indicating a decaying response, which is considered stable.

Eigenvalues: Oversteer
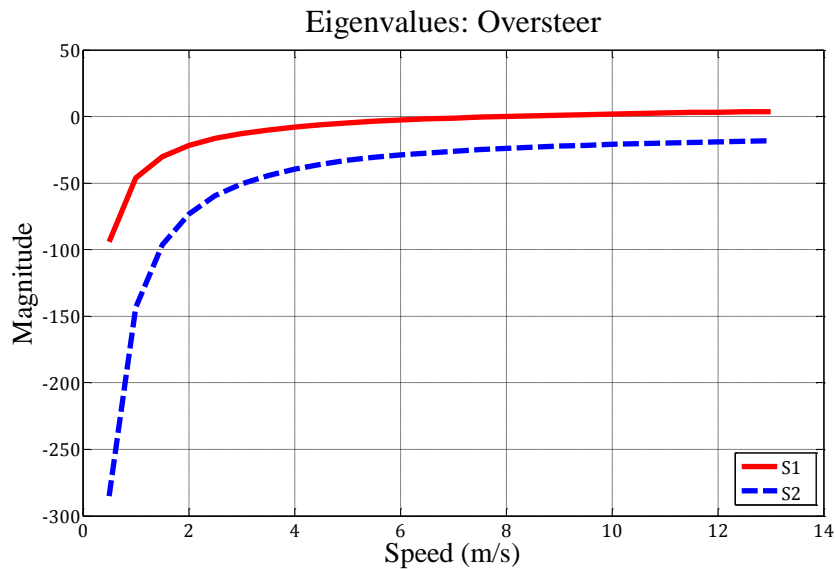
Figure 31: Eigenvalue analysis – Traxxas E-Maxx

The E-Maxx, representing the oversteer condition, has two real valued eigenvalues with one becoming positive as vehicle velocity is increased. The positive eigenvalue results in an unstable condition based on the assumed exponential response.

For the understeer vehicle it is seen that the eigenvalues begin as two negative real numbers and decrease with vehicle velocity until they merge into a single value. Looking at the expression for the eigenvalues, it is seen that as the speed increases the term under the root will

become negative and result in eigenvalues which are complex conjugates. Based on the assumed form of the response, complex eigenvalues result in an oscillatory response. The negative real portion of the eigenvalue ensures that the amplitude decays and thus the response is considered stable.

It is seen that the E-Maxx eigenvalues remain real with one eigenvalue becoming positive as vehicle velocity increases. Oversteering vehicles do not possess complex eigenvalues and therefore will not exhibit oscillatory motion. The positive eigenvalue results in the unstable response that was observed during the steady state analysis.

Frequency Response:

It is now time to investigate how the system reacts to time varying steer inputs. The primary tool to investigate this behaviour is known as the frequency response function (FRF). The most straight forward method to construct the FRF is shown below.

Let us apply a sinusoidal steer input of the form;

Forcing Function:
$$\delta = \delta e^{\lambda t} \tag{46}$$

Assuming the response is of the same form as the input;

$$X = \bar{X} e^{\lambda t}$$

Substituting into the bicycle model gives;

$$M\lambda \bar{X} e^{\lambda t} + C\bar{X} e^{\lambda t} = F\delta e^{\lambda t}$$

Frequency Response Function:
$$\frac{\bar{X}}{\delta} = [M\lambda + C]^{-1}[F] \tag{47}$$

Where,
$$\lambda = \omega_{steer} i \tag{48}$$

$$\omega_{steer} = frequency\ of\ steer\ input\ \ \frac{rad}{s}$$

Note that the imaginary form of the steer input ensures that the forcing function is a pure sinusoidal wave form, allowing us to investigate the system response over a range of frequencies.

Chapter 3 : Vehicle Modeling | Andrew Liburdi

Using Equation 47 the frequency response can be plotted for both state variables v and ϕ. Note that only the yaw rate and lateral velocity transfer functions are examined here; however, the radius of curvature and body slip angles can be constructed using simple algebra. In fact, the transfer functions derived within the steady state analysis are special cases of the FRF's when the input frequency is assumed to be zero. The FRF's for both the understeering and E-Maxx vehicles are plotted over various vehicle speeds in the figures that follow.
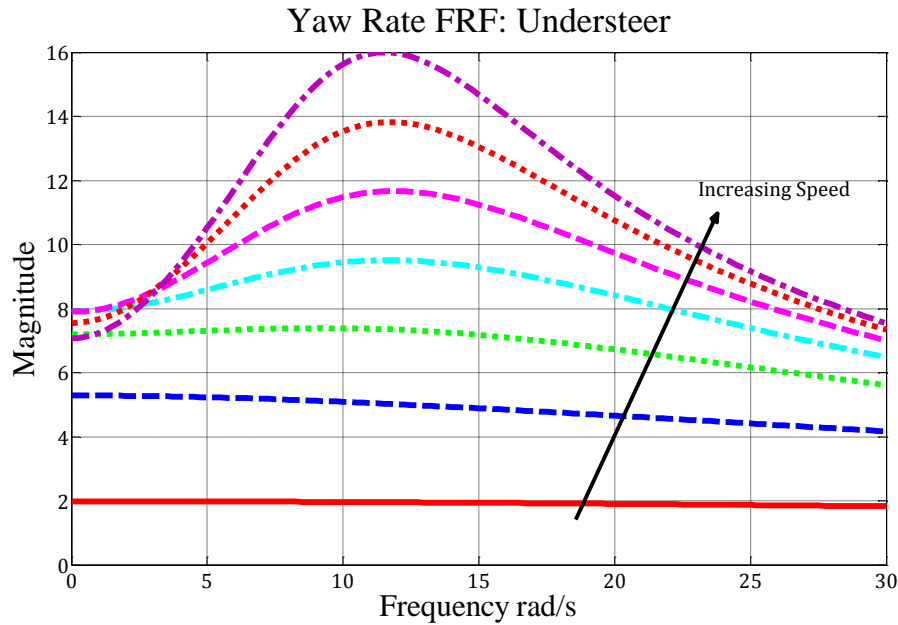
Figure 32: Yaw rate FRF of an understeer vehicle

FRF is shown to increase to a peak at its natural frequency before decreasing with further increases to input frequency. It is also seen that the magnitude of the FRF increases with vehicle velocity which corresponds to decreases in system damping. Therefore the vehicle velocity acts to decrease the yaw damping of the system resulting in an under damped situation where oscillatory motion persists.
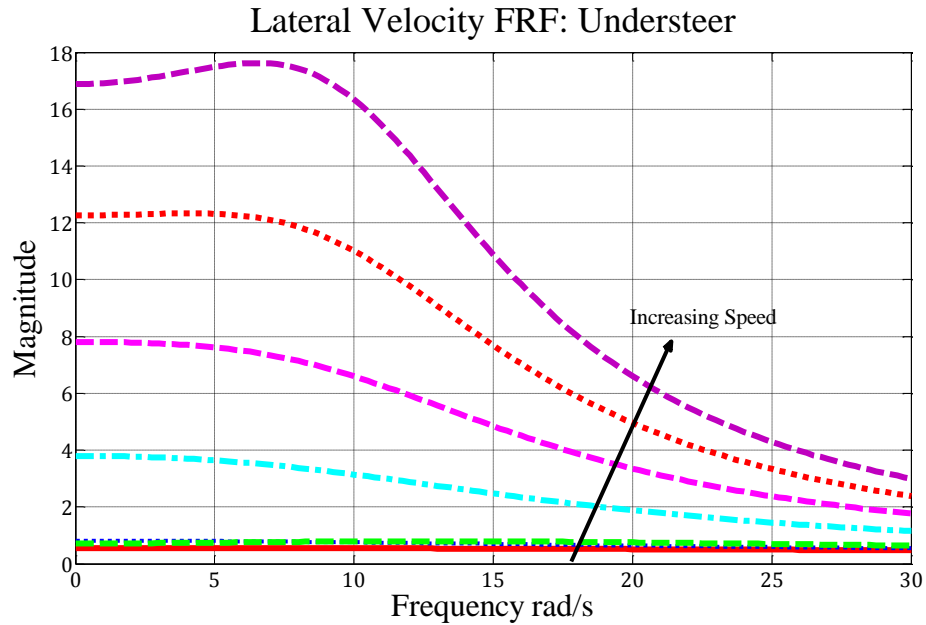
Figure 33: Lateral velocity FRF for understeer vehicle

Similar to yaw rate FRF, the lateral velocity increases to a peak but at a much lower natural frequency of approximately 8 rad/s. It is seen that past its natural frequency, the lateral velocity is attenuated, with magnitudes roughly half of their initial values.

As can be seen from Figure 32 and Figure 33, for an understeering vehicle the magnitudes of the FRF's both increase to a maximum value centred about their natural frequencies. Also, the peak magnitude of both FRF's are shown to be greater for higher vehicle velocities. Comparing this behaviour to that of a standard spring-mass-damper system it is seen that the increase in magnitude is due to a decrease in yaw damping as the vehicle velocity is increased. Therefore, as the velocity is increased the yaw damping is reduced until the system becomes under damped and oscillatory motion is allowed to persist, explaining the presence of complex conjugate eigenvalues.
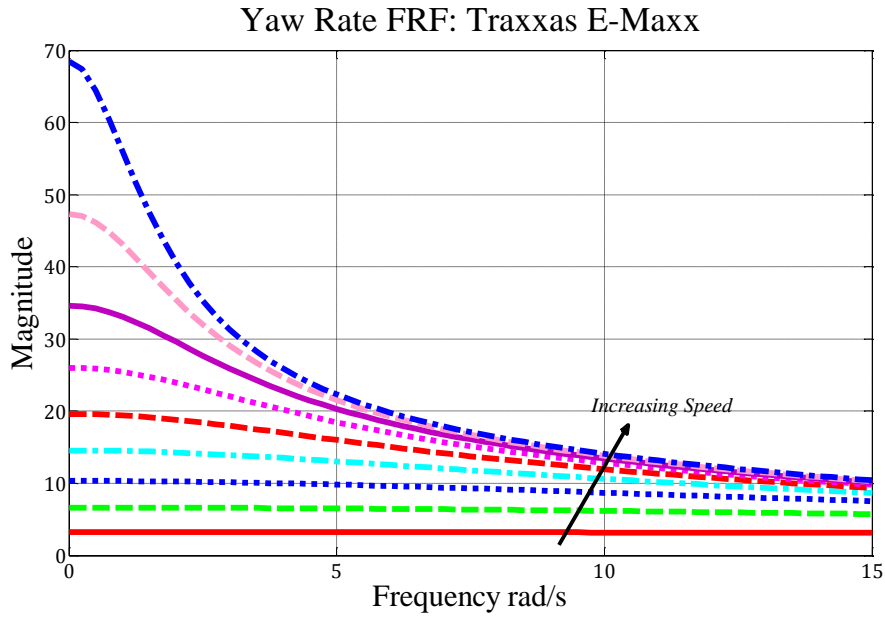
Figure 34: Yaw Rate FRF for the Traxxas E-Maxx

The maximum magnitude is found to be at zero hertz (DC) which indicates that there are no natural frequencies associated with the E-Maxx vehicle. As expected, the decrease in yaw damping with vehicle velocity also results in larger magnitudes in the FRF.
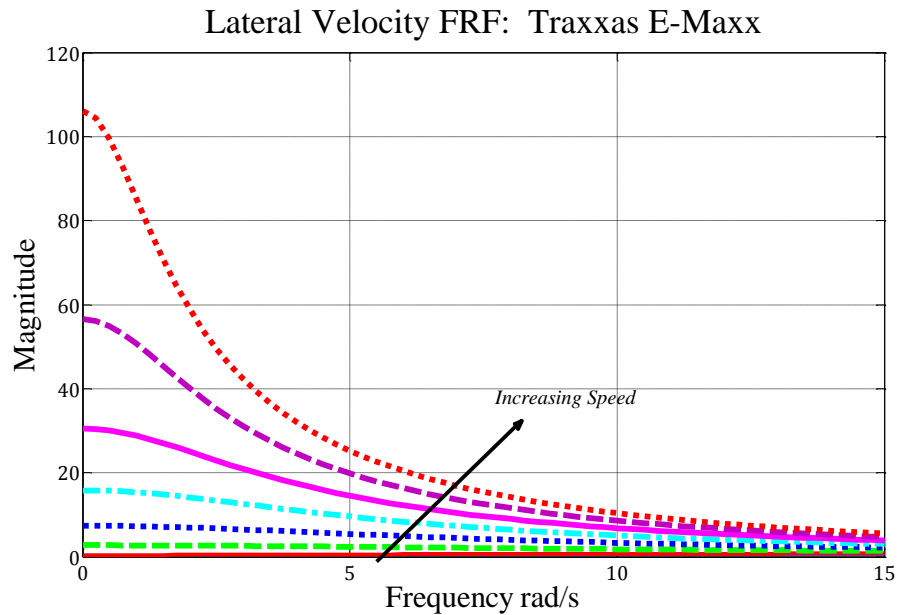
Figure 35: Lateral Velocity FRF for the Traxxas E-Maxx

Similar to the yaw rate FRF, no natural frequency is observed within the frequency range of interest. Amplitudes increase with vehicle velocity due to a reduction of system damping with vehicle velocity.

The E-Maxx's FRF is a maximum at zero Hertz and then decreases as frequency is increased. This is consistent with the eigenvalue analysis shown previously, which indicated that the E-Maxx did not have any complex values or oscillatory motion. Therefore, it should not be expected that the E-Maxx have a natural frequency or exhibit any peaks within the frequency range of interest for either yaw rate or lateral velocity.

Chapter 4: Scale Vehicle Test Bed

4.1 Control System

4.1.1 Handy Cricket Development Board

One of the main goals of this research was to develop a test setup that was untethered from the acquisition and control system. In order to accomplish this goal it was necessary to implement a control system that could be fully contained within the vehicle and was flexible enough to interface with the custom acquisition module. In an effort to reduce the amount of development time required to setup the test bed, the Handy Cricket development board was utilized.

The Cricket itself is an evolution of the MetaCricket project; a hardware and software construction kit for building computational devices. The heart of MetaCricket system is the Handy Cricket, a tiny, programmable development board that can directly control motors, servos and receive information from sensors. The Cricket evolved from an early MIT "Programmable Brick" design, which led to the popular LEGO Mindstorm Robotics Invention System [*39*]. The Cricket allows designers of all backgrounds, not just engineers, to create working prototypes of their ideas. The system is also highly extensible, allowing designers to create custom breakout modules that interface with the Cricket system via a proprietary communications bus. The following sections will outline the Handy Cricket and document several of the key features of the system that were leveraged in the development of the test bed. For details regarding the Cricket proprietary bus protocol refer to the appendices or the Cricket documentation.

Architecture:

The Handy Cricket is comprised of several discrete electronic components which are integrated in order to implement its various functions. The hardware that makes up the Cricket is highlighted below [*40*].

> ➢ **PIC Microcontroller:** The Handy Cricket is based around the PIC16C715, which includes 2048 bytes of one-time programmable ROM (Contains the Handy Cricket operating system), analog inputs, and digital I/O.

- ➢ **Serial EEPROM:** Compiled user code is loaded into a 24LC32 memory chip, which provides 4096 bytes of non-volatile storage.
- ➢ **IrDA Communication Chip:** Using the Sharp GP2W0001YP chip, the Handy Cricket implements bi-directional infrared communications for program download and inter-Cricket communications.
- ➢ **Dual motor driver chip.** The Texas Instruments SN754410NE dual H-bridge motor driver allows the Handy Cricket to directly power two DC motors.
- ➢ **Assorted I/O components.** The Handy Cricket includes two analog sensor ports, two bus expansion boards, a piezo beeper, a run status LED, and a run/stop pushbutton.

Crickets come with a custom software environment, known as Cricket Logo. Cricket Logo is a procedural language that includes global and local variables, procedure arguments (functions), logic structures (loops, if/ifelse), and specialized primitive functions for interacting with motor and sensor hardware [*40*]. The Cricket virtual machine is burned into the PIC microprocessor's internal ROM (read-only memory) and is implemented in assembler language. The virtual machine uses the microprocessor's internal RAM (random-access memory) for a program stack. The user's code resides in a serial EEPROM (electrically erasable programmable read only memory) that is permanently connected to the microprocessor. Built-in infrared communication routines include a protocol for reading and writing to this external EEPROM, such as when downloading Logo programs from the PC. The Logo environment is illustrated in Figure 36.
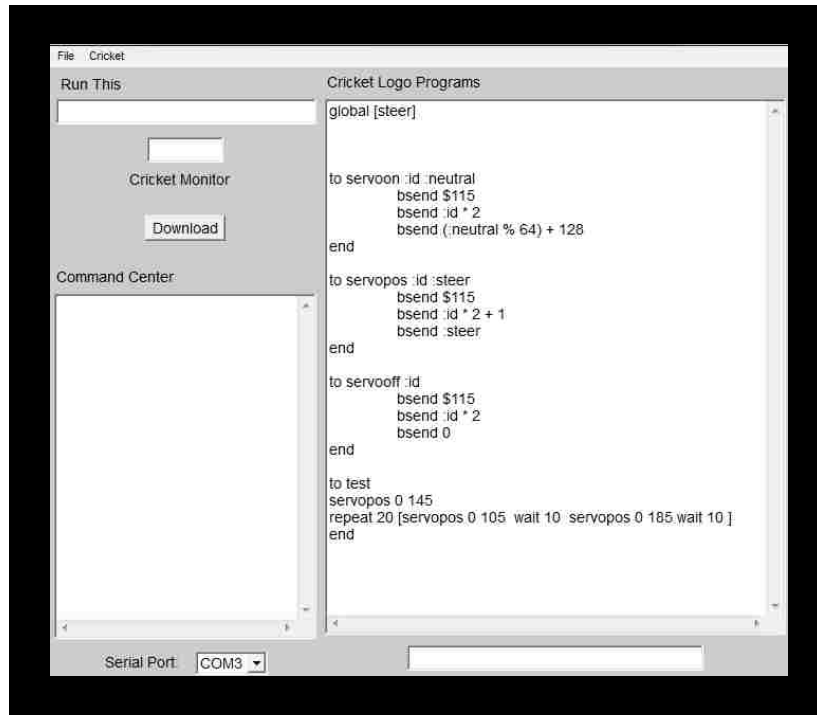
Figure 36: Cricket Logo interface

Custom development environment used to program the Handy Cricket. There are three sections
associated with the interface. The window on the right is where code is written to be eventually
executed on the Cricket. The command center window on the left is where commands or functions can
be written that will be instantly executed by the Cricket. The "*Run This*" field at the top left is where a
specific function can be stored such that when the push button the Cricket is depressed, the function
stored in this field is executed.

Application:

Within this research the Cricket is used as a general purpose processor with its main
function being to act as the user interface for the PIC based acquisition module. The flexibility of
the Cricket bus allowed the acquisition module to be easily interfaced with the Cricket, allowing
the user to issue commands to the module as well as receive data. With the Cricket, acquisitions
are started by pressing the push button on the device itself. It will then signal the acquisition
module to start collecting data before issuing a stop command. The Cricket is also able to
automatically create data sets that increment with each test run so that all data is organized and
easily edited.

Other scenarios may exist beyond those used within this research. For example, the
Cricket is highly extensible and therefore multiple modules can be connected to the device. It is
possible to connect multiple acquisition modules in case the channel count of a single module

was not sufficient. The Cricket is also able to control servo motors directly through its dedicated servo ports or through a breakout board that offers up to an additional nine channels.

4.1.2 Wireless Control

In order to issue control inputs to the vehicle and still have an untethered test bed, the E-Maxx's RC communication system was used. The E-Maxx comes with a proprietary RC control system that consists of a hand held transmitter and a vehicle mounted receiver that operates at 27 MHz. The system is able to deliver commands at distances of up to 100 m depending on the amount of radio interference present. To ensure that the vehicle commands were repeatable it was important to be able to interface the transmitter with a computer so that precise control of the vehicle could be achieved via software. The RC control system can be seen in Figure 37.
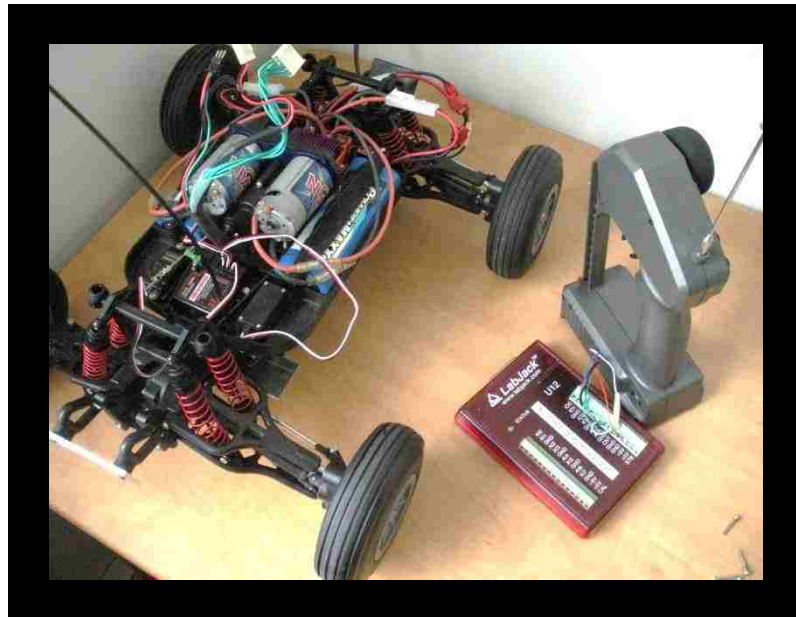
Figure 37: RC control system

RC transmitter is interfaced with LabJack data logger in order to implement computer control. The throttle and steering potentiometers are by-passed on the transmitter and wired to two analog outputs on the LabJack. MatLab is used to communicate directly with the LabJack and issue all steering and throttle commands to the vehicle.

To interface the transmitter with the computer a low cost data logger was used called the LabJack. The key feature of the LabJack used to interface with the transmitter was its two analog outputs that are able to send 0-5 V signals. Therefore, the transmitter was interfaced with the computer by taking the signal wires originally connected to the transmitters' steering and throttles potentiometers and connecting them to the two analog outputs on the LabJack. This is illustrated in Figure 37.

MatLab was the software suite used to generate the control commands. In order for MatLab to communicate with the LabJack, a set of driver .dll files needed to be downloaded from the manufacturer's website and saved to a directory on the PC. Before the drivers can be used, the directory that the .dll files are located in must be saved as a searchable directory within MatLab. Once this is done, it is a simple matter of calling up the LabJack specific functions from the MatLab command line. The function used to output analog voltages is highlighted below.

LabJack Analog Output
MatLab Function:

AnalogOut(ID, Demo, A0, A1)

Where;

ID = LabJack Serial ID

Demo = Value of 1 allows the function to be called without a LabJack connected

A0 = Voltage to be output to channel 0

A1 = Voltage to be output to channel 1

4.2 Acquisition Hardware

4.2.1 Sampling Theory

All acquisition systems require a continuous time varying electrical signal produced by transducers to be digitized and stored to memory. The digitization of this signal results in having to sample the signal at equally spaced time intervals defined by its sample rate. The key steps involved in sampling data are illustrated by the flow chart in Figure 38. A filter is used after the transducer in order to reject higher frequency content. This higher frequency content is not usually desired because it is primarily due to higher order dynamics that the investigator is not interested in observing. In fact, if ignored the higher frequency content can corrupt the lower frequency data due to a phenomenon known as aliasing [*41*].

Figure 38: Acquisition procedure flow chart

Above figure illustrates the general procedure used to sample a time varying transducer signal. A low pass filter is placed between the transducer and the A/D convertor in order to reject high frequency noise that could corrupt the data due to aliasing effects.

To better understand this phenomenon, Figure 39 shows a periodic time domain signal which is to be digitized. If the sample rate used to sample the data is equal to the frequency of the signal itself, then a constant value will be recorded since the signal is being sampled in the same location on the sine wave. This will effectively ignore the time varying nature of the signal and therefore doesn't allow the original waveform to be reproduced.
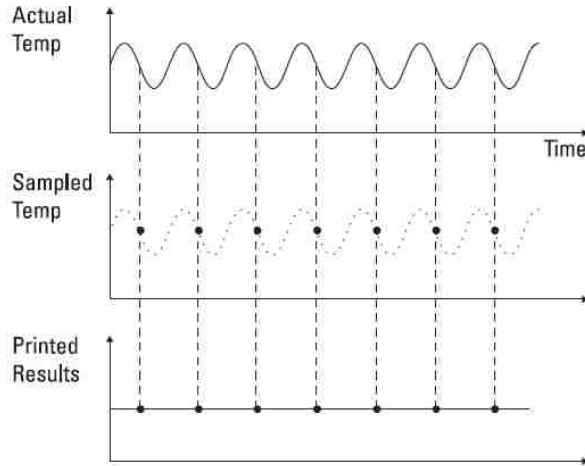
Figure 39: Aliasing example

Sampling a sine wave with a sampling rate the same as the signal itself results in a constant value being recorded. In order to properly reconstruct the time varying nature of the signal, it must be sampled at a sampling rate higher than its own frequency. Figure taken from Agilent Technologies [*41*].

It is obvious that that in order to capture the time varying nature of the signal, it must be sampled at a rate higher than its frequency. In fact, sampling theory states that in order to properly reconstruct a time varying signal the signal must be sampled at twice its own frequency. This minimum sampling frequency is known as the Nyquist frequency and is shown mathematically as;

Nyquist Frequency:
$$f_{Nyquist} = 2 \cdot f_{signal} \qquad (49)$$

This phenomenon can also be viewed within the frequency domain as shown in Figure 40. The most common method of converting time domain data over to the frequency domain is the Fast Fourier Transform (FFT). The Fourier transform operates on the concept that any periodic time varying signal can be represented by an infinite series of sine waves of varying amplitude, frequency and phase. The development of this theorem will not be presented here but the interested reader is asked to consult Nilsson [*42*] for a detailed overview of the method.

Fast Fourier

Transform:
$$y(t) = \sum A sin(\omega t + \gamma) \qquad (50)$$
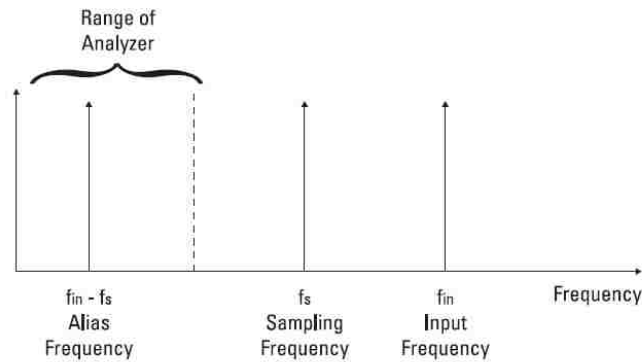
Figure 40: Aliasing viewed within the frequency domain

When a signal is sampled at a frequency less than its own frequency, an erroneous signal is produced within the frequency range of interest. The generation of this erroneous frequency data is known as aliasing, which effectively corrupts the sampled data and should be avoided by using an anti-aliasing filter. Figure taken from Agilent Technologies [*41*].

Applying the FFT to data that was sampled at a rate less than the signal frequency, results in artefacts being produced within the frequency range of interest. This aliased frequency is always generated in the process of sampling and can be represented by the following expression [*41*];

Alias Frequency:
$$f_{Alias} = f_{signal} - f_{sample} \qquad (51)$$

In Figure 40, the input frequency is slightly higher than the sampling frequency so a low frequency alias term is generated. If the input frequency equals the sampling frequency, then the alias term falls at DC (zero hertz). Figure 40 also illustrates the significance of the Nyquist frequency because in order to ensure no artefacts are present within the range of interest, the sampling rate must be at least twice the signal's frequency. Unfortunately, the real world rarely restricts the frequency range of its signals. The only way to be really certain that the input frequency range is limited is to add a low pass filter before the A/D convertor as depicted in Figure 38. This is known as an anti-aliasing filter and should be used in order to ensure aliasing artefacts are not captured within the data.

4.2.2 PIC Microcontroller

The PIC family of microcontrollers is a highly popular solution for many integrated electronics. The chips are low cost and offer a wide range of features which make them ideally suited for electronic hardware control. The family of microcontrollers consists of the PIC10, PIC12, PIC16 and PIC18 lines of 8-bit controllers, with the PIC18 line having the largest instruction set [43]. For this research, the PIC18F 4525 was chosen due to its ability to collect up to 13 analog channels and having a large memory cache of up to 4 kB. The following subsections will describe the controller's architecture and the feature set that was utilized within this research in developing the acquisition system.

Architecture:

A microcontroller is made up of multiple modules that perform specific tasks. The way in which these modules interact with each other makes up its architecture. In the case of PIC microcontrollers, they use what is known as a Harvard architecture which is illustrated in Figure 41 [43].
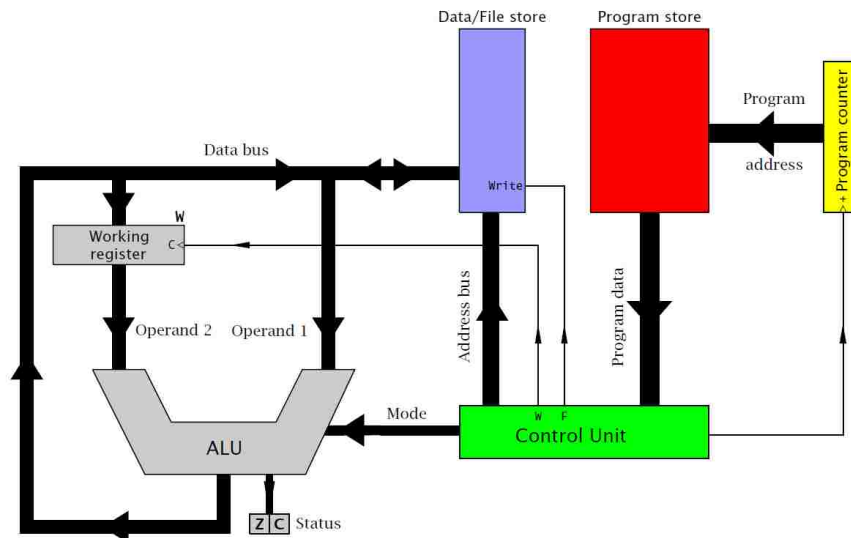
Figure 41: PIC microcontroller Harvard architecture

A PIC microcontroller is made up of six discrete components which transfer data between each other via high speed data busses. The architecture depicted above is known as Harvard architecture since the program and data memory modules are independent of each other and can be accesses simultaneously by the CPU. Figure taken from Katzen [43].

There are six main components of the microcontroller;

1. **Program Memory:** Used to store the list of instructions that the controller is to carry out. Instructions are stored as 8-bit binary numbers or bytes and correspond to basic operations called instructions that the controller is able to execute. The reader is encouraged to refer to the manufacturer's datasheet for a complete overview of its instruction set [*44*].

2. **Data/File Memory:** Used to temporarily store data used by the controller. Data can include the results obtained from arithmetic operations, or parameters to be used in calculations. Data memory is broken up into blocks called file registers where data is stored as 8-bit binary numbers. Certain registers known as special file registers (SFR's) are reserved for system specific data used to control the various functions of the controller. In total the PIC 18F 4525 has up to 4 Kb of data memory available [*44*].

3. **Control Unit (CPU):** The CPU acts as the brain of the microcontroller, processing the list of instructions stored within the program memory. The CPU is the only module that can interact with all other modules and communicates with them via high speed buses highlighted in Figure 41. The main purpose of the CPU is to interpret and execute the instruction set that the user stores in program memory. It is the CPU that coordinates the various functions of the microcontroller such as moving data between file registers and calling the ALU to perform computations.

4. **Working Register:** The working register is a specific block of data memory that the microcontroller uses to execute various operations. For example, the ALU cannot operate on a piece of data without first loading it to the working register [*44*]. Therefore, the working register is extremely important to understanding how the microcontroller functions and therefore a large portion of the instruction set deals with the manipulation of data within this register.

5. **Arithmetic Logic Unit (ALU):** The ALU has only one function which is to perform math operations on two pieces of data. In order for the ALU to carry out a calculation one operand must be stored in the working register and another in data

memory. The results of the operation can be stored either in the working register so it can be used for subsequent calculations or it can be stored directly to data memory. At the hardware level the ALU is limited to addition and subtraction only. However PIC18 devices do have instructions that implement multiplication and division through a recursive process and therefore no additional code is required to implement these operations [*44*].

6. **Program Counter:** The CPU is responsible for interpreting the list of instructions stored within program memory. In order for the CPU to keep track of its position within the list of instructions it utilizes a data file register known as the program counter (PC). The program counter is incremented after the completion of each instruction and can be considered a pointer that calls up the next instruction to be executed. The counter can be directly written to so recursive logic can be executed such as loops without the need to write the same instruction multiple times [*44*].

Timing:

The execution of program instructions is timed with the use of a clock pulse. The clock pulse is usually generated by a circuit external to the chip, such as an oscillating crystal. However, the PIC18F 4525 uses an internal RC clocking circuit which allows for programmable clock rates between 100 kHz and 8 MHz [*44*]. The higher clock rates are important to achieve the high sample rates used for the data acquisition system.

One of the key benefits of the Harvard architecture is that the program and data memory modules are separated and can be accessed independently within a single clock cycle. This better optimizes the flow of data within the microchip and allows it to perform complex instructions quickly.

Feature Set:

A key advantage of PIC microcontrollers are the wide range of features that can be found on many of the devices. The exact feature set varies between particular microcontrollers and depends primarily on the microcontroller's size (# of pins) and cost. Many of the features are implemented by using dedicated circuitry to perform key functions such as implementing standard communication protocols and sampling analog signals. Implementing these functions in hardware greatly reduces the effort required to implement these complex tasks and frees up the programmer to focus on optimizing their overall algorithm. Two key hardware implemented

functions of the PIC18F 4525 that were critical in developing the acquisition module will be highlighted below.

A/D Convertors:

In developing the data acquisition module it was essential that the process of sampling analog channels was done as accurately as possible. This was simplified by the use of the PIC18F 4525's hardware implemented analog to digital (A/D) convertor. The PIC18 F 4525 provides up to 13 A/D convertor channels with a 10-bit resolution [44]. Assuming a signal of 0-5 volts is to be sampled, a 10-bit A/D convertor allows for a voltage resolution of 0.005 V. Therefore the PIC18 F 4525 provides enough channels with which to collect data while at the same time maintaining good resolution.

The implementation of the A/D convertors was a straight forward task and consisted of the manipulation of the three file registers listed below. The steps involved are detailed within the chips datasheet [44].

> ➢ **ADCON0** – A/D Operation Register
> ➢ **ADCON1** – A/D Configuration Register
> ➢ **ADCON2** – A/D Timing Register

Serial Interface:

In developing the acquisition module, it was necessary to interface the PIC microcontroller with other devices in order to store and unload data. Fortunately, the PIC includes dedicated hardware modules that implement many popular communication protocols, eliminating the need to program the low level logic necessary to perform these tasks. There are many protocols used to interface devices; however, the two that were utilized within this research were the I^2C and Serial Communications Interface (SCI). Both protocols are serial interfaces, meaning that each bit of a data byte is sent sequentially or serially over the communication bus. The I^2C protocol is implemented using the Master Synchronous Serial Port (MSSP) module on the PIC [44], while the SCI protocol is implemented using the Enhanced Universal Master Synchronous Receiver Transmitter (EUSART) module [44]. Both protocols have the added benefit of using only two wires to implement communications, thus reducing the complexity of the functional circuit.

The I^{2}C protocol was used to interface the PIC with an external EEPROM memory chip to temporarily store the acquired data. The SCI protocol is more general and is most commonly used to implement communications between PC's and peripherals. In fact the standard RS-232 com port found on computers, utilizes a UART module to implement the SCI protocol. The SCI protocol was used to interface the PIC with the uMMC Memory module in order to permanently store all acquired data to an SD card for easy retrieval.

The I^{2}C and SCI protocols are very similar in their structure even though they use two different hardware modules in their implementation. Both protocols use a Master/Slave asynchronous structure to implement their communications as illustrated in Figure 42.

Figure 42: Master/Slave Asynchronous Framework

In a Master/Slave framework, the master device controls all communication protocols including initiation of the transfer and clock pulses which time the transfer. A transfer is initiated by the master device sending a start bit, followed by a control byte and finally a stop bit. Depending on the protocol being used, the slave device will either respond to the master device or silently acknowledge that it received the data.

In the case of this research the PIC is considered the master device with the EERPROM and uMMC acting as slaves. In this type of communication, the master device initiates all communications as well as governs the clock rate used to shift data over the communication bus. The frequency of the clock pulse used within the communication protocol is known as its Baud Rate.

In the case of the PIC, both the MSSP and EUSART modules use an internal Baud Rate generator that is user programmable [*44*]. Even though the two devices are operating at the same baud rate, it is still necessary to notify the slave of any subsequent data transmission. This is accomplished by the master device sending a start and a stop pulse to let the slave know when data is to be transmitted. This type of communication is known as asynchronous because the start pulse acts to synchronize the two devices so the slave is able to properly interpret any subsequent transmission. The implementation of these protocols within the PIC hardware is highlighted

within the appendices; however, for a detailed overview it is recommended that the manufacturer datasheet for each device be consulted.

4.2.3 Memory Chip

It was necessary to interface the PIC with an external memory chip in order to temporarily store all data before it could be downloaded to a memory card for easy retrieval. This is because the A/D converters generate 10-bit numbers and therefore requires 2 bytes to define each data point. With a high sample rate of 10 Hz, using the onboard memory cache found on the PIC would result in it quickly becoming overrun after several seconds. Therefore, an external memory chip was required, with the Microchip 24AA1025 EEPROM being chosen due to its high memory density, low cost and high transfer speeds. The chip is specially designed for data acquisition applications and offers up to 1 MB of memory and transfer speeds of up to 1 MHz [45].

The memory chip also has the ability to write a single byte of data at a time or up to 128 bytes in page write mode. In this mode the 128 bytes of data can be written to memory in approximately 3ms . The high transfer speeds and page write capability were critical in having the acquisition system achieve high sample rates.

Figure 43 highlights the EEPROM's pin layout used to interface with the PIC. Note that all pins are considered digital inputs. Therefore connecting a pin to the supply voltage (V_{DD}) gives it a logic value of 1, while connecting a pin to ground (V_{SS}) gives it a logic value of 0.
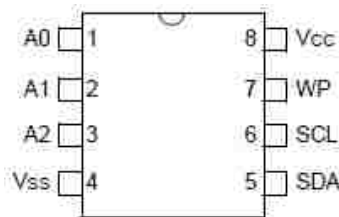
Figure 43: 24AA1025 EEPROM pin diagram

Figure above illustrates the pin layout of the EEPROM used to temporarily store the acquired data. All pins are considered digital inputs and therefore connecting them to V_{DD} is considered a logic value of 1 and connecting them to V_{SS} is a logic value of 0. Figure taken from EEPROM datasheet [45].

A0, A1 – Chip Address Inputs

Up to four devices may be connected to the same bus by using different Chip Select bit combinations. In most applications, the chip address inputs A0 and A1 are hard-wired to Vcc or Vss.

A2 - Chip Address Input

This pin is non-configurable and must be connected to VDD in order for the device to operate.

SDA - Serial Data

This is a bidirectional pin used to transfer addresses and data into and out of the device. This pin must be connected to the corresponding SDA pin on the PIC to ensure proper data transfer.

SCL - Serial Clock

Pin used to transmit the clock pulse generated by the master device. The clock pulse is used to synchronize the data transfer process.

WP - Write Protect

If connected to Vss, write operations are enabled. If connected to V_{DD}, write operations are inhibited, but read operations are not affected.

4.2.4 uMMC Storage Module

In order to easily access the data collected by the acquisition system it was necessary to offload the data to a removable storage medium. To perform this task the uMMC storage module illustrated in Figure 44 was used. The uMMC is a small footprint, serial data logger that is capable of reading and writing data to SD cards [*46*]. Data can be written up to the full capacity of the memory card and read by a standard card reader on a computer. The uMMC stores data using basic text files which means an inexpensive 128 MB SD card can store several hours of test data.

Figure 44: uMMC storage module

The uMMC storage module is used to permanently store all acquired data to a standard SD memory card for easy retrieval. Data is stored as text files which allows for several hours' worth of data to be stored on a low cost memory card. Figure taken from uMMC documentation [*46*].

Specifications:

The uMMC module communicates using a standard SPI serial port which operates with a user selectable Baud rate of 9600, 19200, 38400, 57600 or 115200 bits/s. The serial port is connected via transmit and receive pins illustrated in Figure 45. The communication is asynchronous and requires a start and a stop bit to be sent to let the uMMC know about incoming data. This serial communication was easily implemented using the built in EUSART module on the PIC microcontroller. Once the EUSART is properly configured to operate at the specified Baud Rate then it was a simple matter of sending data bytes to the EUSART'S transmit register. The EUSART automatically serializes the data with the proper start and stop bits and sends it over the serial bus. For a detailed overview of the uMMC communication bus, refer to the manufacturer's datasheet [*46*].
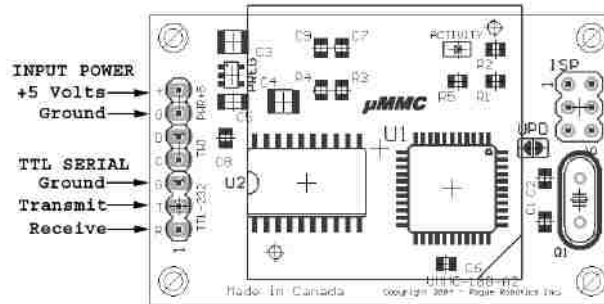
Figure 45: uMMC memory module interface diagram

As shown above the uMMC requires a regulated 5 V supply voltage in order to operate. Transmit and receive pins must be connected to the appropriate EUSART pins on the PIC in order for proper data transfer to take place. Figure taken from uMMC documentation [*46*].

The uMMC uses a standard FAT32 file system which needs to be formatted to the memory card using a computer upon first use. The device does not have the ability to format memory cards on its own. The uMMC has the ability to open and operate on up to 4 data files at the same time. An internal page buffer allows the uMMC to receive up to 512 bytes of data before issuing a read/write cycle. This page write function allows for much faster write speeds and was utilized within the acquisition algorithm. Refer to the manufacturer datasheet for the list of commands to implement write operations on the memory module [*46*].

4.2.5 Circuit

The circuit required to interface all of the components discussed so far was developed on a breadboard prototype kit which is illustrated in Figure 46. By using the breadboard to build the circuit, it was possible to quickly prototype the circuit by plugging in the components and attaching jumper leads to their respective pins. However, the downside of using breadboards is that they introduce high frequency noise into the functional circuit due to the interconnections between each rail. This high frequency noise can potentially cause integrated electronics, such as microcontrollers to respond erratically since fluctuations in the supply voltage or signal lines will be interpreted as commands.
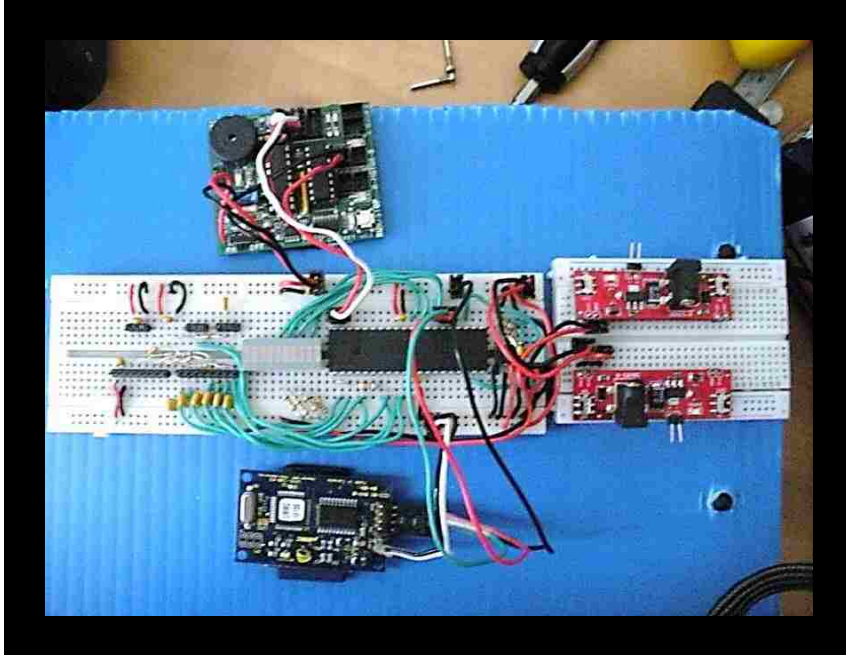
Figure 46: Functional acquisition module circuit

Acquisition module implemented using breadboard prototype kit as shown above. Module consists of the PIC microcontroller, uMMC memory module, serial EEPROM, Handy Cricket and voltage regulator boards. An LED array is wired just left of the PIC in order to display messages to the user.

After extensive testing of the acquisition system with the breadboard, it was found that the noise level was sufficiently low to allow the PIC as well as the other components to function as intended without any impact to their performance. Due to time constraints and the flexibility to change the circuit during testing, it was decided to use the breadboard configuration for the remainder of this research rather than etching the circuit to a circuit board. The wiring of each pin on the PIC is presented in the appendices for reference.

Power Distribution:

All components of the acquisition module are powered using two supply voltages, 5 V DC and 3.3 V DC. It was critical to regulate these supply voltage to ensure a clean stable signal was being supplied to each device. Rather than wiring a voltage regulator circuit, a dedicated regulator board was used. The PTR-09319 voltage regulator board shown in Figure 47 can be purchased from Sparkfun.com and accepts a DC supply voltage via a standard barrel connector or a two pin header. It is specially designed to connect directly to breadboard prototype circuits. The user can select the output voltage of either 5V or 3.3 V via a switch.
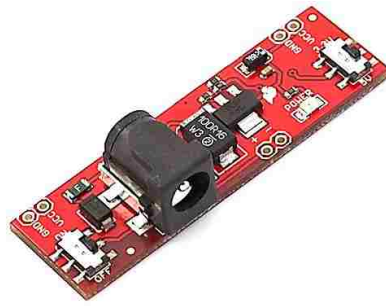
Figure 47: Voltage regulator board

The PTR-09319 voltage regulator board was used to provide a steady 5 V and 3.3 V rail supply to the acquisition module. The board accepts a DC voltage via a standard barrel connector or 2-pin header.

The supply voltage is provided by a 9V DC NiCd battery pack with a capacity of 2400 mAh. This pack provides enough charge to power the acquisition system and its associated transducers for several hours. Two regulator boards were used to implement the rail voltages with a 5V rail supplying the PIC, uMMC, EEPROM and Cricket. A 3.3 V rail supplied power to the Razor 6 DOF inertial measurement unit, used to capture the vehicle's motions. Lastly, a $0.1\mu F$ capacitor was connected across the V_{SS} and V_{DD} pins of each device. This decoupling capacitor acts to smooth out the power signal and prevents any fluctuations or drop outs which could cause the devices to function erratically.

Anti-Aliasing Filter:

Recall that an anti-aliasing filter is required ahead of the A/D convertor in order to prevent high frequency noise from corrupting the acquired data. This was accomplished by implementing the RC circuit shown below for all transducer channels. Values for the resister and capacitors needed to specify a particular cut-off frequency is governed by the following equation. Table 5 lists the values used within this research.

Figure 48: RC low pass filter circuit

The RC circuit depicted above implements a low pass filter with a cut-off frequency governed by Equation 52. Figure taken from Nilsson [*42*].

RC Low Pass Filter:

$$f_{cut-off} = \frac{1}{2\pi RC} \qquad (52)$$

Table 5:   RC low pass filter parameters

Component	Value
Resistor	100 kΩ
Capacitor	0.4 μF
$f_{cut-off}$	4 Hz

4.3 Transducers

4.3.1 Inertial Measurement Unit

Recall that the bicycle model predicts the behaviour of two state variables, yaw rate and lateral velocity. The yaw rate can be captured with the use of a yaw rate sensor, which is made up of a gyro that develops a voltage proportional to its angular velocity. The lateral velocity is more difficult to directly measure, so instead the lateral acceleration can be collected and analysed as a substitute. Fortunately, these two sensors are usually packaged into a single integrated sensing module known as an inertial measurement unit (IMU).

For this research the low cost and small footprint Razor 6 DOF IMU was utilized and obtained from Sparkfun.com. This IMU is able to not only collect the channels highlighted above, but can also acquire the roll rate, pitch rate and vertical acceleration as well. Recall that when sampling a time varying signal it is important to filter out any unwanted high frequency content to prevent aliasing. Fortunately, the IMU is configured with hardware filters that limit the sensors to a bandwidth of 0.5-20 Hz for yaw rates and 0-20 Hz for acceleration. However, due to the high bandwidth of 20 Hz it was still necessary to implement the anti-aliasing filter discussed previously. This guaranteed that no aliasing artefacts were present in the data. Lastly, the IMU provides amplified output voltages which eliminates the need for additional conditioner electronics and allows the transducer to fit easily within the E-Maxx's packaging.
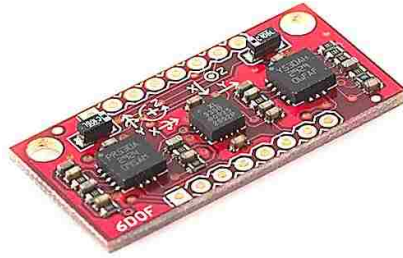
Figure 49: Razor 6DOF IMU

The Razor IMU consists of the ADXL335 three axis accelerometer, the LPR530AL yaw rate sensor and the LY530ALH dual axis gyro for measuring all six degrees of freedom. An amplified output is provided so additional conditioner electronics are not required.

The Razor IMU module consists of an ADXL335 three axis accelerometer, a LPR530AL yaw rate gyro, and a LY530ALH dual axis gyro for measuring pitch and roll rates. All three sensors are linear, with their calibration constants shown in Table 6. A self-calibration feature is provided to ensure that the module is functioning properly. By connecting the V_{test} pin to the supply voltage, the IMU produces reference voltages at the output pins which can be compared to the manufacturer's recommended levels.

Table 6: IMU calibration constants

Transducer	Channel	Calibration Constant
Acceleration	A_x, A_y, A_z	300 mV/g
Angular Velocity	G_x, G_y, G_z	3.333 mV/deg/sec

4.3.2 Steering Potentiometer

The steer input measurement defined by the bicycle model is with respect to the wheels themselves, and therefore is not easily measured directly. Looking at the Emaxx's steering system illustrated in Figure 50, the steering geometry can be classified as a parallel link configuration. The two parallel links are known as the Pitman arm (driven by the servo) and the idler arm. By measuring the angle of the Pitman arm, it is possible to determine the angle at the wheel by knowing the kinematic relationship of the steer linkages.
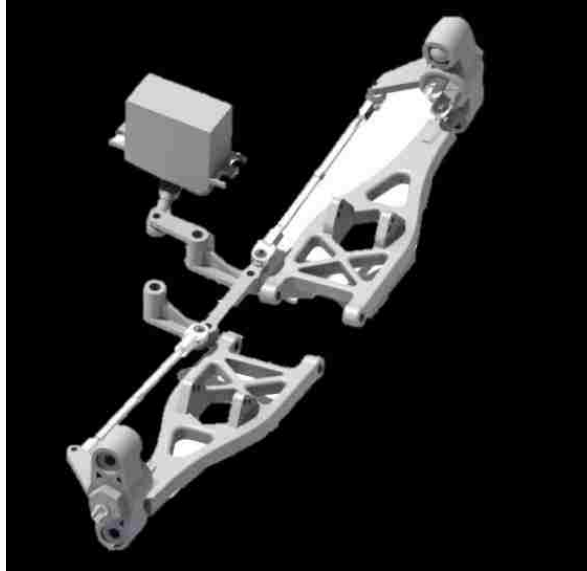
Figure 50: Parallel Link Steering Geometry

CAD model represents the steering linkage used on the E-Maxx. Steering input from the servo is transmitted to two parallel links. The two links translate a cross-car link which ultimately transmits the steering inputs to the wheels through the tie-rods.

To measure the Pitman arm angle, a bracket was attached to the vehicle chassis such that a potentiometer could be mounted along the vehicle centerline shown in Figure 51. The potentiometer is attached to the center of the cross-car link by a sensing arm. It is seen that the sensing arm and the pitman arm are parallel and therefore will rotate at the same angle, thus transferring the pitman arm rotation to the potentiometer where it can be acquired. Care was taken to ensure that any play in the joints of the potentiometer and the sensing arm were minimized. This resulted in a more accurate measurement and the avoidance of any high frequency vibrations that could corrupt the measurement.

Figure 51: Steering potentiometer mounting

The above figure illustrates the brackets used to mount the steering potentiometer to the E-Maxx. A sensing arm is attached to the potentiometer and fixed to the cross-car linkage. The sensing arm is parallel to the pitman arm, ensuring that the potentiometer is measuring the pitman arm angle. Calibration was performed to relate the potentiometer reading to the wheel angle as required by the bicycle model.

In order to calibrate the sensor a digital level was fixed to the outside surface of the tire and servo commands were issued to steer the front wheels. The voltage measured by the potentiometer and the digital level reading were recorded and a calibration constant obtained as shown below.

Steering Potentiometer
Calibration Constant:

$$K_{Steer} = 0.7425 \ rd/Volt \qquad (53)$$
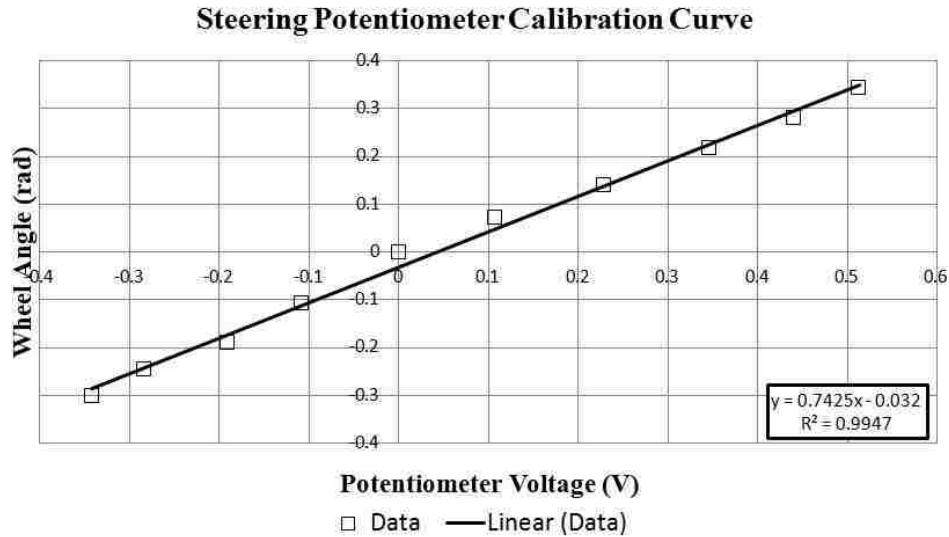
Figure 52: Steering potentiometer calibration curve

It is observed that the calibration curve obtained relating the steering potentiometer voltage to wheel angle is linear with a calibration constant equal to 0.7425 rad/V. Results were obtained with the suspension in its fully extended position.

4.4 Acquisition Algorithm

4.4.1 Programming Environment

Tools:

To understand how to develop firmware for a PIC microcontroller, it is necessary to recall that the PIC only understands binary numbers. Therefore, any firmware that is loaded to the PIC's program memory must be in binary format. Luckily, the programmer is not forced to write code in binary, but instead tools are available that allow for code to be written in more manageable high level languages such as C or C++. A compiler converts the high level code to the binary format that the PIC can understand. There are also other levels of abstraction between the binary code and the high level languages as illustrated in Figure 53.
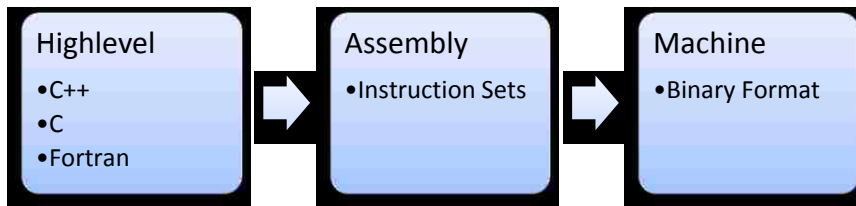
Figure 53: Levels of abstraction within programming languages

The highest level of abstraction includes the more general languages such as C++. The lower level of abstraction includes machine language which uses the binary format. In between these two levels is the assembly language, which uses a standard instruction set that the microcontroller can execute. Assembly language requires the programmer to understand how the microcontroller internally executes a set of instructions in order to effectively program firmware.

The intermediate level of abstraction is assembly code. Assembly code offers user understandable commands; however, each command is mapped to a specific instruction that the PIC can perform. Therefore, it is necessary to have an intimate understanding of how the PIC works in order to develop code in assembly language [*43*]. The tool used to convert the assembly code to binary is known as an assembler. For this research, assembly language was used because the acquisition algorithm required direct access to low level PIC functions such as operating the A/D converter module which minimized the benefit of using higher level languages.

Microchip offers a free full featured integrated development environment called MPLAB IDE which was used to develop the acquisition firmware. Figure 54 shows the MPLAB interface which consists of three main components, the editor, project manager and debugger.
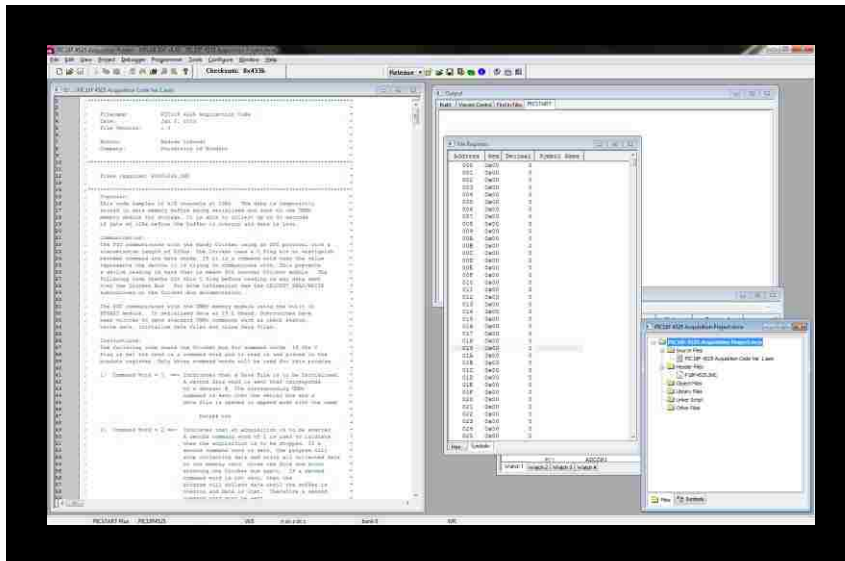
Figure 54: MPLAB IDE PIC development environment

MPLAB IDE is a full featured development environment that Microchip provides in order to program firmware for their PIC microcontrollers. The software suite includes an advanced text editor and debugger. MPLAB even allows the programmer to simulate the execution of their code by simulating the PIC microcontroller in software.

The editor is where the source code is written and is where the programmer will spend most of their time. The project manager organizes all of the different files or objects needed to build a functional code base. The debugger is used to troubleshoot the code and can simulate many of the PIC's functions or behaviour.

Development Process:

The process involved in writing an application is often described as a development cycle, since it is rare that all of the steps from design to implementation can be done flawlessly the first time. More often code is written, tested and then modified in order to produce an application that performs correctly. The Integrated Development Environment (IDE) allows the developer to progress through this cycle without the distraction of switching among an array of tools [*43*]. This process is illustrated in Figure 55.
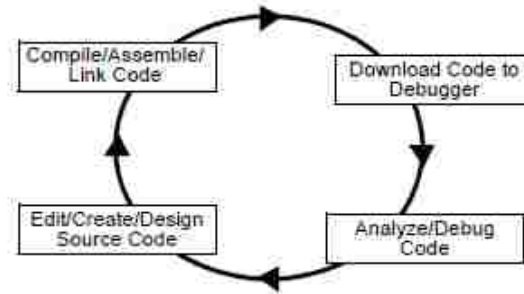
Figure 55: PIC firmware development Process

The development cycle highlighted above illustrates the process involved in developing functional firmware. The process starts with the generation of source code which is compiled and tested using a debugger. The code is then modified and re-tested until the code is free of issues and functions as intended. Figure taken from Katzen [*43*].

Source Code:

      All code is written within MPLAB's editor. It is similar to other development text editors and offers debugging tools and other options to help with troubleshooting. Using assembly language requires knowledge of how the PIC operates and its various functions.

Build Process:

      The build process is made up of three components, the source code, assembler and linker which are illustrated in Figure 56. The source code and assembler have already been discussed; however, the linker is what organizes the code within the PIC's memory. Therefore, it requires knowledge of the PIC's architecture which it receives from Object File Libraries. These libraries contain the configuration of the PIC and allow the linker to properly organize the code within its memory. As a result of the build process two files are generated, a debug file and an executable file. The executable file is what is eventually loaded into the PIC.
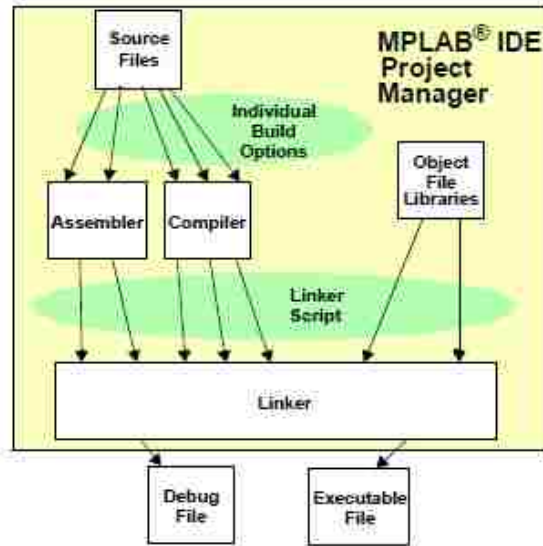
Figure 56: Firmware build process

The process of building binary a file that the PIC can use is highlighted in the figure above. Source code is sent to an assembler or compiler where it is converted to binary format. A linker is used to organize the binary data within the PIC's memory registers. In the end an executable file is created that will be loaded to the PIC's program memory. Figure taken from Katzen [*43*].

Debugger:

MPLAB has a full featured debugger that is able to simulate all PIC microcontrollers in software. All aspects of the PIC are simulated from the timing of clock cycles to the use of modules such as the serial ports and A/D converter. Therefore, the source code can be fully tested without having to load a program to a single piece of hardware. The debugger was extremely useful in developing the acquisition algorithm because it greatly reduced the time it took to iterate the design by allowing all aspects of the code to be investigated without having to load it into the PIC every time.

Loader:

A hardware loader is used to physically download the binary executable file generated by the build process to the PIC's program memory. The loader used for this research was the PICStart Plus.

4.4.2 Subroutines

In developing the acquisition algorithm it was important to segment the code into discrete modules or subroutines. The main advantage to this approach is that each subroutine can be

tested individually before being incorporating into in to the larger code base. Also, assigning repetitive tasks such as reading a data port or converting binary data to its decimal equivalent are easily implemented as separate subroutines that are called within the main algorithm. Therefore, before discussing the overall acquisition code, it is necessary to understand how subroutines are handled within a PIC microcontroller.

Recall that a program is nothing more than a list of instructions that the microcontroller is to execute in a particular order. The program counter (PC) is the tool the CPU uses to keep track of which instruction it is to perform. There are two instructions that can be used to manipulate the PC and therefore allow the CPU to jump to specific sections of code [44]. The two instructions are highlighted in Table 7.

Table 7: PIC subroutine instructions

Operation	Description
Call	
Call subroutine	Transfer to subroutine
Return	Transfer back to caller
from subroutine	Pull original PC back from stack

To implement a subroutine the call instruction is used. Two things happen when the CPU executes the call instruction. First, the current PC value is stored to series of data registers known as the hardware stack. Second, the CPU jumps to the new program address associated with the call instruction. The CPU will then proceed to execute the instructions located at the new PC location until it reaches the return instruction. Upon reading the return instruction, the CPU jumps to the original program location by reading the PC value from the hardware stack. The process is illustrated in Figure 57.
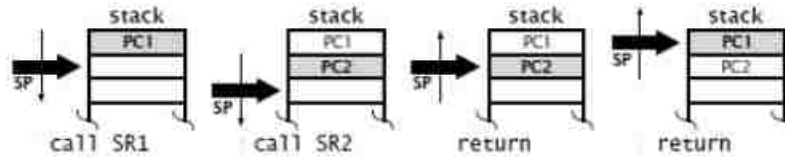
Figure 57: Subroutines - Program stack

Subroutines are implemented by manipulating the program counter (PC) with which the CPU uses to keep track of the next instruction to be executed. Referring ot the figure, when the first subroutine (SR1) is called, the program counter value (PC1) is stored to the hardware stack. A second call adds another PC value to the stack. When the CPU executes a return instruction it reads the last PC value within the stack (PC2) and jumps to that location. A second return instruction reads in the PC1 and allows the CPU to return to the original program location. In this way PIC's are able to execute nested subroutines efficiently. Figure taken from Katzen [*43*].

4.4.3 Algorithm Logic

Recall that the acquisition algorithm is comprised of discrete modules or subroutines that are interfaced together to make up the whole program. In fact, the firmware can be broken down into the five main modules highlighted in Figure 58. The logic involved in executing each of these modules will be discussed next. Detailed flow charts of the logic structure for each subroutine can be found within the appendices.
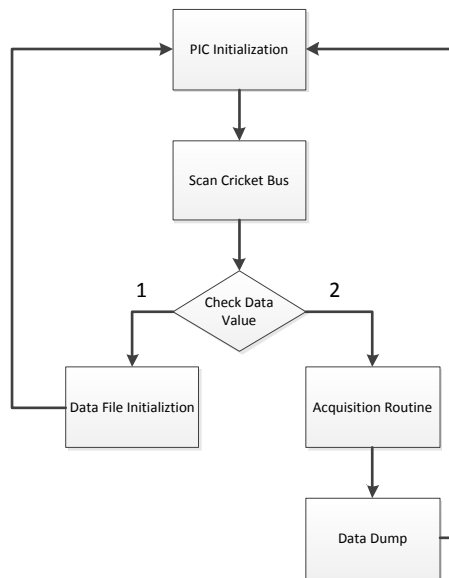
Figure 58: Algorithm logic overview

Acquisition algorithm is broken up into four main subroutines. The PIC initialization routine is used to configure all aspects of the PIC such as the A/D convertor modules and serial communication ports. The Scan Cricket Bus subroutine reads the Cricket bus for potential commands. If it receives a value of one then the Data File Initialization routine is executed. Within this routine the text file used to store all data is created. If a value of two is received then the main acquisition routine is started. Once finished the Data Dump routine is called which stores all data to the SD card for easy retrieval.

PIC Initialization:

The PIC initialization routine is the first section of code that is executed when the system is powered on or after a reset. All control registers are configured at this stage in order to properly enable the hardware modules such as the A/D converter and serial ports. A simple start up routine is then executed which cycles the LED array to indicate to the operator that the chip has been properly initialized. Finally the status of the uMMC storage module is checked by checking the receive register of the EUSART module for the required ">" character. If received, the algorithm continues on to the Scan Bus subroutine.

Scan Cricket Bus:

After the PIC has been initialized it then proceeds to scan the Cricket bus using the CRICKET_READ subroutine. It will do this indefinitely until the Cricket sends a command. There are two command options that can be sent. If the command value sent is equal to one, then the data file initialization routine is called. If the command value is two then the acquisition routine is initiated. Before every test run the data file initialization routine should be called so that a new data file is properly created within the SD card and the data for each run is organized sequentially.

Data File Initialization:

If a command value of one was sent by the Cricket then the data file initialization routine will be called.   The first step in this routine is to scan the Cricket bus for another data byte corresponding to the data set number. The data set number is used to name the data file and keep track of each test run. Once the data set number is received, the algorithm proceeds to send the uMMC command over the serial port to create a text file with the file name DatasetXX.txt, where XX is the dataset value sent by the Cricket.

Acquisition Routine:

The acquisition routine is a nested loop structure which executes indefinitely until signalled by the Cricket to stop acquiring data.   The first two steps of the routine reset two registers that keep track of the memory location within the EEPROM. These are reset at the beginning of each test run so that the full range of the EEPROM memory can be utilized. Next the outer loop is initiated which is responsible for defining the timing of the acquisition or sample rate of the system. The A/D channel is reset prior to entering the inner loop known as the sampling loop.

Within the sampling loop the A/D converter module is enabled and sampling of the current channel begins. The routine proceeds by temporarily storing the data to the PIC's data memory known as the buffer. The A/D convert channel is then incremented by 1 and the process is repeated until all channels are sampled. The data stored in the buffer is then sent to the EEPROM where it is stored. The routine then waits for the remaining sample period to expire and returns back to the beginning of the timing loop to repeat the whole process again.

Note that at the beginning of the timing loop, the RB6 pin is checked, which is how the algorithm decides when to stop the acquisition. Therefore, when the Cricket drives the RB6 pin to zero, the algorithm will call the Data Dump subroutine that begins to send all collected data to the uMMC. The Data Dump subroutine proceeds to read all data from the EEPROM and sends it to the uMMC for final storage to a SD card. The Cricket Bus Scan routine is then called in preparation for another acquisition run.

Chapter 5: Experimental Results

5.1 Test Manoeuvres

In order to properly investigate the dynamic behaviour of the E-Maxx and evaluate the adequacy of the virtual models developed, it was necessary to carefully construct test manoeuvres that would utilize the linear range of its tires. To properly define the manoeuvres, the linear bicycle model was programmed within Simulink and used to determine the vehicle's response. In addition to the standard state variables of yaw rate and lateral velocity the Simulink program populates other variables, such as lateral acceleration, body slip angle, tire slip angle and vehicle path. The model also uses calibration factors for the steering potentiometer and velocity profiles and calculates the required steer and throttle commands that need to be sent to the E-Maxx in order to carry out the manoeuvre. A script was written that interfaces with the LabJack to send the commands upon user demand. A complete list of response variables defined within the model is shown in Table 8.

Table 8: Simulink bicycle model response variables

Response Variable:	Symbol	Units
Lateral Velocity	v	m/s
Yaw Rate	ϕ	rad/sec
Lateral Acceleration	a_y	g
Body Slip Angle	β	rad
Tire Slip Angle	α	rad
Steer Angle	δ	rad
Vehicle Path X Coordinate	x	m
Vehicle Path Y Coordinate	y	m
Steer Command	V_{Steer}	Volts
Throttle Command	$V_{Throttle}$	Volts

An iterative approach was used to evaluate each manoeuvre using a MatLab script. The script asks the user what type of manoeuvre is to be tested along with the various parameters which define it. Two manoeuvres were constructed to test different aspects of the vehicle's response. These will be highlighted within the remaining subsections.

5.1.1 Scale Test Speed

Recall that the scaling of the tire's cornering stiffness could be manipulated by changing the vehicle's forward velocity. This scaling was performed in Chapter 3 by assuming that the vehicle behaviour at highway speeds would be investigated. The resulting scaled vehicle velocity was 9 m/s. However, there are several practical limitations associated with conducting testing at such high velocities.

First among them is the area needed to conduct the testing. It was found using the Simulink model that a test surface of roughly 50 m^2 is needed to conduct some manoeuvres as illustrated in Figure 59. This is a very large area and may be prohibitive if it is desired to test the vehicle indoors. Also, it would be difficult to control the quality of the test surface for such a large area.
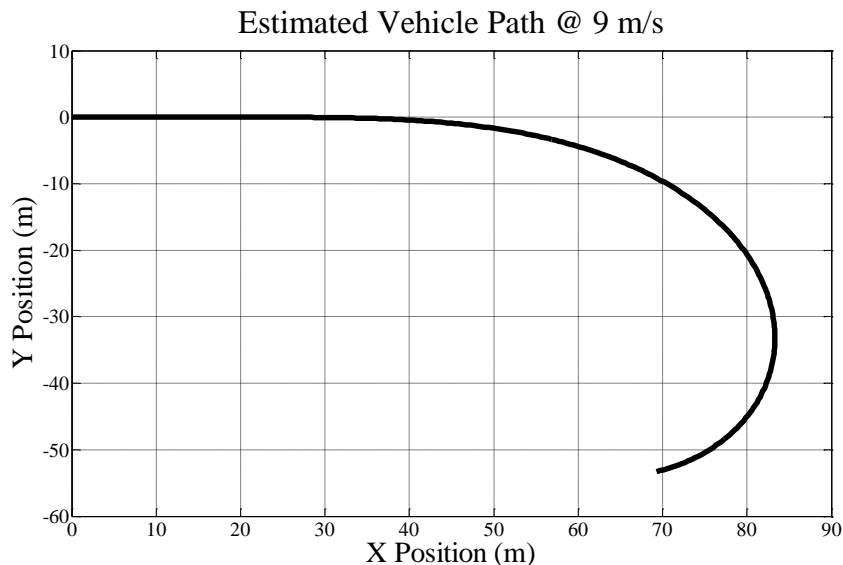
Figure 59: Scale speed issue

Sample test manoeuvre indicating the amount of area that is needed to conduct testing at a forward velocity of 9 m/s. It would be difficult to find a test surface of this size and maintain certain qualities such as flatness and roughness.

Another issue is related to the introduction of un-modeled dynamics. At higher speeds, non-uniformities in the tire as well as small misalignments would be exaggerated and could potentially result in a large amount of wheel wobble. This would introduce higher order dynamics that are not captured by the simplified linear models presented within this research. The introduction of these extraneous inputs will also result in greater system noise and could cause aliasing issues if the sampling rate is too low or anti-alias filtering not used.

Chapter 5: Experimental Results | Andrew Liburdi

Finally, in order test the vehicle within its linear range it was shown that the lateral acceleration will need to be kept below 0.3 g [*13*]. Therefore, the faster the vehicle's forward velocity is, the less steer input is needed to generate the required acceleration. As a result, the smaller steer amplitudes are more difficult to collect due to the resolution of the system and the introduction of signal noise. Therefore, lower velocities will produce data with a higher signal to noise ratio and result in a more reliable data set overall. Taking all of these factors into account and through the use of several simulations, it was found that a vehicle velocity of 4m/s would produce responses which are sufficient to capture the vehicle's linear response while eliminating the issues outlined above.

5.1.2 Double Lane Change

The double lane change manoeuvre is commonly used to test a vehicle's transient response within the time domain. In fact, it is so popular that both ISO and SAE have defined standard lane change manoeuvres with which to test vehicle dynamics. This manoeuvre is mainly used to investigate roll over propensity of large vehicles as well as stability on low friction surfaces. The reason for this is that the quick steer inputs tend to saturate the tire's response, causing the vehicle to reach its handling limit.

To construct the lane change manoeuvre, two Simulink subsystems were created and nested together. The first subsystem implements a single lane change, while second subsystem sequences the single lane change to create the double lane change profile. Using Simulink, the estimated vehicle path can be plotted as shown in Figure 60.

Estimated Double Lane Change Path @ 4m/s
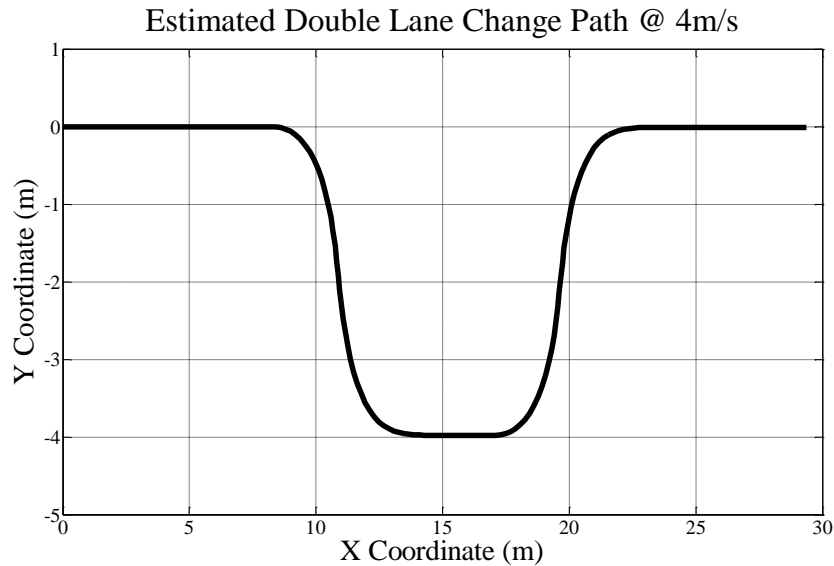
Figure 60: Estimated vehicle path - Double lane change @ 4 m/s

The double lane change path as predicted by linear bicycle model for a forward velocity of 4 m/s.

5.1.3 Sine Sweep

To properly investigate a dynamic system it is necessary to view its response in both the time and frequency domain. Therefore, it is necessary to experimentally determine the vehicle's frequency response so that virtual models can be correlated. To investigate the vehicle's response within the frequency domain, it is necessary to excite the vehicle over a wide range of frequencies. Separate sine waves of varying frequency and amplitude can be sent to the vehicle and the response collected. This would require several test runs and therefore is a very time consuming proposition. Fortunately, sine sweeps can be used to vary the input frequency within a single run and therefore cut down on the number of test runs needed to determine the vehicles frequency response.

There are multiple formulations that can be used to implement a sine sweep wave form. The interested reader is encouraged to consult Tuma [47] for further details on the subject. The form used in this research is shown below and uses a logarithmic sweep, which sweeps octaves of frequency over equally spaced time intervals. This is the most accepted method of excitation since the logarithmic sweep avoids any modulation distortion and allows for the linear transfer function to be separated from any nonlinear modulation components [47].

Sine Sweep

$$Y(t) = sin\left(2\pi\left(\frac{f_1(-1 + 2^{Rt})}{Rln(2)}\right)\right) \tag{54}$$

Where;

$$f_1 = initial\ frequency$$
$$f_2 = final\ frequency$$
$$R = \frac{N}{t_2 - t_1}$$

$$N = \frac{ln\left(\frac{f_2}{f_1}\right)}{ln(2)}$$

Once programmed using Simulink, simulations were conducted to develop an adequate steer profile. Figure 61 illustrates the resulting steer profile, while Figure 62 illustrates the predicted vehicle path. The frequency range of the steer profile is listed below.

Frequency Range:

$$f_{sweep} = 0.1 - 1.5\ Hz \tag{55}$$
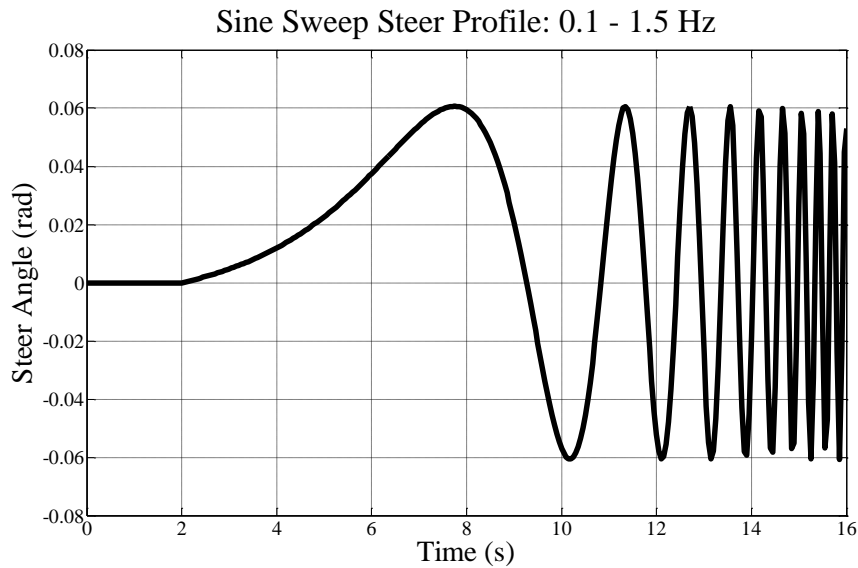
Figure 61: Sine sweep steer input

Steer profile is swept between 0.1 and 1.5 Hz which will be used to evaluate the vehicle's frequency response.

Estimated Sine Sweep Path @ 4m/s
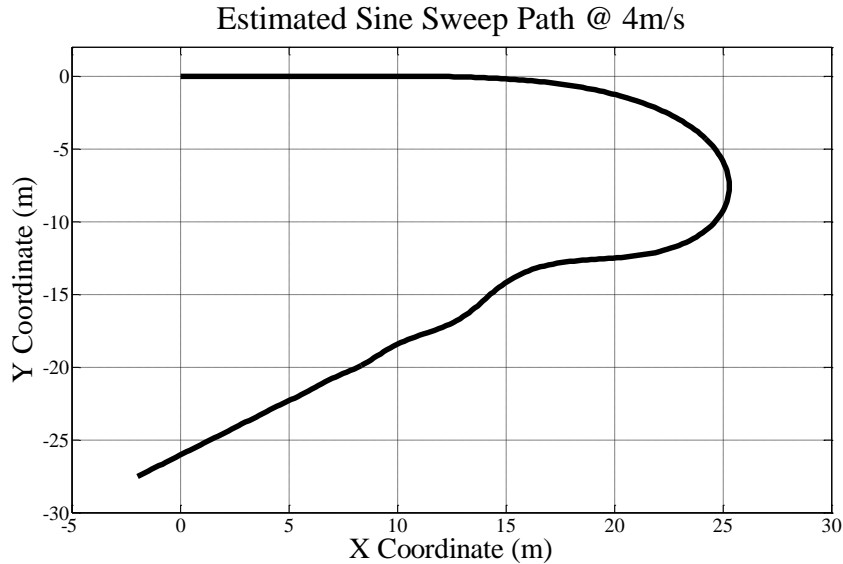
Figure 62: Estimated vehicle path – Sine Sweep @ 4 m/s

The estimated sine sweep vehicle path as predicted by the linear bicycle model with a forward speed of 4 m/s.

5.1.4 Cornering Stiffness

Throughout this thesis the importance of tire cornering stiffness has been discussed several times. This is because it is the dominant factor in dictating the vehicle's handling response as predicted by the bicycle model. Unfortunately, it is also the most difficult property to experimentally measure. In order to properly correlate the response data, the stiffness would need to be obtained for the road surface on which the vehicle is tested. Due to the difficulties of accurately measuring this parameter, it was decided to determine the cornering stiffness through simulation.

A MatLab script was programmed which generated several vehicle responses over a range of cornering stiffness values. A total of 500 values of cornering stiffness ranging between 50 N/rad to 300 N/rad were tested. The best fit response was selected by calculating the least square error between the collected response and that predicted by the bicycle model. The decision criterion is shown below.

Error Function:

$$MIN\left[\sum_{i}^{n}\left(y_{i,\ data} - y_{i,\ model}\right)^2\right] \qquad (56)$$

Where,

$$y_{data} = Collected\ Response$$
$$y_{model} = Bicycle\ model\ response$$
$$i = i^{th}\ data\ point$$

Detailed results obtained from correlating the data will be discussed in upcoming sections; however, it should be noted that both test manoeuvres achieved good fits with the optimization process choosing cornering stiffness within 5% of each other. The closeness in each prediction validates that the optimization method is a valid technique when predicting cornering stiffness values. The exact stiffness values are highlighted in Table 9 with the average value indicated below.

Cornering stiffness:

$$C_f = C_r = 177\ N/rad \qquad (57)$$

Table 9: Calculated cornering stiffness values

Test Manoeuvre	Cornering Stiffness (N/rad)
Double Lane Change	174
Sine Sweep	180

It should be noted that the value of the cornering stiffness obtained above is much lower than that which was published by Polley [*30*] (330 N/rad). This was to be expected since the test surface used within Polley's research was much rougher than that used within this thesis. Also, the tire pressures used by Polley could not be determined and therefore were not matched.

The large discrepancy is mainly due to the inability to properly inflate the Du-Bro tire to a reasonable pressure. The small valve stems made inflating the tire difficult, and leakage around the stems caused the tire pressures to remain around 10 psi. Tire pressure is a significant factor in dictating the tire's cornering stiffness and therefore without properly matching its value, it should not be expected that the two stiffness values match. The low inflation pressures used for testing support the low cornering stiffness values obtained from the optimization routine.

5.2 Test Surface

One of the most important factors in dictating the vehicle's response is the characteristics of the test surface. It was desired to conduct the testing indoors so as to mitigate any extraneous disturbances, such as wind and temperature variation. However, due to scheduling conflicts it

was not possible to reserve floor space large enough to test the vehicle, so outdoor testing was conducted instead. A few issues related to testing outdoors will be discussed next.

5.2.1 Inclination

One of the disadvantages of testing outdoors is trying to find a large enough surface that is flat. Recall that the linear bicycle model does not take into account any type of load transfer that would occur if a vehicle were to traverse an uneven surface. That being said, the surface used for this research was chosen because it was relatively flat. Even though care was taken to minimize these effects, the surface did exhibit small variations in its inclination that impacted the vehicle's response slightly. In order to block these effects from the results, each test run was conducted in a different direction so that the elevation effect would be introduced as a random disturbance rather than cause a bias in the data. The photo in Figure 63 shows the test surface used to conduct all testing. A 30 m^2 section was needed to carry out the testing.
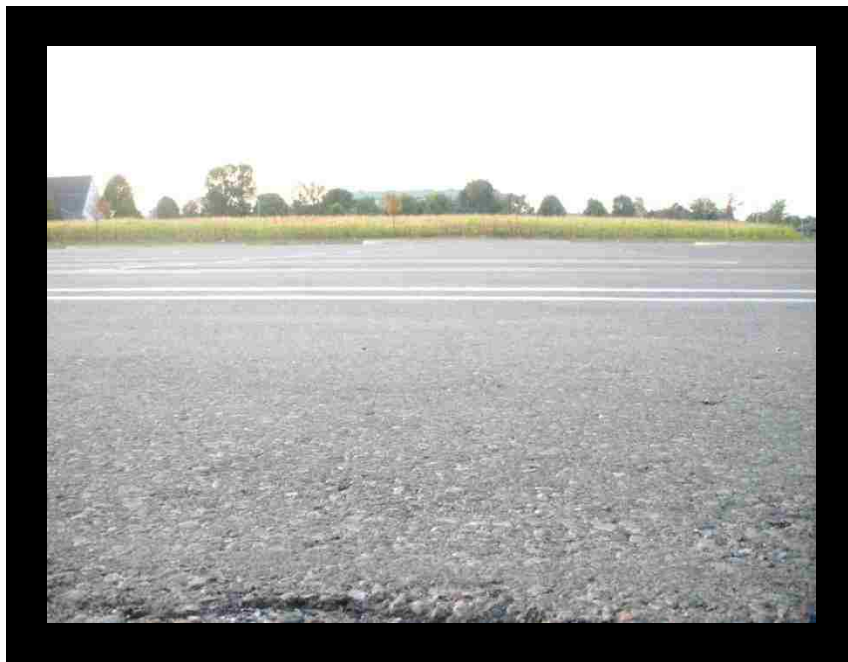
Figure 63: Test surface

The test surface shown above was used to conduct all testing. Care was taken to ensure that the selected surface was as level as possible and that any irregularities were not present. The linear bicycle model does not take into account these effects so they would introduce un-modeled dynamics.

5.2.2 Surface Roughness

The most important aspect of any test surface is its roughness. If the surface is too rough, then tire degradation will be accelerated and could affect the amount of data that can be collected for set of tires. If it is too low, then the vehicle will slide around and not achieve the desired vehicle states required by the investigator. The test surface was made up of asphalt aggregate and provided adequate grip in order to successfully carry out the intended manoeuvres while minimizing the amount of tire wear.

Due to the small size of the vehicle, small surface irregularities such as stones or asphalt joints can become significant disturbances, upsetting the vehicle's handling response. Figure 64 shows some of these irregularities in relation to the E-Maxx tire. As can be seen these irregularities will result in significant vertical motions to the vehicle, which are not being taken into account by the linear bicycle model. An effort was made to remove as many of these irregularities as possible, but some still remained. Therefore, along with analysing key state variables such as lateral acceleration and yaw rate, it is also necessary to review the vertical acceleration to ensure that large disturbances are not present, which could in validate the linear assumptions made by the bicycle model.
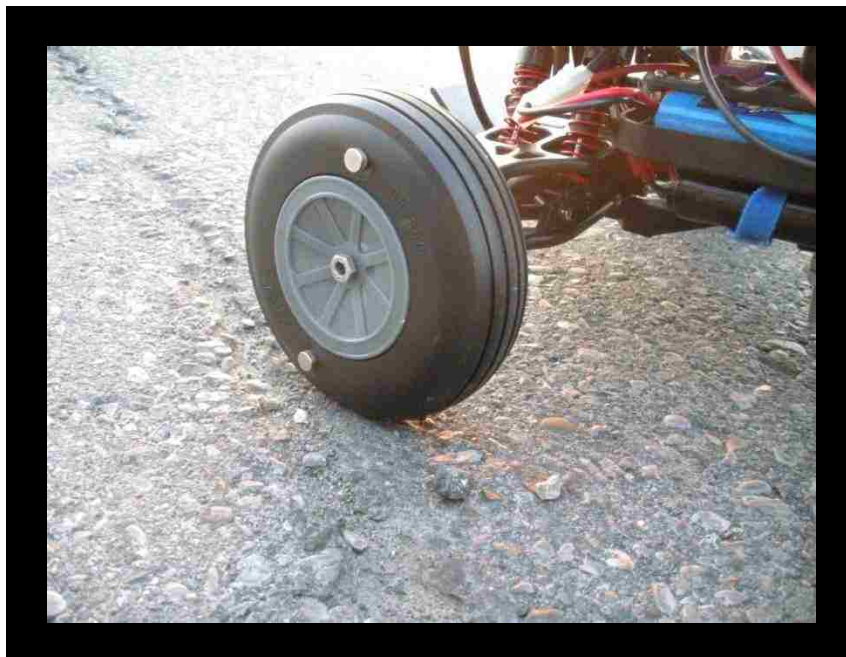
Figure 64: Road irregularities with respect to the E-Maxx tire

Small stones and divots in the asphalt test surface can cause large disturbances to the vehicle due to its small scale. Care was taken to ensure as many of these irregularities were removed prior to testing, however some remained. Vertical and longitudinal accelerations were analyzed in order to determine if these effects were significant in the overall response of the vehicle.

5.3 Time Domain Response

As a first attempt at correlating the data, the vehicle's response will be observed in the time domain. Note that in correlating the data, the simulation process was slightly modified in its execution. Recall that the control system relies on wireless communications, which introduces time delays to the system response. In an effort to by-pass these nonlinearities, the steer angle data was used to drive the linear bicycle model rather than the original steer command. This is justified because only the input/output relationship between the wheel angle and the vehicle's state variables is of interest. Therefore, both the actual vehicle and the virtual model will utilize the same stimulus, with the only difference being how each system reacts to that stimulus.

It was also observed throughout testing that the current draw from the motors and steering servo quickly consumed the batteries. This resulted in the forward velocity of the vehicle varying from manoeuvre to manoeuvre since the same throttle command was being used but the batteries could not supply the same current to the drive motors. Without a direct velocity measurement, it was necessary to use an optimization routine within the Simulink code to determine the approximate vehicle velocity. This was incorporated with the optimization technique used for the cornering stiffness and produced values that were consistent with observations. Specifically, it was observed that the actual test velocity was much lower than the intended 4 m/s due to extra load on the drive system and battery charge. Also, the sine sweep test speed was observed to higher than the lane change speed because the sine sweep was collected first.

5.3.1 Lane Change

Figure 65, Figure 66 and Figure 67 illustrate the steer input profile as well as the lateral acceleration and yaw rate responses respectively. To reduce signal noise for the lateral acceleration and yaw rate channels, a low pass Butterworth filter was implemented within Simulink using a cut-off frequency of 1.0 Hz. The values for vehicle velocity and cornering stiffness obtained from the optimization routine are listed in Table 10.

Table 10: Estimated parameters – Double lane change

Vehicle Velocity	1.74 m/s
Cornering Stiffness	174 N/rad
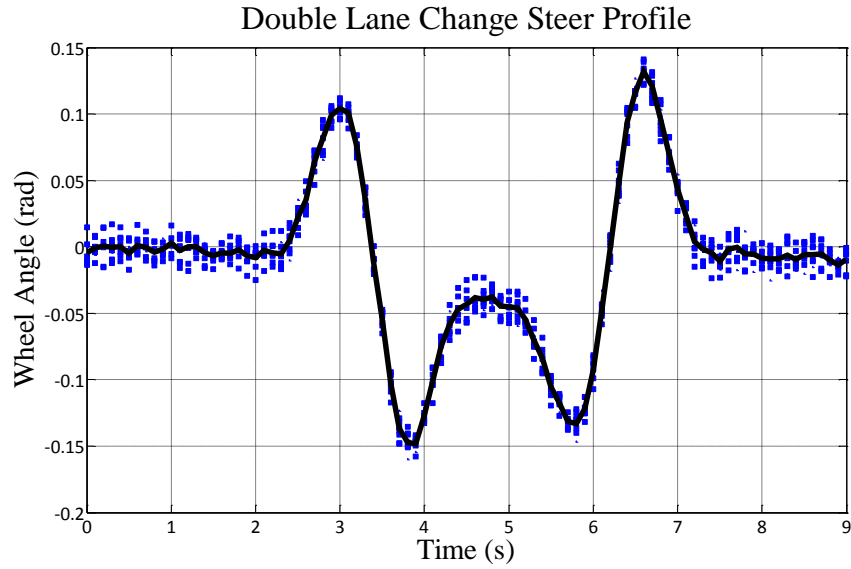
Figure 65: Lane change steer profile

Close grouping is achieved with the steer data indicating the control system is repeatable. Solid line represents the mean steer profile, which is used to drive the bicycle model. Butterworth low pass filter applied with $f_{cutoff} = 1.0\ Hz$.

The steer input profile shows a close grouping in the acquired data indicating that the steering control system is very consistent. The steer input used to carry out the simulations was taken as the average steer input that passes through the data. Due to the close grouping of the steer data, the calculated steer input is a close match and is well suited to drive the bicycle model.

Double Lane Change Lateral Acceleration
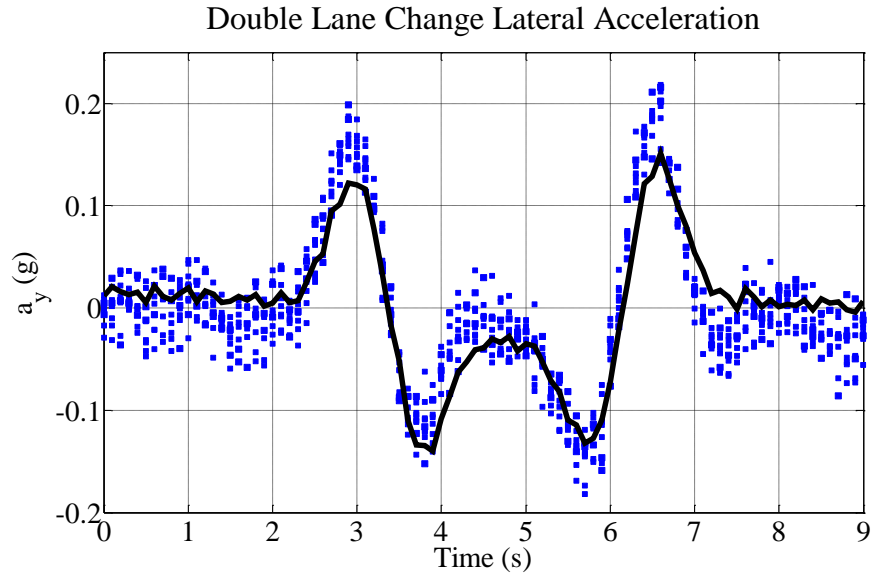
Figure 66: Lane change lateral acceleration response @ 1.74 m/s

Solid line indicates bicycle model prediction. Overshooting present at the peaks and appears to be bias toward positive values. The bias is assumed to be associated with un-modeled dynamics such as steering misalignment, surface inclination or roll steer. Butterworth low pass filter applied with $f_{cutoff} = 1.0\ Hz$. $C_\alpha = 174\ N/rad$.

Sine Sweep Yaw Rate Response
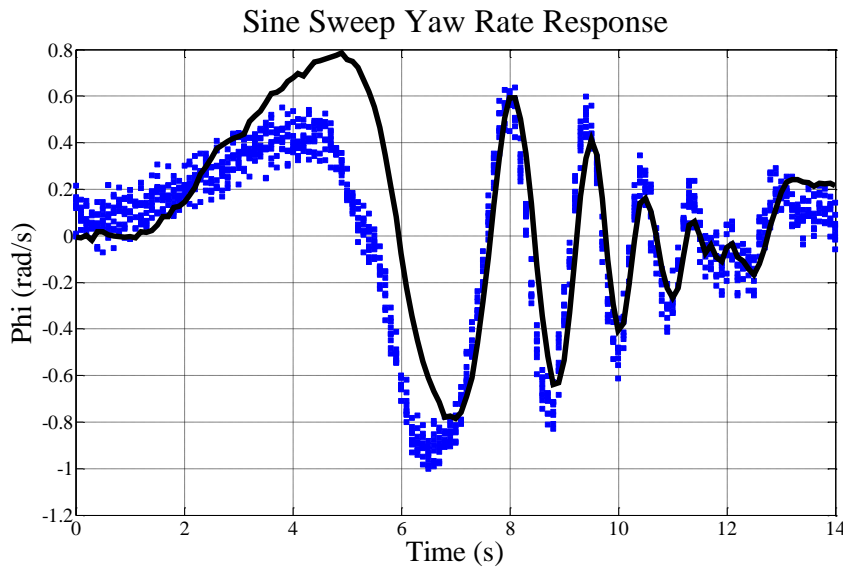
Figure 67: Lane change yaw rate response @ 1.74 m/s

Solid line represents bicycle model prediction, which closely matches data. Similar to lateral acceleration, a slight bias toward positive yaw rates is observed. Overall data appears to be more closely grouped than lateral acceleration, indicating that the yaw rate sensor is more repeatable. Butterworth low pass filter applied with $f_{cutoff} = 1.0\ Hz$. $C_\alpha = 174\ N/rad$.

Chapter 5: Experimental Results | Andrew Liburdi

The above lateral acceleration and yaw rate plots show that the model does a good job at predicting the vehicle's response overall; however, it tends to undershoot at the peaks. The undershooting seems to be biased toward positive accelerations or right handed turns. It is expected that the discrepancy is due to higher order dynamics that are not taken into account by the model.

Several factors that may contribute to this type of issue include steering alignment, roll steer effects, surface inclination and tire non-uniformities. All of these factors could introduce a bias in the acceleration and yaw rate responses for a particular steering direction, though surface inclination is less of a concern because care was taken to randomize its effects by running the vehicle in different directions.

Notice that the maximum lateral acceleration is below 0.3 g, which ensures that the tire is operating within its linear range. Even with the slight bias in the data, it is clear that the bicycle model is well suited at predicting the E-Maxx's transient response and further supports the notion that the bicycle model can accurately predict linear handling behaviour.

The longitudinal and vertical acceleration channels are shown in Figure 68 and Figure 69 for completeness. Their primary purpose is to reveal if the vehicle experienced any abnormal road disturbances that could potentially invalidate the bicycle model assumptions. Looking at the longitudinal acceleration plot shows an event is present between 0-2 seconds. This is related to the vehicle reaching its steady state velocity after accelerating from a stand still. As can be seen the acceleration is ramping down to steady state at the same time the vehicle is starting its initial turn. This slight overlap is not expected to cause any of the bias issues observed previously and can be neglected.
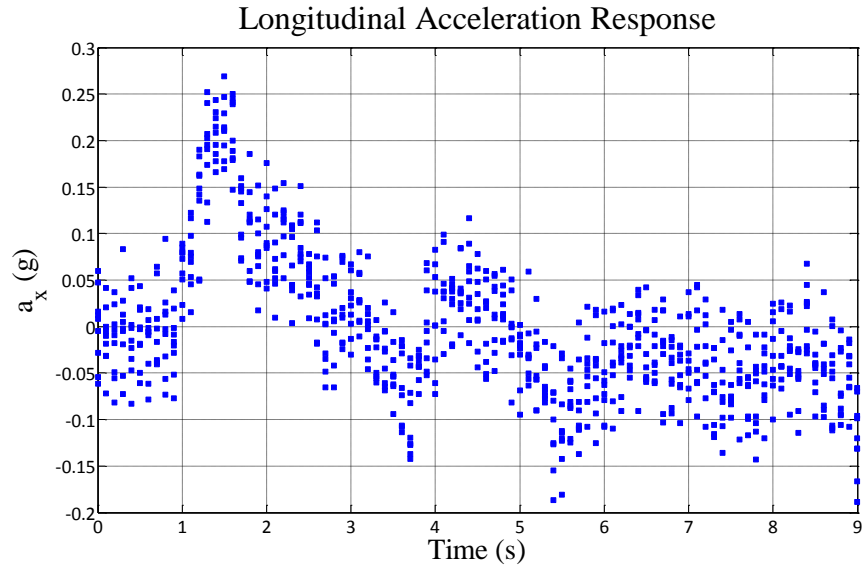
Figure 68: Double lane change longitudinal acceleration @ 1.74 m/s

Longitudinal acceleration data indicates an event at beginning of time history, which is due to the vehicle returning to steady state after accelerating from a stand still. Butterworth low pass filter applied with $f_{cutoff} = 1.0\ Hz$.
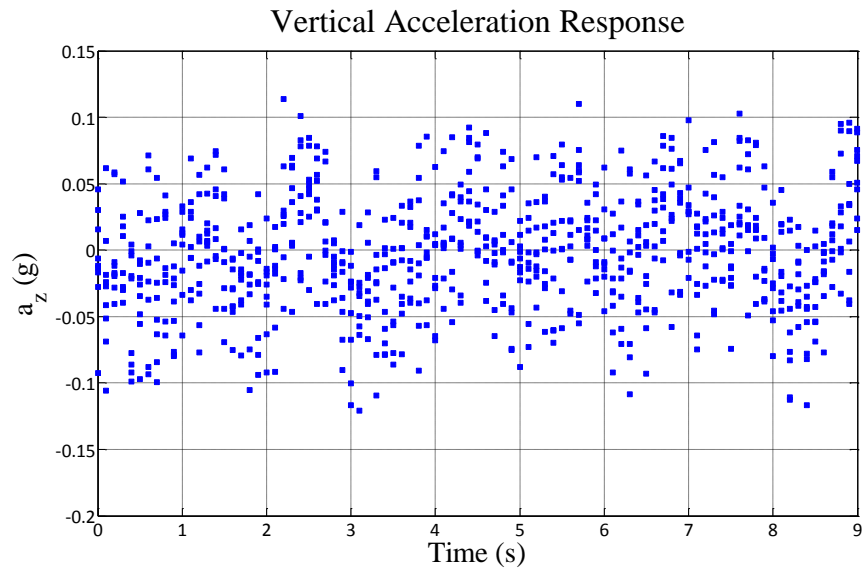
Figure 69: Lane change vertical acceleration @ 1.74 m/s

Uniform distribution in vertical acceleration data indicates flat ride was achieved.

Looking at the vertical acceleration it is seen that its signal levels are very low and indicate that the vehicle is achieving a smooth ride as required by the bicycle model. The results from the longitudinal and vertical acceleration channels further support the use the bicycle model to predict the E-Maxx's response at low accelerations.

5.3.2 Sine Sweep

The steer profile, lateral acceleration and yaw rate responses for the sine sweep manoeuvre are illustrated in Figure 70, Figure 71 and Figure 72. Similar to what was done for the double lane change manoeuvre; a low pass Butterworth filter was implemented within Simulink using a cut-off frequency of 1.5 Hz. The values for vehicle velocity and cornering stiffness obtained from the optimization routine are listed in Table 11.

Table 11: Estimated parameters – Sine sweep

Vehicle Velocity	2.1 m/s
Cornering Stiffness	180 N/rad
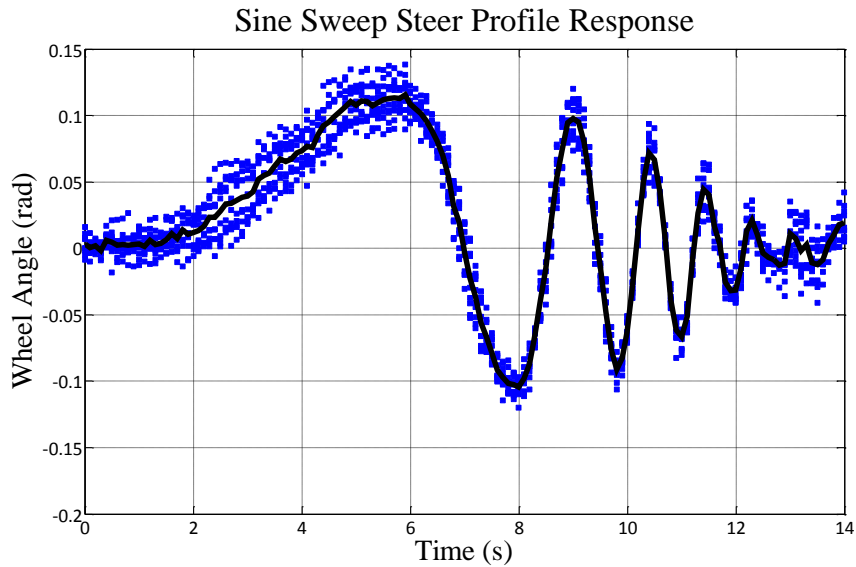
Figure 70: Sine sweep steer profile

Solid line represents average steer input used to drive bicycle model. Good fit is achieved overall; however, the steer profile separates at low frequencies. Separation is due to hysteresis effects associated with the steering linkages.

Looking at the results obtained for the steering profile it seen that the data is very repeatable except for the initial portion of the profile below five seconds. The profile diverges into two closely grouped responses before merging into a single profile at five seconds. It is believed that the separation in the steering profile is due to hysteresis effects. Its presence at the initial portion of the profile is a result of the low frequency nature of the signal in that area. Hysteresis effects are more pronounced at low frequencies and therefore it stands to reason that it would be present in sine sweep profile rather than on the lane change profile due to the lower

frequencies involved. It should be noted that even with the separation at the beginning of the profile, the calculated steer input used to drive the bicycle model matches the data very well.
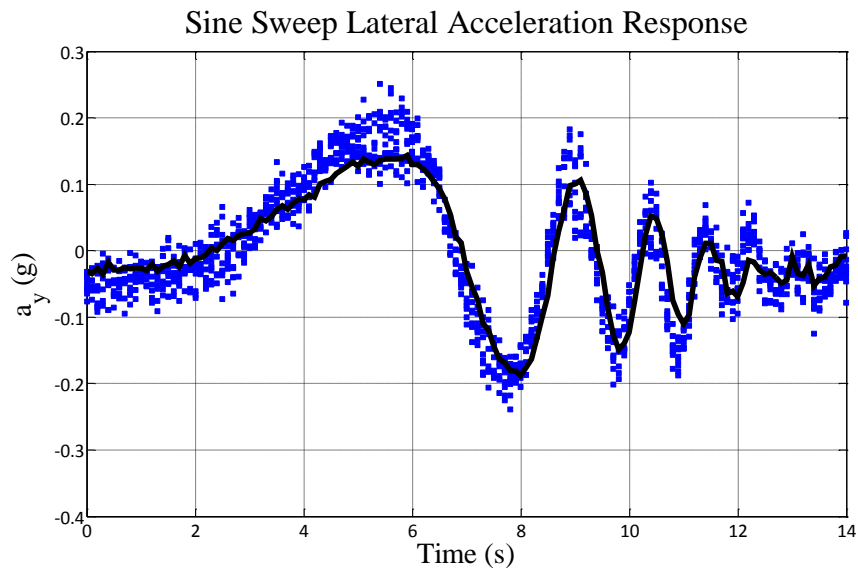
Figure 71: Sine sweep lateral acceleration @ 2.1 m/s

Solid line indicates bicycle model prediction. Model tracks data well however overshooting exists throughout. A bias in the data towards positive accelerations is observed at the first peak of the time history. This is consistent with the double lane change manoeuvre which was attributed to steering misalignment, roll steer or surface inclination effects. A Butterworth low pass filter was applied with $f_{cut-off} = 1.5\ Hz$. $C_\alpha = 180\ N/rad$.
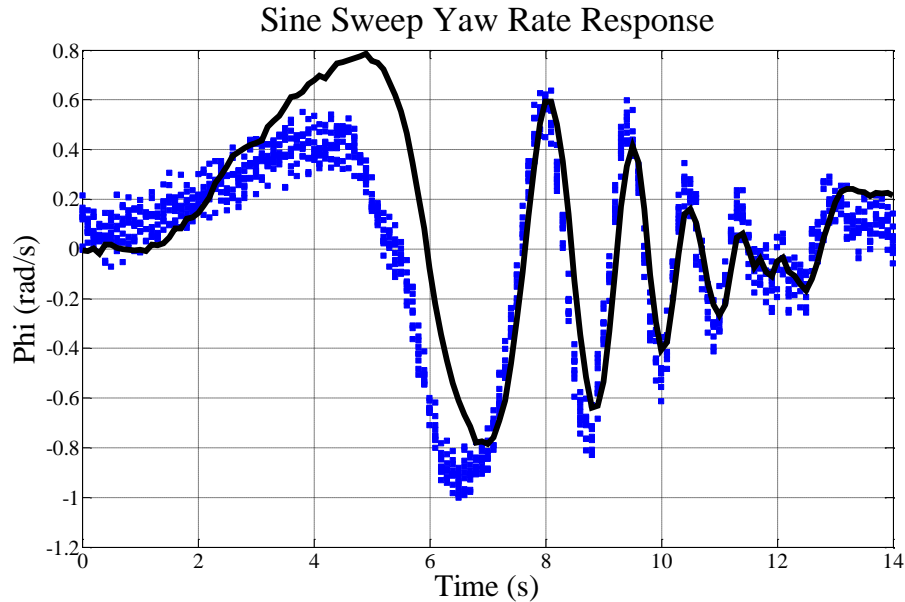
Figure 72: Sine sweep yaw rate @ 2.1 m/s

Solid line indicates bicycle model prediction. Poor correlation is achieved initially within the low frequency portion of the time history but matches well at higher frequencies. The poor correlation is due to a high pass filter wired to the yaw rate sensor which attenuates the data below 0.5 Hz. Butterworth low pass filter was applied with $f_{cut-off} = 1.5\ Hz$. $C_\alpha = 180\ N/rad$.

Looking at the lateral acceleration response in Figure 71 it is seen that the bicycle model once again does a very good job at predicting the lateral response of the vehicle. In fact, the bias issue seems to only be present at the initial low frequency portion of the time history, indicating that the disturbance causing the issue is low frequency in nature. This further supports the hypothesis that steering or suspension alignment is the reason for the bias. These effects show up as offsets or low frequency inputs to the tire and therefore primarily affect the low frequency response of the vehicle.

The yaw rate response is more interesting. It is seen that for the low frequency section of the response, the model over predicts the vehicle's yaw rate. However, as the frequency increases, the two start to merge and correlate well with each other. This behaviour is due to the high pass filter that is built into the yaw rate sensor circuitry. The high pass filter attenuates the sensors response below 0.5Hz. The initial portion of the time history is below this cut-off frequency and therefore the transducer response is attenuated and not able to match the model. As the frequency is increased and passes the filter's cut-off frequency, the transducer output aligns with the model and good correlation is achieved.

Chapter 5: Experimental Results | Andrew Liburdi

Based on the results observed above, the bicycle model once again does a good job at predicting the E-Maxx's response and further validates this approach. The linear assumptions made by the model are validated by the fact that lateral accelerations remained below 0.3g, ensuring linear tire behaviour. Looking at the longitudinal and vertical acceleration channels it is seen that both the constant forward velocity and flat ride assumptions have been met due to the low levels indicated in Figure 73 and Figure 74.
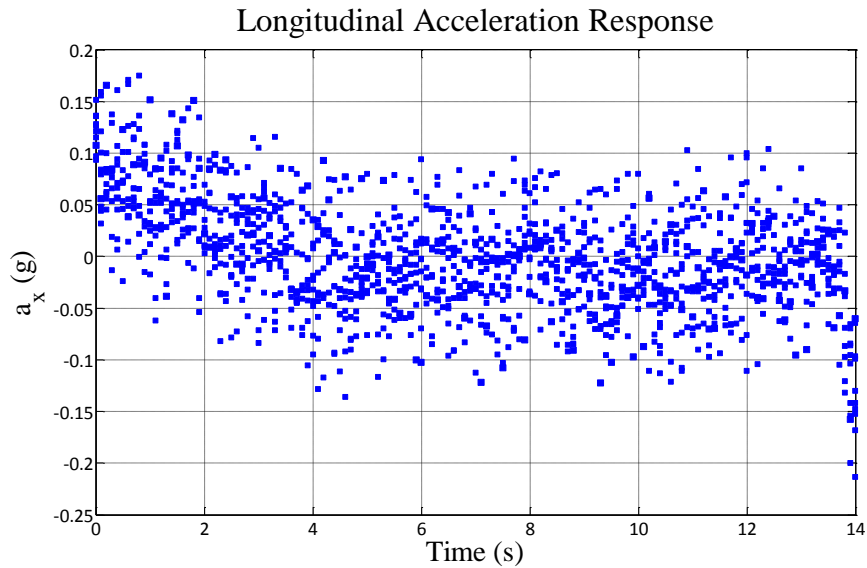
Figure 73: Sine sweep longitudinal acceleration

Uniform distribution longitudinal acceleration data indicates forward velocity remained constant.
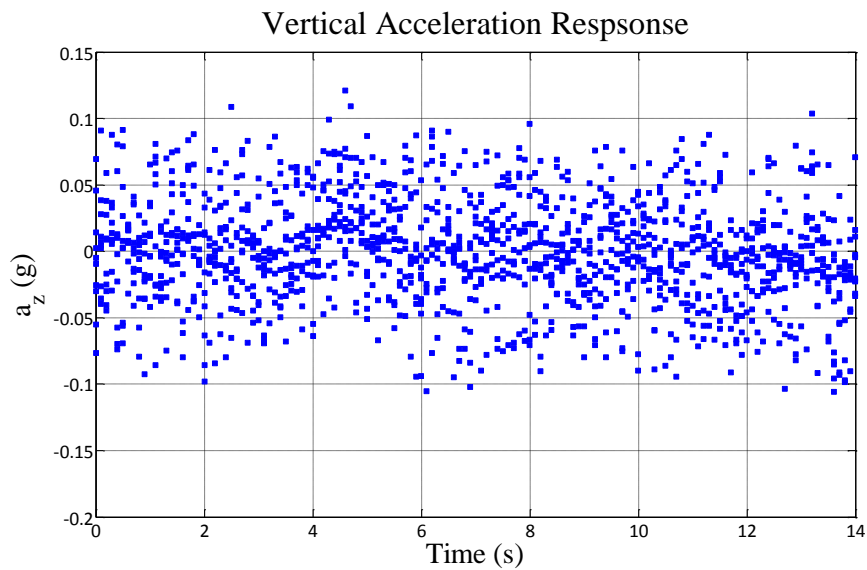
Figure 74: Sine sweep vertical acceleration

Uniform distribution of vertical acceleration data indicates flat ride was achieved.

5.4 Frequency Domain Response

Though the results presented above provided a good idea of how the bicycle model predicts a specific type of manoeuvre, the frequency response of the vehicle illustrates how the vehicle responds to a wide range of inputs. The sine sweep steer input was used to excite the vehicle over a wide range of frequencies so that its response could be recorded. In order to construct these frequency plots, the Fast Fourier Transform (FFT) was used on the data.

5.4.1 Lane Change

Figure 75 through Figure 77 illustrates the steering profile, lateral acceleration and yaw rate responses reconstructed within the frequency domain.
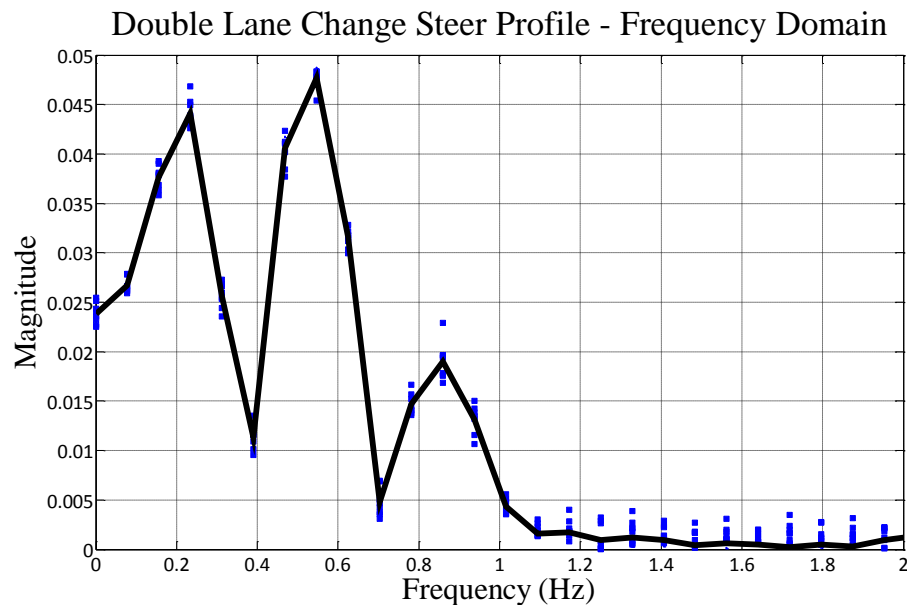
Figure 75: Lane change steer profile - Frequency domain

Solid line represents average steer profile used to drive the bicycle model. The step steer inputs associated with the lane change manoeuvre are represented by three harmonics equally spaced within the frequency domain. Very little content is observed passed 1 Hz due to the Butterworth filter that was applied to the data.

The frequency plot of the steering profile shows three distinct peaks known as harmonics equally spaced apart on the frequency axis at 0.25 Hz, 0.5Hz and 0.75Hz. These harmonics define the step responses shown in the time domain. Notice that all content falls off past 1.0 Hz since that was the cut-off frequency of the Butterworth filters used to edit the data. Never the less, the data still shows some low amplitude content at high frequencies which can be considered

noise. Overall the calculated steering input closely matches the collected data which further supports its use.

Lane Change Lateral Acceleration - Frequency Domain
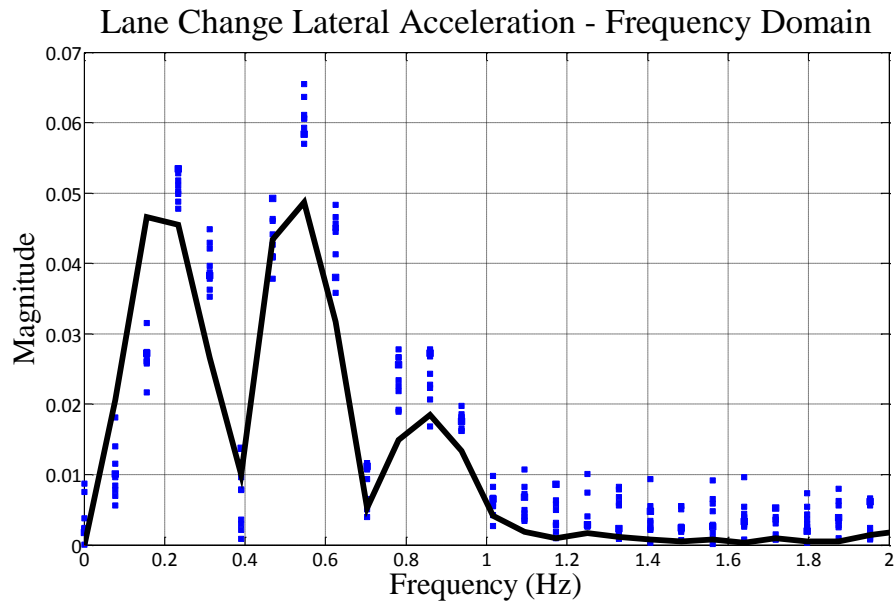
Figure 76: Lane change lateral acceleration – Frequency domain

Solid line indicates the bicycle model prediction. Overall good fit was achieved; however, data tends to overshoot at the peaks. This is consistent with time domain where a bias was observed in the data.

Lane Change Yaw Rate Frequency Response
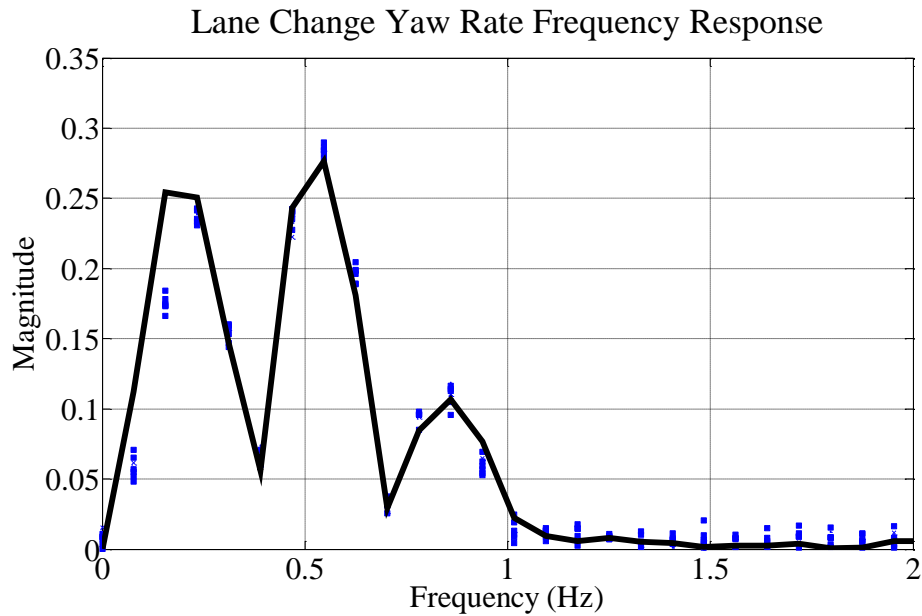
Figure 77: Lane change yaw rate – Frequency domain

Solid line represents bicycle model prediction which correlates well with the data. As can be seen for frequencies below 0.5 Hz, the model over predicts the data due to the high pass filter installed on the yaw rate sensor.

Chapter 5: Experimental Results | Andrew Liburdi

As expected the same three harmonics are present in the lateral acceleration and yaw rate responses. It is also seen that the model undershoots the acceleration data at the peaks of these harmonics. This is consistent with the undershooting observed within the time domain which was attributed to suspension alignment effects. The yaw rate response matches very well with the model, overshooting slightly at frequencies below 0.5 Hz due to the high pass filter. The above results indicate further that the bicycle model can accurately predict the linear behaviour of the E-Maxx.

5.4.2 Sine Sweep

The following figures highlight the sine sweep manoeuvre as well as the vehicle's response as observed within the frequency domain. The main purpose of the sine sweep manoeuvre was to excite the vehicle over a range of frequencies and therefore can be considered the more useful correlation method.
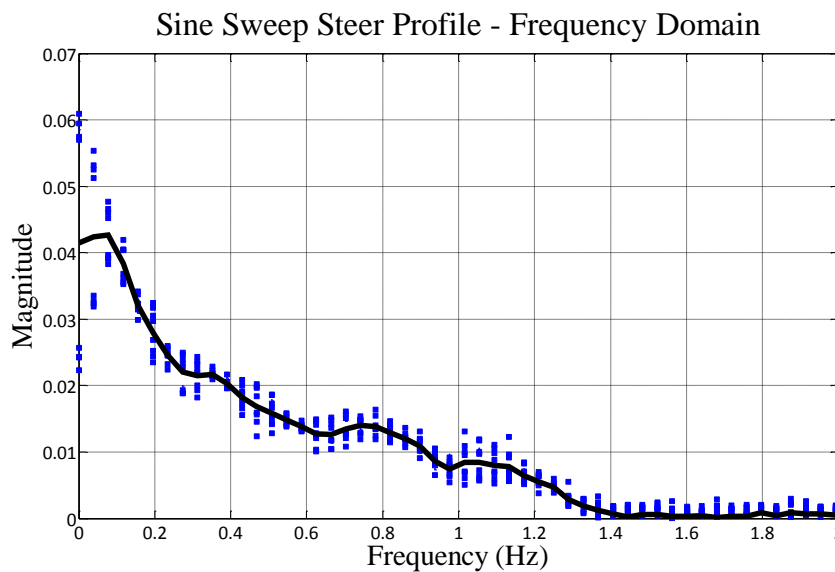
Figure 78: Sine sweep steer profile – Frequency domain

Solid line represents the average steer input used to drive the bicycle model. Good fit is achieved overall further validating its use. Data tends to overshoot at low frequency because of the hysteresis effects found within the time domain.

The frequency content contained within the sine sweep manoeuvre can be observed in Figure 78. It is seen that it does a good job at exciting all frequencies between 0 – 1.5 Hz as intended. Overall the calculated steer input for the bicycle model is an extremely good fit, further validating its use.

Chapter 5: Experimental Results | Andrew Liburdi
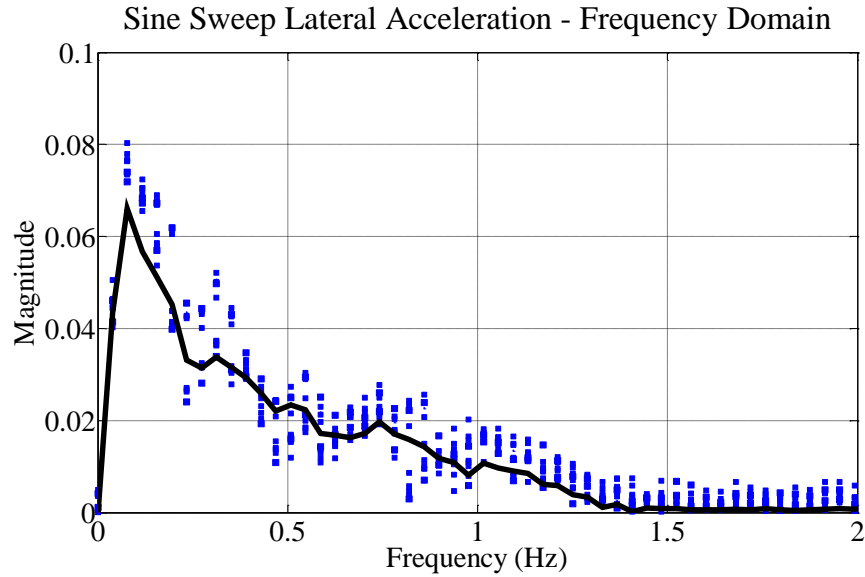
Figure 79: Sine sweep lateral acceleration – Frequency domain

Solid line represents the bicycle model prediction. Most of the overshooting in the data occurs at low frequency (< 0.4 Hz) where it was observed in the time domain that a bias was present. Overall, the model does a good job at following the data even in the presence of the bias issue. It should be noted that the variability in the acceleration data is seen to be greater than either the steer or yaw rate channels.
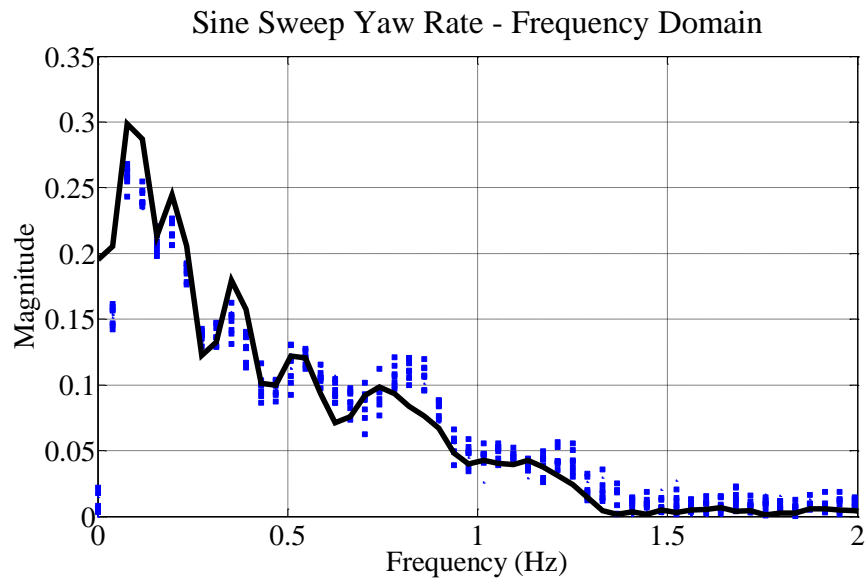
Figure 80: Sine sweep yaw rate – Frequency domain

Solid line represents bicycle model prediction. It is seen that for frequencies below 0.5 Hz the model over predicts the data due to the high pass filter wired to the yaw rate sensor. Otherwise, the model tracks the data very well. There is a small peak in the data at 0.9 Hz which is due to a resonance associated with un-modeled dynamics.

The acceleration and yaw rate response shows that the bicycle model is indeed a good fit for all frequencies except for those near zero Hertz (DC). The undershooting is consistent with the results found in the time domain. The fact that the overshooting mainly occurs near zero Hertz further supports the notion that alignment effects are the reason for the bias in the data since they can be considered steady state or DC disturbances.

5.5 Summary of Results

5.5.1 Correlating the Bicycle Model

Although the ultimate purpose of this test bed is to investigate the nonlinear nature of vehicle handling, it was first necessary to look at simplified linear models to ensure they correlate well. The reason for this is that nonlinear behaviour is simply an extension of the fundamental dynamics predicted by the linear bicycle model and therefore if linear models do not correlate well, then neither will nonlinear models.

The following precautions were taken in the development of the test manoeuvres to ensure that the vehicle remained within its linear range.

1. Lateral accelerations were kept under 0.3g to ensure tire response was linear
2. Forward vehicle velocity kept constant
3. Test surface inclination approximately zero
4. Road irregularities that could cause large vertical disturbances were removed or avoided

The test manoeuvres used within this research consisted of a double lane change steer profile as well as a sine sweep profile. The lane change manoeuvre tested the vehicles transient performance, while the sine sweep investigated its frequency response. Both sets of data were analyzed in the time and frequency domains with the bicycle model achieving good fits for each case.

One issue that was observed from the data was a bias in the acceleration and yaw rate channels for right hand turns. Looking at the frequency domain for the sine sweep manoeuvre, the bias was shown to be at or near zero Hertz. It was hypothesized that the bias was due to suspension or steering misalignment, which would introduce a steady state offset to the tire response [8].

Even in the presence of a signal bias, the bicycle model still predicated the E-Maxx's handling response very well and proved that it is well suited for this application. With the close correlation obtained within this research the model can now be used with confidence and linear control methods investigated.

5.5.2 *Estimating Cornering Stiffness*

One of the benefits of using the Du-bro tire was that tire data was available due to the work done by Polley [*30*]. However, this data could not be used directly since the test conditions used to generate this data could not be fully matched. Therefore, the cornering stiffness values for the test surface used within this research were unknown and needed to be determined.

Due to the difficulties with measuring this parameter, simulations were used to estimate the stiffness based on the vehicle's response. An optimization routine was developed which generated hundreds of vehicle responses over a wide range of cornering stiffness values. The least squares error between the model response and the data was used in order to determine the best fit. The cornering stiffness value associated with the best fit response became the best estimate for cornering stiffness on the road surface with which testing was conducted.

Performing this analysis for two different manoeuvres resulted in the estimated cornering stiffness highlighted below. Note that each manoeuvre predicted values which were within 5% of each other, indicating that the method is consistent.

Cornering Stiffness:
$$C_f = C_r = 177 \ N/rad \qquad\qquad (58)$$

Chapter 6: Conclusions and Recommendations

6.1 Conclusion

Currently, research in the area of vehicle dynamics and control is primarily relegated to virtual simulation. However, in order for the models being developed to have any value, they must be correlated with test data. Unfortunately, due to the prohibitive cost associated with a proper vehicle testing program, the vast majority of work is strictly theoretical. Therefore, it was the focus of this research to develop a vehicle dynamics test bed which allowed vehicle handling to be investigated at a fraction of the time and cost it would take using traditional methods. To accomplish this goal a scale vehicle approach analogous to wind tunnel testing was used to simplify the testing procedure and reduce the costs associated with system setup.

Throughout this thesis the development of a scale vehicle test bed was detailed. The system utilized the Traxxas E-Maxx 1/10th scale RC car, with custom electronics installed to provide control and data logging functions. One of the key aspects of this work that makes it unique compared to similar scale vehicle test beds is that the vehicle is untethered from the acquisition system. This provides the researcher the flexibility to conduct any type of testing they wish. It also means that both the linear and nonlinear regions of vehicle handling can be investigated since the vehicle is free to conduct the most aggressive manoeuvres possible. To accomplish this goal, a custom data acquisition module was developed based on a PIC microcontroller. The system was shown to successfully collect up to 13 channels at a sample rate of 10 Hz, while being fully contained within the vehicle.

To validate the usefulness of the test bed, testing was conducted on the E-Maxx in order to correlate its response with the linear bicycle model. Two manoeuvres were used, a double lane change steer profile to test the vehicle's transient response and a sine sweep steer profile to test the vehicle's frequency response. The bicycle model was shown to correlate well with both manoeuvres within the frequency and time domains. The good correlation that was achieved further validates the use of the bicycle model and provided confidence that it can accurately predict the E-Maxx's behaviour.

With the experimental results validated, all goals defined at the beginning of this research have been accomplished. Specifically, a low cost method with which to test a vehicle's handling

behaviour was demonstrated and validated with actual test data. The custom acquisition module allowed the system to be untethered and therefore provided the maximum amount of flexibility with which to conduct testing. The logical extension of this work would be to start investigating control strategies within the linear region of vehicle handling. The model developed herein was shown to correlate well with the actual vehicle and can be used as an accurate plant model for controls development.

Ultimately, investigating the nonlinear handling behaviour should be the goal moving forward. However, it will be necessary to properly define tire performance if nonlinear effects are to be considered. This is a difficult task and could be the focus of a graduate thesis in itself. With a proper tire model defined, an approach similar to what was presented in this thesis can be used to correlate the models with vehicle data. Once the models are correlated, they can be used to investigate control strategies that stabilize the full range of vehicle behaviour.

6.2 Recommendations

Based on the results highlighted above it is seen that the test bed was successful at achieving the original goals of the project. However, through the course of development some limitations of the system were identified which could be improved moving forward.

6.2.1 Scale Vehicle Subsystem

Many of the difficulties associated with the development of this test bed were related to the small scale of the vehicle. Issues included the inability to measure important vehicle states due to packaging the required electronics. Also, the low mass of the vehicle requires that a test speed upwards of 9 m/s be used in order to test highway behaviour. The development of the acquisition system itself was dictated by the fact that dedicated acquisition systems were too bulky to fit within the vehicle's packaging.

All of these issues can be solved by using a larger vehicle system. This would allow better transducers to be used as well as lower the required vehicle speeds. Luckily, the acquisition system developed within this research is independent of the vehicle subsystem and can easily be integrated onto another vehicle. It should be noted that increasing the size of the vehicle increases the cost associated with the test hardware. It will also increase the risk for potential injury or damage if the vehicle becomes unstable. Both of these were key factors in motivating this research, so a compromise needs to be made between conducting more accurate testing and reducing costs.

Lastly, it would be advantageous that the vehicle be re-configurable. For example, if a specific full size vehicle is to be studied, then it follows that the scale model should be re-configurable such that it can achieve the same Pi parameters as the full scale vehicle [*3*]. The easiest way to do this would be to construct a custom vehicle chassis using an aluminum structure. Multiple suspension points can be incorporated into the design to provided alternate configurations. Provisions should also be made to allow ballast to be shifted in order to tune the vehicle inertial properties.

6.2.2 Control System

If the closed loop response of the vehicle is to be investigated, then the wireless communication system will need to be replaced, since it will introduce unnecessary nonlinearities to the system. Therefore, an onboard control system would need to be implemented that could accurately actuate the steering servo and drive motors. This can be accomplished by programming a microcontroller similar to what was done with the acquisition module; however, a more attractive option is to use a multipurpose development board.

One family of development boards popular among electronics enthusiasts is the Arduino development kit [*48*]. Due to the large support community, the range of devices that can interface with these kits is extensive. Anything from Bluetooth communication modules to data acquisition modules and even servo controllers are available that can be easily interfaced with the kit. The kits can be custom built with different processors in order to suit the application. Without investigating this in too much depth it is believed that a control solution can be easily implemented using these kits and would be less time intensive than what was done for the acquisition module.

References

[1]   S. Brennan and A. Alleyne, *Using a Scale Testbed: Controller Design and Evaluation*, IEEE Control Systems Magazine, 0272-1708 (2001), pp. 15-26.

[2]   B. Hamblin and S. Brennan, *Lessons Learned from Matching Experimental Data to Low Order Models of Vehicle Yaw, Sideslip and Roll Behavior*, ASME International Mechanical Engineering Congress and Exposition, Seattle, WA (2007), pp. 167-175.

[3]   S. Brennan, *On Size and Control: The use of Dimensional Analysis in Controller Design*, University of Illinois at Urbana-Champaign, PhD Thesis, 2002.

[4]   G. Genta, *Motor Vehicle Dynamics: Modeling and Simulation*, World Scientific, Singapore, 1997.

[5]   A. Stefanopoulou, A. Alleyne, R. Smith, K. Hedrick, and G. Rizzoni, *NSF Workshop on the Integration of Modeling and Control For Automotive Systems*, University of California, Santa Barbara, Workshop Report, 1999.

[6]   M. Tomizuka and J. Hedrick, *Advanced Control Methods for Automotive Applications*, Vehicle System Dynamics, 24 | 6 (1995), pp. 449-468.

[7]   J. Hyde, *Regulators Push Stability Control*, Detroit Free Press, September 15 (2006), pp. E1.

[8]   P. Haney, *The Racing & High Performance Tire*, Society of Automotive Engineers, Warrendale, PA, 2003.

[9]   T. Gillespie, *Fundamentals of Vehicle Dynamics*, Society of Automotive Engineers, Warrendale, PA, 1992.

[10]   W. F. Milliken and D. L. Milliken, *Race Car Vehicle Dynamics*, Society of Automotive Engineers, Warrendale, PA, 1995.

[11]   H. Josephs and R. Huston, *Dynamics of Mechanical Systems*, CRC Press, Boca Raton, FL, 2002.

[12]   S. Brennan and A. Alleyne, *Dimensionless Robust Control with Applications to Vehicles*, IEEE Transactions on Control Systems Technology, 13 (2005), pp. 624-630.

[13]   D. J. Leblanc, E. Johnson, P. Venhovens, G. Gerber, and R. DeSonia, *CAPC: A Road Departure Prevention System*, IEEE, 0272-1708 (1996), pp. 61-71.

[14]   Y. Furukawa and A. Masato, *Advanced Chassis Control Systems for Vehicle Handling and Active Safety*, Vehicle System Dynamics, 28 | 2 (1997), pp. 59-86.

[15]   D. Hrovat, *Survey of Advanced Suspension Developments and Related Optimal Control Applications*, Automatica, 33 | 10 (1997), pp. 1781-1817.

[16]   M. Nagai, H. Yutaka, and S. Yamanaka, *Integrated Control of Active Rear Steering and Direct Yaw Moment Control*, Vehicle System Dynamics, 27 | 5 (1997), pp. 357-370.

[17]   B. Hamblin, R. Martini, J. Cameron, and S. Brennan, *Low Order Modeling of Vehicle Roll Dynamics*, American Control Conference, Minneapolis, MN (2006), pp. 4008-4015.

[18]   B. Lam, *Lexus Self Parking Review*, Augus 25(2006), Website: http://gizmodo.com/196551/lexus-self-parking-car-video-and-review.

[19]   BMW, *Active Cruise Control*, Website: http://www.bmw.com/com/en/insights/technology/technology_guide/articles/active_cruise_control.html.

[20]   B. R. Munson, D. F. Young, and T. H. Okiishi, *Fundamentals of Fluid Mechanics*, 4th ed., Wiley & Sons, New Jersey, NJ, 2002.

[21]   E. Buckingham, *On Physically Similar Systems: Illustrations of the use of dimensional equations*, Bureau of Standards, 4 | 4 (1914), pp. 345-376.

[22]   S. Brennan, *Modeling and Control Issues Associated with Scaled Vehicles*, University of Illinois at Urbana-Champaign, Master Thesis, 1999.

[23]   P. Hoblet, R. O'Brien, and J. Piepmeier, *Scale Model Vehicle Analysis for The Design of a Steering Controller*, IEEE, 0-7803-7697-8 (2003), pp. 201-205.

[24]   W. E. Travis, R. J. Whitehead, D. M. Bevly, and G. T. Flowers, *Using Scaled Vehicles to Investigate the influence of Various Properties of Rollover Propensity*, American Control Conference, Boston, MA (2004), pp. 3381-3386.

[25]   R. Verma, D. D. Vecchio, and H. K. Fathy, *Development of a scaled vehicle with logitudinal dynamics of an HMMWV for an ITS testbed*, IEEE/ASME Transactions of Mechatronics, 13 | 1 (2008), pp. 1-12.

[26]   S. Kueperkoch, J. Ahmed, A. Kojic, and J. P. Hathout, *Novel vehicle stability control using steer by wire and independant four wheel torque distribution*, ASME IMECE, Washington, DC (2003), pp. 413-420.

[27]   J. Huang, J. Ahmed, A. Kojic, and J. P. Hathout, *Control oriented modeling for enhanced yaw stability and vehicle steerability*, American Control Conference, Boston, MA (2004), pp. 3405-3410.

[28]   S. Brennan, A. Alleyne, and M. DePoorter, *IRS - A Hardware in the Loop Testbed for Vehicle Dynamics and Control*, American Control Conference, Philadelphia, PA (1998), pp. 493-497.

[29]   S. Lapapong, V. Gupta, E. Callejas, and S. Brennan, *Fidelity of Using Scaled Vehicles for Chassis Dynamics Studies*, Vehicle System Dynamics, 47 | 11 (2009), pp. 1401-1437.

[30]   M. Polley, *Size Effects on Steady State Pneumatic Tire Behavior: An Experimental Study*, University of Illinoise at Urbana-Champaign, Master Thesis, 2003.

[31]   S. Brennan and A. Alleyne, *The Illinois Roadway Simulator: A Mechatronic Testbed for Vehicle Dynamics Control*, IEE/ASME Transactions of Mechatronics, 5 | 4 (2000), pp. 349-359.

[32]   M. Polley and A. Alleyne, *Dimensionless Analysis of Tire Characteristics for Vehicle Dynamics Studies*, American Control Conference, Boston, MA (2004), pp. 3411-3416.

[33]   S. Brennan and A. Alleyne, *Generalized H-Infinity Vehicle Control Using Dimensional Analysis*, American Control Conference, Denver, CO (2003), pp. 3774-3780.

[34]   Traxxas, *E-Maxx Owner's Manual*, Plano, TX, Manufacturer's Documentation, 2002.

[35]   D. Inman, *Engineering Vibrations*, 2nd ed., Prentice Hall, Saddle River, NJ, 2001.

[36]   R. A. Bixel et al., *Measured Vehicle Inertial Parameters - NHTSA's Data Through November 1998*, SAE Paper, 1999-01-1336, 1999.

[37]   K. D. Bird and J. F. Martin, *The Calspan Tire Research Facility: Design, Development and Initial Test Results*, SAE Paper, 730582, 1973.

[38]   R. W. Allen, T. T. Myers, T. J. Rosenthal, and D. H. Klyde, *The Effect of Tire Characteristics on Vehicle Handling and Stability*, Warrendale, PA, SAE Paper, 2000-01-0698, 2000.

[39]   F. Martin, B. Mikhak, and B. Silverman, *MetaCricket: A designer's kit for making computational devices*, IBM Systems Journal, 39 | 3 (2000), pp. 795-815.

[40]   Handyboard, *Handy Cricket Hardware Description*, Manufacturer's Documentation,.

[41]   Agilent Technologies, *The Fundamentals of Signal Analysis*, Application Note, 1997.

[42]   J. W. Nilsson and S. A. Riedel, *Electric Circuits*, 4th ed., Pearson, New Jersey, NJ, 2001.

[43]   S. Katzen, *The Quintessential PIC Microcontroller*, 2nd ed., Springer, England, 2001.

[44]   Microchip, *PIC18F4525 - Enhanced Flash Microcontrollers with 10-bit A/D and nano Watt Technology*, Manufacturer Data Sheet, DS39626E, 2008.

[45]   Microchip, *24AA1025 - 1024K I2C Serial EEPROM*, Manufacturer Data Sheet, DS21941F, 2008.

[46]   Rogue Robotics, *uMMC Serial Data Module Data Sheet*, Manufacturer Data Sheet, 2004.

[47]   J. J. Tuma, *Engineering Mathematics Handbook*, McGraw-Hill, New York, NY, 1979.

[48]   Sparkfun, *Development Boards*, Website: http://www.sparkfun.com/commerce/categories.php?c=103.

[49]   Handyboard, *The Handy Cricket Bus*, Manufacturer Documentation, 2004.

[50]   A. Glumac, *Scale Tire Modeling and Experimentation on a Rolling Roadway Simulator*, Pennsylvania State University Schreyer Honors College, Bachelor's Thesis, 2006.

[51]   H. Haftay and S. Brennan , *Use of Dimensional Analysis to Reduce the Parametric Space for Gain Scheduling*, American Control Conference, Portland, OR (2005), pp. 598-603.

[52]   H. Hu and H. Qiang, *Three Dimensional Modeling and Dynamic Analysis of 4-Wheel Steering Vehicles*, Acta Mechanica Sinica, 19 | 1 (2003), pp. 79-88.

Appendix A: Communication Protocols

A.1 Cricket Bus Protocol:

The Cricket bus utilizes a proprietary protocol that uses a byte-oriented data transfer scheme, with an additional bit included to distinguish between commands and data. The communications protocol follows a strict master-slave approach with the Cricket device as the single master, and all of the bus devices as slaves [40]. When the Cricket talks to the bus, it issues a command for a single bus device. That bus device may either silently take action, or it may respond by sending its "answer" back on the bus.

Each transmission consists of a 100 microsecond "prestart" synchronization pulse, which is followed by a start bit, 8 data bits (least significant bit first), a 9th bit to indicate command or data, and a stop bit. This is illustrated in Figure 81. The 100 us pre-start pulse is used for synchronization and allows all receiving devices to get ready to receive the bus data. All receiving devices are expected to dedicate their full attention to the bus signal by polling the bus pin before the synchronization period ends.
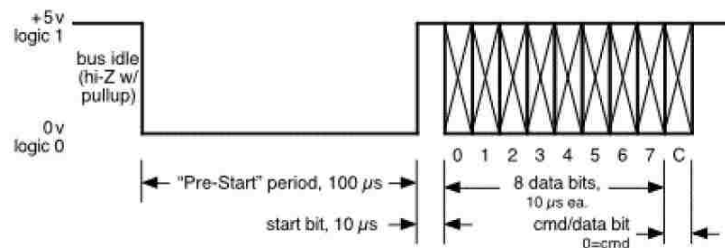
Figure 81: Handy Cricket bus protocol

The bus protocol starts with the initiation of a 100 μs prestart pulse as indicated above. This prestart pulse is used to ensure that the slave device is able to get ready to accept data. A start bit is sent followed by eight data bits. A ninth bit is sent which corresponds to the command bit. If the command bit is logic 1 then the word being sent is a command word and the slave must execute an action. If the command bit is logic 0 then the transmission is only data which the slave may or may not act on. Finally a stop bit is sent which terminates the transmission and signals the slave to carry out the required action. Figure taken from Cricket documentation [49].

At the rising edge of the start bit, receivers synchronize their internal timing to allow the remainder of the communication to be performed at the high speed of 10 microseconds per bit. Eight data bits are transmitted, followed by the command/data bit and then the stop bit. The command/data bit is used to indicate whether the byte being sent is a command byte or a data

byte. Command bytes may be sent only from the Cricket to bus peripherals, whereas data bytes can be the reply of a bus peripheral to the Cricket, or additional parameters needed to complete the Cricket command. Each bus peripheral has a unique 8-bit identifier, so any given command can only address one device at a time.

A.2 I^2C Communication Protocol:

Recall that the EEPROM uses a standard serial communication protocol called I^2C. The structure of the protocol is illustrated in Figure 82 using a byte write example.
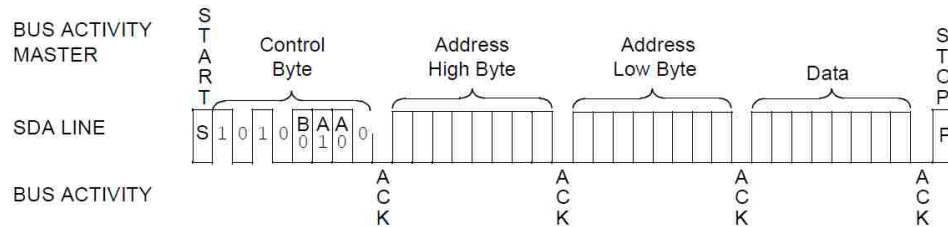
Figure 82: I^2C byte write protocol

The transmission is initiated by a start bit sent by the master device followed by a control byte. In the case of the EEPROM, the control byte specifies the device ID as well as the memory bank with which data is to be written. Once the slave has received the control byte, it is required to send an acknowledge bit to the master. The high and low byte of the memory location is then sent followed by the data byte that is to be written. The slave device must send an acknowledge bit after receiving each byte in order of the transmission to continue. Finally the sequence is terminated when the master device sends a stop bit. Figure taken from EEPROM datasheet [45].

In order to synchronize the data transmission the communication is initiated by the Master device sending a start condition. Next a control byte is sent to the slave device to let it know what operation is to be performed. The first four bits of the control byte are called the control code. For the EEPROM being used these will always have values of '1010'. The next bit is the block select bit. The EEPROM memory is organized into two banks of 512 kbits. Therefore the bank select bit lets the EEPROM know which bank of memory the data is to be written. The next two bits are the chip select bits which designate the address of the slave device to be used. Recall the address of the EEPROM was set by wiring A0 and A1 pins to V_{ss} or V_{DD}. The last bit within the control byte is the Read/Write bit which tells the slave device which operation is to be performed.

Upon receiving the control byte the slave device is required to send and acknowledge (ACK) bit to the Master device. Next the Master device will send a high byte and a low byte of the memory address location the data is to be written. Finally, the actual data byte to be written is sent to the EEPROM. After receiving each address and data byte the EEPROM is required to

send another ACK bit to the Master device. The transmission is ended when the Master device sends a stop condition which signals the EEPROM to start its internal write cycle, storing the data to the address location specified by the high and low address bytes.
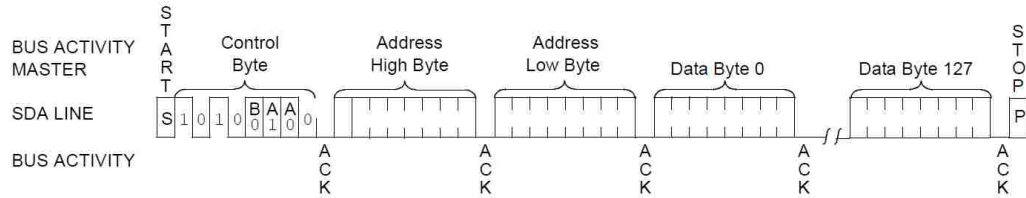
Figure 83: I^{2}C page write protocol

The page write process is the same as for byte write, however instead up to 127 additional data bytes are sent prior to sending the stop bit. This allows for much faster write cycles and higher data throughput overall. Figure taken from EEPROM datasheet [45].

Recall that the EEPROM has a page write capability which is illustrated in Figure 83. The only difference between the byte write and page write communications are that a stop condition is not sent after the first data byte. Rather, another 127 bytes of data can be sent with the EEPROM acknowledging each byte individually. The 127 bytes are stored in a buffer on the EEPROM until a stop condition is sent by the Master device. Once the stop condition is received, the EEPROM will start writing all 128 bytes of data to its memory. Note that read operations are handled the same way by setting Read/Write bit to a value of 1.

Appendix B: PIC Wiring Instructions

      The first step in developing the overall circuit was to understand how to wire the PIC microcontroller. The PIC microcontroller used for this research is a 40 pin device with each pin being multiplexed so they can be used to carry out multiple functions. The PIC's pin diagram is illustrated in Figure 84. Only a subset of the 40 pins was required to wire the acquisition module, therefore only those pins will be highlighted next. For a detailed overview of each pin and its function refer to the PIC18F 4525's datasheet.
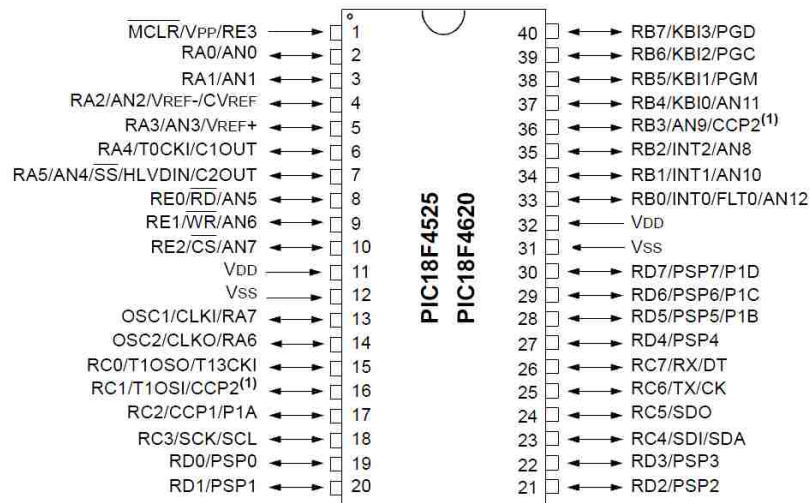
Figure 84: PIC18F 4525 pin diagram

The PIC18F 4525 is a 40 pin device with most pins being multiplexed so they can conduct multiple functions. Refer to the manufacturer's datasheet for detailed explanations on each pin and its associated function. Figure taken from PIC18F 4525 datasheet [*44*].

Pin 1: MCLR

      This pin is referred to as the Master Clear/Reset pin and is essential in ensuring that the microcontroller properly starts up from a power on or hard reset condition. Applying the supply voltage (VDD Pin 11) to the MCLR causes the microcontroller to initiate a start-up sequence which prevents it from executing any instructions until the supply voltage has had a chance to stabilize. This is essential because any fluctuations associated with the transient start-up of the power source could cause the microcontroller to become unstable. The MCLR pin is connected to VDD through a 1 kΩ resister.

Appendices | Andrew Liburdi

Pins 2-5, 7-10, 34-37: AN0 – AN 12

These 13 pins are used as the analog input channels for the A/D converter module. All 13 pins are multiplexed and can be used as digital inputs as well. Therefore, it is necessary in the firmware to set them as analog inputs by properly configuring the ADCON0 register as was discussed in the previous section. These pins were connected to the signal pin of each transducer.

Pins 11, 32: V_{DD}

V_{DD} accepts the supply voltage which for this application is regulated at 5V. Two V_{DD} pins are provided to ensure that the input current does not exceed maximum levels.

Pins 12, 32: V_{SS}

V_{SS} is designated as ground for the microcontroller. Two pins are provided to limit currents across each pin.

Pin 19: SCL

The SCL pin is used to transmit the serial clock pulse for the I2C communication protocol. It is automatically set as SCL when the MSSP module is configured to operate in I2C mode. The SCL pin is connected to the corresponding SCL pin on the serial EEPROM memory module.

Pin 23: SDA

The SDA pin is used to transmit serial data using the I2C communication protocol. The MSSP module must be configured in I2C mode in order to use this pin as the SDA. The pin is connected to the corresponding SDA pin on the serial EEPROM.

Pin 40: RB7

RB7 is configured as a digital input and is used to receive Handy Cricket bus commands. Recall that the Cricket uses a custom communication protocol which needs special subroutines written in the PIC's firmware in order to interpret and execute Cricket commands. This pin is connected to the signal pin on the Cricket's bus port.

Pin 41: RB6

RB6 is configured as a digital input and is connected to one of the Cricket's switch ports. When the PIC is conducting an acquisition it polls this pin to determine if the current acquisition should be stopped. If the pin value is logic 1 (5V) then the acquisition goes uninterrupted. When

the acquisition is to be stopped, the Cricket drives the value of RB6 to logic 0 (0V), which causes the PIC to cease collecting any further data.

Pins 27-30: RD4- RD7

These pins are configured as digital outputs and are connected to an LED array used to activate various LED sequences. The LED's are used to tell the operator when the PIC is ready, initializing or an error has occurred. Refer to the acquisition module operating instructions for more details on each LED sequence.

Pin 25: TX

The TX pin is used to transmit serial data using the EUSART module. It is automatically configured as the transmit pin when the EUSART is activated in the firmware. This pin is connected to the receive pin on the uMMC memory module.

Pin 26: RX

The RX pin is used to receive serial data from a slave device. It is automatically configured as the receive pin when the EUSART is activated in firmware. This pin is connected to the transmit pin on the uMMC memory module.

Appendix C: PIC Sample Source Code

```
;****************************************************************
;       Function: Cricket Bus Read                             *
;                                                              *
;       This function scans the busport and reads in data from the Handy Cricket.  *
;       It consists of a 100 us pre-start pulse followed by 10 bits each 10 us long *
;       for a total transmission length of 200 us. The last bit is the command bit. *
;       If the command bit is high, then it indicates a command instruction and the *
;       PIC needs to check the ID number for the proper operation.  The current *
;       code is based on a 8 MHz frequency and timing routines would need to be *
;       changed if another oscillator mode is to be used.      *
;                                                              *
;       Note: The following code is based on example code found in the *
;       Handy Cricket Bus documentation and was modified for this application *
;                                                              *
;****************************************************************

       CRICKET_READ:

       ready
              btfsc busport,buspin
                goto ready                    ; loop until bus line goes low

       pre_start
              btfss busport,buspin
                goto pre_start                ; wait for end of prestart

              movlw 8
              movwf buscntr
              call delay_5cyc
              call delay_5cyc
              nop
              nop
              nop

       data_loop
              call delay_5cyc
              call delay_5cyc
              nop
              nop
              nop
              rrcf busdata,F                  ; pre-rotate destination byte
              bcf busdata,7                   ; clear high bit (it'll rotate down)
              btfsc busport,buspin
              bsf busdata,7                   ; if BUSPIN was set, set busdata bit
              decfsz buscntr,F
                goto data_loop
```

```
        call delay_5cyc
        call delay_5cyc
        call delay_5cyc

        bcf STATUS,C                    ; pre-set carry (cmd word)
        btfsc busport,buspin
        bsf STATUS,C                    ; if no stop bit, clear carry

        return
```
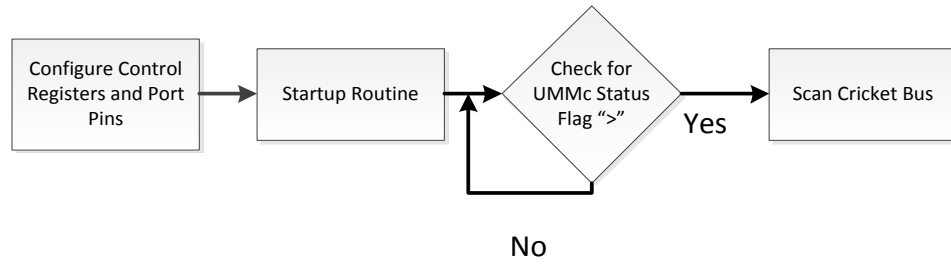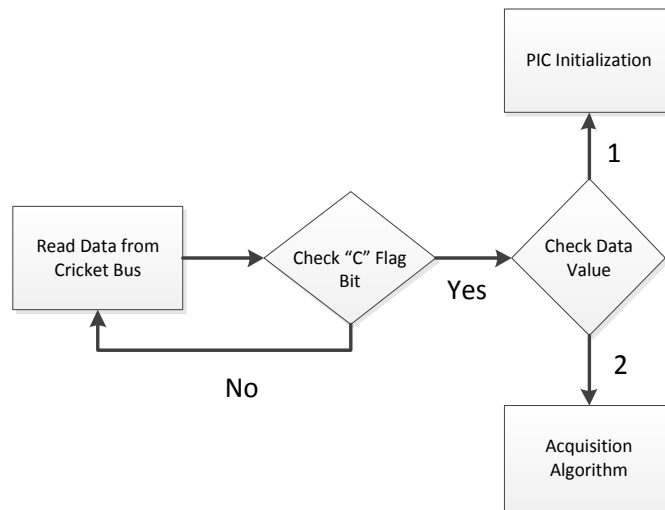
;***
;***

Appendix D: Subroutine Flow Charts

D.1 PIC Initialization

```
┌──────────────────┐      ┌──────────────┐        ◇ Check for        ┌──────────────────┐
│ Configure Control│      │              │       ◇ UMMc Status ◇     │                  │
│ Registers and Port│ ──▶ │ Startup Routine│ ──▶ ◇  Flag ">"   ◇ ──▶│ Scan Cricket Bus │
│      Pins        │      │              │        ◇          ◇  Yes  │                  │
└──────────────────┘      └──────────────┘         ◇        ◇       └──────────────────┘
                                  ▲                    │
                                  │                    │
                                  └────────────────────┘
                                             No
```

D.3 Scan Cricket Bus

```
                                                        ┌──────────────────┐
                                                        │ PIC Initialization│
                                                        └──────────────────┘
                                                                 ▲
                                                                 │  1
                                                            ◇ Check Data ◇
┌──────────────┐        ◇ Check "C" Flag ◇               ◇   Value    ◇
│ Read Data from│ ──▶  ◇      Bit       ◇  ──▶           ◇            ◇
│ Cricket Bus  │        ◇              ◇   Yes            ◇          ◇
└──────────────┘         ◇            ◇                     │  2
       ▲                    │                               ▼
       │                    │                      ┌──────────────────┐
       └────────────────────┘                      │   Acquisition    │
                 No                                 │   Algorithm      │
                                                    └──────────────────┘
```

D.4   Acquisition Routine

D.5 Initialize Data File

```
┌─────────────────┐
│  Read in Dataset │
│      Value       │
└─────────────────┘
         │
         ▼
┌─────────────────┐
│  Convert Dataset │
│  Value to BCD    │
│     Format       │
└─────────────────┘
         │
         ▼
┌─────────────────┐
│   Send Open      │
│ Command to UMMc  │
└─────────────────┘
         │
         ▼
┌─────────────────┐
│                  │
│ Scan Cricket Bus │
│                  │
└─────────────────┘
```
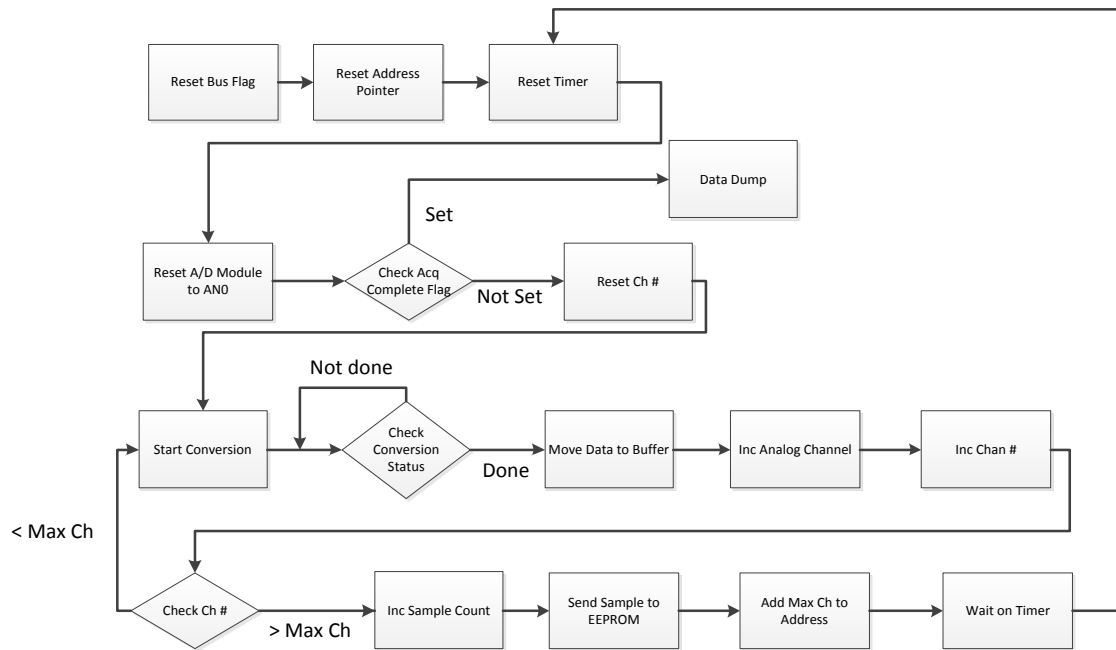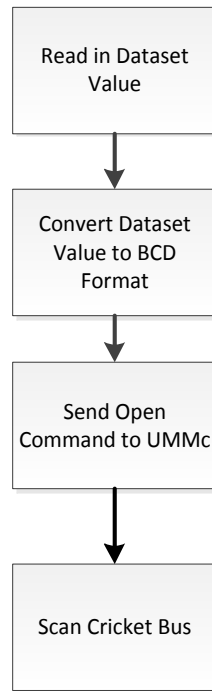
Appendix E: Steady State Transfer Functions

E.1   Yaw Rate: $\phi\,/\delta$

Equating the derivative terms to zero in the bicycle model gives,

$$\frac{(c_f+c_r)}{u}\,v\;+\;\left[\frac{(ac_f-bc_r)}{u}+mu\right]\phi\;=c_f\delta \tag{1}$$

$$\frac{(ac_f-bc_r)}{u}\,v\;+\frac{(a^2c_f+b^2c_r)}{u}\,\phi\;=ac_f\delta \tag{2}$$

From (1):

$$\left(c_f+c_r\right)v+\left[\,\left(ac_f-bc_r\right)+mu^2\right]\phi=uc_f\delta$$

$$v=\frac{uc_f\delta-[(ac_f-bc_r)+mu^2]\phi}{c_f+c_r} \tag{3}$$

Substitute (3) into (2):

$$\frac{(ac_f-bc_r)}{u}\left\{\frac{uc_f\delta-\left[(ac_f-bc_r)+\;mu^2\right]\phi}{c_f+c_r}\right\}+\frac{(a^2c_f+b^2c_r)}{u}\;\phi=\;ac_f\delta$$

$$\{-(ac_f-bc_r)[(ac_f-bc_r)+mu^2]+(a^2c_f+b^2c_r)(c_f+c_r)\}\phi$$
$$=[auc_f(c_f+c_r)-uc_f(ac_f-bc_r)]\delta$$

$$\left[-a^2c_f^2+\;2abc_fc_r-b^2c_r^2-\left(ac_f-bc_r\right)mu^2+\;a^2c_f^2+a^2c_fc_r+b^2c_fc_r+b^2c_r^2\right]\phi$$
$$=\left(auc_f^2+auc_fc_r-auc_f^2+\;buc_fc_r\right)\delta$$

$$\left[(a+b)^2c_fc_r-mu^2\left(ac_f-bc_r\right)\right]\phi=\left[(a+b)uc_fc_r\right]\delta$$

$$\frac{\phi}{\delta}=\frac{(a+b)uc_fc_r}{(a+b)^2c_fc_r-mu^2(ac_f-bc_r)}$$

Yaw Rate Transfer
Function:

$$\frac{\phi}{\delta}=\frac{u}{(a+b)-\dfrac{mu^2(ac_f-bc_r)}{(a+b)c_fc_r}}$$

Appendices | Andrew Liburdi

E.2 Lateral Velocity: v/δ

Equating the derivative terms to zero in the bicycle model gives,

$$\frac{(c_f+c_r)}{u} v + \left[\frac{(ac_f-bc_r)}{u} + mu\right]\phi = c_f\delta \qquad (1)$$

$$\frac{(ac_f-bc_r)}{u} v + \frac{(a^2c_f+b^2c_r)}{u}\phi = ac_f\delta \qquad (2)$$

From (2):
$$\left(a^2c_f + b^2c_r\right)\phi = uac_f\delta - \left(ac_f - bc_r\right)v$$

$$\phi = \frac{uac_f}{a^2c_f+b^2c_r}\delta - \frac{(ac_f-bc_r)}{a^2c_f+b^2c_r}v \qquad (3)$$

Substitute (3) to (1):

$$\frac{(c_f+c_r)}{u}v + \left[\frac{(ac_f-bc_r)}{u}+mu\right]\left[\frac{auc_f}{(a^2c_f+b^2c_r)}\delta - \frac{(ac_f-bc_r)}{(a^2c_f+b^2c_r)}v\right] = c_f\delta$$

$$\left\{\frac{(c_f+c_r)}{u} - \left[\frac{(ac_f-bc_r)}{u}+mu\right]\left[\frac{(ac_f-bc_r)}{(a^2c_f+b^2c_r)}\right]\right\}v$$

$$= \left\{c_f - \left[\frac{(ac_f-bc_r)}{u}+mu\right]\left[\frac{auc_f}{(a^2c_f+b^2c_r)}\right]\right\}\delta$$

$$\frac{v}{\delta} = \left\{c_f - \left[\frac{(ac_f-bc_r)}{u}+mu\right]\left[\frac{auc_f}{(a^2c_f+b^2c_r)}\right]\right\}$$

$$* \left[\frac{u(a^2c_f+b^2c_r)}{(c_f+c_r)(a^2c_f+b^2c_r) - (ac_f-bc_r)^2 - mu^2(ac_f-bc_r)}\right]$$

$$\frac{v}{\delta} = \left[c_f - \frac{ac_f(ac_f-bc_r)+mau^2c_f}{a^2c_f+b^2c_r}\right]\left[\frac{u(a^2c_f+b^2c_r)}{(a^2+2ab+b^2)c_fc_r-mu^2(ac_f-bc_r)}\right]$$

$$\frac{v}{\delta} = \left[\frac{(b^2c_fc_r+abc_fc_r-mau^2c_f)}{a^2c_f+b^2c_r}\right]\left[\frac{u(a^2c_f+b^2c_r)}{(a+b)^2c_fc_r-mu^2(ac_f-bc_r)}\right]$$

$$\frac{v}{\delta} = \frac{bc_fc_r(a+b)-ma^2c_f}{(a+b)^2c_fc_r-mu^2(ac_f-bc_r)}u$$

Appendices | Andrew Liburdi

Lateral Velocity
Transfer Function

$$\frac{v}{\delta} = \frac{b - \dfrac{mau^2}{(a+b)c_r}}{(a+b) - \dfrac{mu^2(ac_f - b_r)}{(a+b)c_f c_r}} u$$

Vita Auctoris

Andrew M. Liburdi was born on March 22, 1983, in Windsor, Ontario, Canada. He graduated from Kennedy Collegiate High School in 2002. He then attended the University of Windsor, where he earned the degree of Bachelor of Applied Science in Mechanical Engineering, with distinction. Upon graduating he received an Ontario Graduate Scholarship to pursue a Master of Applied Science degree in Mechanical Engineering at the University of Windsor in 2006. He switched to part time status in 2007 to pursue a career at Chrysler LLC where he worked full time as a Road Test Simulation engineer. He is presently a candidate for the Master of Applied Science in Mechanical Engineering degree at the University of Windsor, and is scheduled to graduate in October 2010. His current employment is with General Dynamics Land Systems Canada as a design engineer.